Remote Sensing of Water Surface Variability Near River Mouths

Ruth A. Branch

A dissertation
submitted in partial fulfillment of the
requirements for the degree of

Doctor of Philosophy

University of Washington

2020

Reading Committee:

Alexander R. Horner-Devine, Chair

Nirnimesh Kumar

C. Chris Chickadel

Program Authorized to Offer Degree:
Civil & Environmental Engineering

University of Washington

Abstract

Remote Sensing of Water Surface Variability Near River Mouths

Ruth A. Branch

Chair of the Supervisory Committee:
Allan and Inger Osberg Associate Professor Alexander R. Horner-Devine
Civil & Environmental Engineering

Rivers discharge approximately $10^6 \mathrm{m}^3/s$ of freshwater to the oceans (*Geyer et al.*, 2004), yet less than 60% of this discharge is measured at the river mouth (*Fekete et al.*, 1999). The standard method of measuring river discharge is to use in-situ current meters that are expensive to deploy and not easily used at remote locations. Remote sensing of river discharge could address the problem of global coverage and is becoming an active area of research due to the recent and upcoming improvements of the resolution of satellite altimeters. Remote measurements of river discharge have been made from altimeter type water surface elevation data before but only far upstream where the flow is uniform. In order to accurately quantify the amount of freshwater being discharged into the ocean the discharge measurement must be made at the river mouth where the flow is not uniform and the relationship between water surface elevation and discharge is not well understood.

At the river mouth, the water surface elevation is dependent on discharge but it is also influenced by tides and bathymetry (*McCabe et al.*, 2009; *Poggioli and Horner-Devine*, 2015, 2018). This thesis uses airborne Lidar data, numerical model output, and derived equations to characterize the relationships between river discharge, water surface elevation, tides, and bathymetry at the river mouth. It is found that the slope of the water surface elevation at the mouth of the Columbia River changes sign over the tidal period and that wave amplification increases with river flow velocity. Numerical model output of a generalized river describes the shape of the water surface elevation near the river mouth under both low

and high discharge conditions. During high discharge conditions an offshore ridge develops on the water surface whose location and height are related to river discharge. Equations are derived to calculate the location and height of the ridge and are used to predict if the upcoming Surface Water and Ocean Topography (SWOT) altimeter will be able to detect the ridge for flow from the Mississippi, Connecticut, and Columbia Rivers. This research provides an understanding of how the level and shape of the water surface elevation at the river mouth is related to tides, waves, and discharge and quantifies which of these signals will be observable by SWOT.

Finally, equations are derived to calculate the river bottom drag coefficient from remotely sensed surface measurements of the turbulent kinetic energy and horizontal Reynolds stress. The equations are tested with field data from the Snohomish River and the drag coefficients calculated from the surface turbulent kinetic energy compare well with drag coefficients calculated from *in situ* velocity data. In the future, the turbulent kinetic energy equation for the drag coefficient and remote sensing techniques presented here could be applied to data from unmanned aerial vehicles.

TABLE OF CONTENTS

LIST OF FIGURES

LIST OF TABLES

ACKNOWLEDGMENTS

I'd like to thank my advisor, Alex Horner-Devine, for giving me such exciting projects to work on, spending many hours teaching me fluid mechanics, and patiently helping me learn how to write. He is one of the most positive, brave, and tenacious people I've ever met. We had a lot of failures during our time working together but Alex always came up with another idea of what to try next. He seems to have an endless supply of good ideas and it was my privilege to work on them. Few people ever get the opportunity to do basic research with such a great scientist and I will always be thankful that I was one of them.

My committee is also composed of great scientists who played a large role in this thesis. Andy Jessup and Chris Chickadel very generously gave me their data from COHSTREX and DARLA to analyze. They designed the experiments, wrote the proposals, built the equipment, and collected the data. Much of this thesis is just following through on the science questions they posed and collected data to answer. Stefan Talke also participated in the COHSTREX and DARLA experiments and was very generous in sharing his analysis code with me and his expertise on turbulence and tides at the mouth of the Columbia River. Nirni Kumar came to UW when I was half way through grad school and rescued my thesis by helping me with a modeling project to replace my failed laboratory experiment. He has been such a wonderful addition to the department not only as an excellent scientist but also as a really great human being. UW is lucky to have him and I hope the department realizes how valuable he is.

I'd like to thank Dan Clark who engineered and built the many complicated instrument systems used to collect these data. This research would not have been possible without his amazing engineering and programming skills. I suspect he put as many hours into preparing for and collecting the data as I did in analyzing it. Measuring waves from a tiny airplane bouncing around in the wind at the mouth of the Columbia River and turbulence from

infrared imagery are not small accomplishments and I hope he knows how valuable his contribution to these projects was.

My friends in the Environmental Fluid Mechanics group at UW were very supportive and helpful throughout the grad school process. I doubt I would have survived the first year of classes without Sam Kastner. The students who graduated before me: Anthony, Seth, Roxanne, Brad, Raul, Maricarmen, Maddie, and Molly were so inspiring and helpful at each step of the grad school process. Those who will graduate after me: Sam K., Zhuochen, Christine, Shelby, Sam F., and Sam B. have helped me learn how to give a good talk and make good figures. Jim Thomson is not on my committee but he is a co-author on the paper from Chapter 2 and was very helpful by answering emails about ADCP measurements for Chapter 4 even though he was on a cruise in the middle of the Arctic ocean. The EFM group is such a great community. I look forward to hearing about the exciting science everyone from this group does in the future.

Grad school was very much an exercise in walking on water for me. Every time I started to sink someone reached down a hand and pulled me back up. I'd like to thank my favorite scientist and best friend, Trevor, for daily encouragement, unwavering support, and mentoring along the path of science. I literally thank God for you every day and feel so blessed to be your wife. Thank you for sacrificing your career so that I could pursue this dream of grad school. I'd also like to thank my mother for always believing in me, sacrificing so much for me, and spending many hours taking care of my kids while I worked on this thesis. Lastly, I'd like to thank Simon for filling my life with beautiful music and Patrick for keeping us all entertained and laughing with his enthusiasm for life.

DEDICATION

to my amazing husband, Trevor, my wonderful mother, Mary, and my two precious sons, Patrick and Simon

Chapter 1

INTRODUCTION

1.1 Motivation

Freshwater is one of earth's most precious resources. Rivers transport this precious resource from the mountains to coast and discharge it into the ocean. When river flow is too low, freshwater scarcity becomes a critical issue for the 2.3 billion people that live in river basins under water stress (*Johnson et al.*, 2001). When river flow is too high, floods and erosion affect the hundreds of millions of people that live near the coast in river deltas (*Syvitski and Saito*, 2007). River discharge is difficult to predict and can vary by an order of magnitude over the course of a year (*Horner-Devine et al.*, 2015).

Rivers carry freshwater, sediment, and nutrients into the coastal ocean (*Syvitski et al.*, 2003) where their along-coast transport is controlled by stratified-shear mixing, frontal processes, geostrophic transport, and wind forcing (*Horner-Devine et al.*, 2015). Some rivers, like the River Teign, dishcarge a small amount of freshwater that forms into small buoyant plume after ebb tide and dissipates over a few hours (*Pritchard and Huntley*, 2006). Very large rivers, like the Mississippi, discharge a large amount of freshwater that forms into a persistent plume dominating the coastal circulation of the whole region (*Cochrane and Kelly*, 1986; *Zhang et al.*, 2012; *Zhang and Hetland*, 2012). The magnitude of discharge controls sediment deposition and erosion in the delta and at the river mouth. Low discharge causes sediment deposition while high discharge causes erosion and river-bed scour (*Lamb et al.*, 2012; *Chatanantavet et al.*, 2012). Many rivers are much deeper near their mouths than farther upstream, and it has been hypothesized that this is due to scour during large floods (*Lane*, 1957). High discharge floods may be infrequent but they need to be understood because they are the drivers of morphological change near the river mouth.

1.2 Calculating discharge from water surface elevation

Time-series of discharge measurements are important for assessing hydrological variability and planning for climate change, water security issues, and floods and droughts (*Hannah et al.*, 2011). The current method of measuring discharge is to use in-situ current meters, which are expensive to deploy and not easily used at remote locations. Remote sensing of discharge could address the problem of global coverage and is becoming an active area of research (*Bjerklie et al.*, 2003; *Bates et al.*, 2013; *Pavelsky et al.*, 2014), particularly due to recent and planned advances in the resolution and coverage of satellite altimeters. Satellite measurements of water surface elevation have improved in accuracy from 0.35 m for TOPEX/Poseidon to 0.1 m for ICESat (*O'Loughlin et al.*, 2016). Algorithms are used to convert water surface elevation measurements into discharge estimates. The most commonly used algorithms for remotely estimating discharge, Q, rely on slope-area methods such as Manning's equation (*Manning et al.*, 1890), which require inputs of bottom roughness, n, cross-sectional area, A, hydraulic radius, R_H, and water surface slope, S (*Alsdorf et al.*, 2007; *Durand et al.*, 2014; *Bonnema et al.*, 2016)

$$Q = \frac{k_n}{n} A R_H^{2/3} S^{1/2} \tag{1.1}$$

where $k_n = 1$ in the metric unit system. Estimating global river discharge using entirely remotely sensed measurements of these parameters remains an elusive goal (*Lettenmaier et al.*, 2015).

Remotely sensed water surface slope measurements have been used to calculate discharge in the Amazon (*LeFavour and Alsdorf*, 2005), Willamette (*Tuozzolo et al.*, 2019), and Tanana (*Altenau et al.*, 2019) rivers but the measurements were made upstream far from the river mouth where the flow is uniform and slope-area equations apply. Near the river mouth the water surface slope is controlled by discharge but can also be influenced by tides, waves, upwelling, and channel geometry (*McCabe et al.*, 2009; *Poggioli and Horner-Devine*, 2015, 2018). A clear understanding of how the water surface changes with these processes could lead to new methods of measuring discharge remotely at the river mouth.

1.3 River bottom roughness

Bottom roughness is a key parameter in all numerical models of river systems and slope-area methods to measure discharge. It is a parameter that satellite altimeters will not be able to measure (*Durand et al.*, 2014) and the current methods of using in-situ sonar are costly. Historically, the Manning's n of a river reach was estimated by finding a photograph in a government document that matched the characteristics of the site being studied (*Barnes*, 1967). Currently, it is often estimated by varying its value in a model such as HEC-RAS until the model output agrees with in-situ sensor measurements (*Timbadiya et al.*, 2011; *Parhi et al.*, 2012; *Hameed and Ali*, 2013).

In a river bed, the bottom roughness is almost always composed of sand or rocks organized into dunes or ripples (*Nezu and Nakagawa*, 1993a). Often the ripples are superimposed on top of the dunes and the turbulence generated depends on the shape of the resulting bedform (*Best*, 2005). As the river water flows over roughness elements, wakes and jets are created that propagate up to the surface (*Moog and Jirka*, 1999a). The amount and intensity of the wakes and jets depends on the bottom roughness. The Reynolds stress has been observed experimentally to be higher in the water column above a rough surface than a smooth surface (*Best*, 2005; *Balachandar and Bhuiyan*, 2007). The process of the turbulent motion moving up through the water column from the bottom to the surface can be described with the "chain saw model" where large scale eddies transport turbulent energy to the surface but smaller scale eddies renew the surface and are important to gas transfer (*Moog and Jirka*, 1999b). The turbulent kinetic energy that is transported up through the water column can be measured near the surface with an *in situ* velocimeter and at the surface with infrared or visible videos (*Chickadel et al.*, 2011; *Johnson and Cowen*, 2017). Surface turbulence statistics can be calculated when the velocity is extracted from videos of the surface using particle imaging velocimetry (PIV). PIV works with visible imagery if there is a tracer such as seeding materials and with infrared imagery when a temperature contrast shows the water movement. If PIV can remotely measure surface turbulence statistics and those statistics are dependent on bottom roughness, then that roughness can be measured remotely.

1.4 Thesis Outline

This thesis aims to answer three questions related to river discharge estimation from surface elevation signals and bottom roughness estimation from remotely sensed turbulence statistics. The questions are answered with a combination of data from field experiments and numerical modeling output. The three questions are:

- What relevant water surface signals can be remotely detected at the mouth of the Columbia River?
- How does the water surface elevation change with discharge at the mouth of a generalized river?
- How are remotely sensed turbulence statistics related to river bottom roughness?

In Chapter 2, airborne Lidar data from the Data Assimilation and Remote Sensing for Littoral Applications (DARLA) experiment at the mouth of the Columbia River is used to determine the relevant water surface elevation signals that can be detected remotely. The remotely sensed signals are compared with in-situ data when it is available and co-located ROMS output is examined to give more information about the parts of the tidal cycle when airborne data is unavailable. This chapter is:

>

Chapter 3 examines water surface elevation changes with discharge at the mouth of a generalized river modeled with ROMS. I derive equations to predict the location and height of an offshore water surface slope change during high discharge events. This work will be published in the joint issue of the Journal of Geophysical Research and Water Resources Research on Coastal Hydrology and Oceanography as,

Branch, R. A., A. R. Horner-Devine, N. Kumar, and A. R. Poggioli, River plume liftoff dynamics and surface expressions, *Water Resources Research*.

Chapter 4 presents new results from the COHerent STructures in Rivers and Estuaries EXperiment (COHSTREX) on the Snohomish River. Turbulence statistics are calculated from remotely sensed infrared imagery and compared to river bottom roughness measured with sonar. This chapter will be submitted with the following title and co-authors,

Branch, R. A., A. R. Horner-Devine, C. C. Chickadel, A. T. Jessup, and S. A. Talke, Remote sensing of river bottom roughness.

Finally, Chapter 5 gives a summary of my conclusions and recommendations for future research.

Chapter 2

AIRBORNE LIDAR MEASUREMENTS AND MODEL SIMULATIONS OF TIDES, WAVES, AND SURFACE SLOPE AT THE MOUTH OF THE COLUMBIA RIVER

2.1 Introduction

River discharge into the ocean influences coastal stratification and coastal currents (*Hickey and Banas*, 2003), carries sediments and nutrients into the ocean (*Syvitski et al.*, 2003), and, considered globally, forms an incompletely known portion of the global water mass balance and sea-level budget. Since river slope is related to discharge, remotely sensing river and coastal water surface elevations has become an active area of research (*Bjerklie et al.*, 2003), particularly due to recent and planned advances in the resolution and coverage of satellite altimeters, including the upcoming launch of the SWOT (Surface Water Ocean Topography) altimeter which will be used to investigate sea level variability in the coastal zone (*Turki et al.*, 2015). The SWOT altimeter, which will measure with a swath resolution of < 60 m, slope accuracy of 1.7 cm/km for water areas > 1 km^2, vertical accuracy < 25 cm, and return period of 20.86 days (*Biancamaria et al.*, 2016), is designed to measure water levels in regions of little or no data. A primary SWOT science objective is to calculate river discharge from measurements of water surface elevation (*Durand et al.*, 2010). The presence of tides, however, greatly complicates measurements of river flow near the mouth due to non-linear tide-current interaction, the compensation flow for Stokes drift, and other factors (*Kukulka and Jay*, 2003) (*Moftakhari et al.*, 2016). Hence, while a slope/discharge technique has been used with remote sensing data before, it is limited to regions far from the mouth (*LeFavour and Alsdorf*, 2005). Such measurements miss the effect of coastal tributaries and other factors such as evaporation or water withdrawal which can significantly influence the water mass balance. To avoid these confounding factors, one would ideally measure discharge at the river mouth, using the water level slope after correcting for the influence of tides (e.g., method of (*Hudson et al.*, 2017)).

In this chapter, I present the first airborne Lidar measurements of sea surface elevation at a river mouth which I combine with a numerical model to investigate dynamical processes. The mouth of the Columbia River (MCR) is a critical dynamical region for navigation and connectivity between the ocean and the river environment. It is an energetic region subject to high river discharges, large waves, significant tides, and strong winds. This effort builds off the results of (*Hudson et al.*, 2017), who used airborne Lidar to measure river slope within the tidal river but did not measure at the river mouth where the complexity of the region introduces different processes such as wave amplification, that can influence the sea surface elevation and slope. Specifically, this research investigates the feasibility and challenges of measuring water levels and surface slopes at the river mouth in order to evaluate the potential for estimating coastal river discharge from remotely sensed data.

Airborne Lidar measures the distance between an airplane and the water surface using a laser time-of-flight ranging system, and corrects for plane movement using an inertial navigation system. The airplane moves quickly (40 m/s) sampling a 15 km stretch of river in 5-10 minutes. Each 15 km transect is a snapshot of the conditions, assuming that currents and waves are stationary over that time period. The rapidly sampled Lidar measurements provide high spatial resolution sufficient for resolving surface waves. This enables us to assess the effects of small scale variability such as wave setup that might not be detectable by spaceborne sensors. Several Lidar transects can be combined to form a swath of the conditions over a half hour period. The combined data provides a unique platform to simultaneously measure waves and tides rather than only tides (*Hudson et al.*, 2017) or waves (*Reineman et al.*, 2009).

Wave height amplification due to wave-current interactions is a well known navigational hazard at the MCR, but is difficult to measure *in-situ* due to dangerous, spatially and temporally variable, and highly energetic conditions. Moored (*González*, 1984) and drifting buoys (*Thomson et al.*, 2014) have measured significant wave heights amplified by a factor of three near the mouth compared with locations offshore during ebb tide, but the spatial and temporal effects of tides on waves have not been empirically quantified. Numerical modeling studies predicted that wave-current interactions cause an increase in wave height of almost 200% during ebb (*Elias et al.*, 2012; *Akan et al.*, 2017). Since wave amplification can produce

patterns of setup and setdown, such spatial variations may influence remotely sensed water levels and thus affect estimates of tidal slope or river discharge from the measurements.

Surface elevation changes with the tide have been predicted by numerical models at the MCR in order to study the vertical current structure (*Elias et al.*, 2012), wave-current interactions (*Akan et al.*, 2017), plume spreading (*McCabe et al.*, 2009), and tidal salt transport mechanisms (*Kärnä and Baptista*, 2016). The models showed strong qualitative agreement with in-situ tidal gauges however they did not study the surface elevation for the purposes of quantifying the surface slope. One goal of this research is to determine if the slope changes caused by the tide can be measured remotely. If slope changes due to the tide can be quantified and removed from the elevation signal, then it may be possible to measure slope changes due to river discharge.

In this chapter I use airborne Lidar data and a numerical model to study the water surface elevation, waves, and surface slope at the mouth of a river. In the Methods section I describe how the Lidar data were acquired and how the physical parameters such as significant wave height and surface slope were calculated from the data. I also describe the numerical model and how it was run for the same time period that the Lidar data were acquired. In the Results section I verify that the Lidar correctly measures water surface elevation, waves, and surface slope by comparing my results with tide gauges, drifting wave buoys, and the numerical model outputs. In the Discussion section I outline possible sources of measurement error and natural variability that cause differences between the Lidar measurements and *in-situ* measurements or model predictions. In the Conclusions section I summarize the success of the airborne Lidar at studying the physical processes at the mouth of the Columbia River and discuss directions for future research.

2.2 Methods

2.2.1 Study Site

The Columbia River discharges into the Pacific Ocean on the west coast of North America, on the border between Oregon and Washington state. Tide, wave, and discharge conditions are monitored continuously near the MCR by NOAA (National Oceanographic and

Atmospheric Administration), NDBC (National Data Buoy Center), and the USGS (United States Geological Survey) due to its navigational and ecosystem importance in the region. I compare Lidar measurements of tides with tidal levels measured by NOAA at the Hammond station (station 9439011, river kilometer 15 from the mouth) and waves with offshore wave measurements at the NDBC buoy 46029 (37 km offshore) (Fig. 2.1b). River discharge was measured by the USGS at the Beaver Army Terminal (river kilometer 86, Fig. 2.1b), where 97% of the total freshwater discharged into the ocean is measured (*Naik and Jay*, 2011), (*Orem*, 1968).

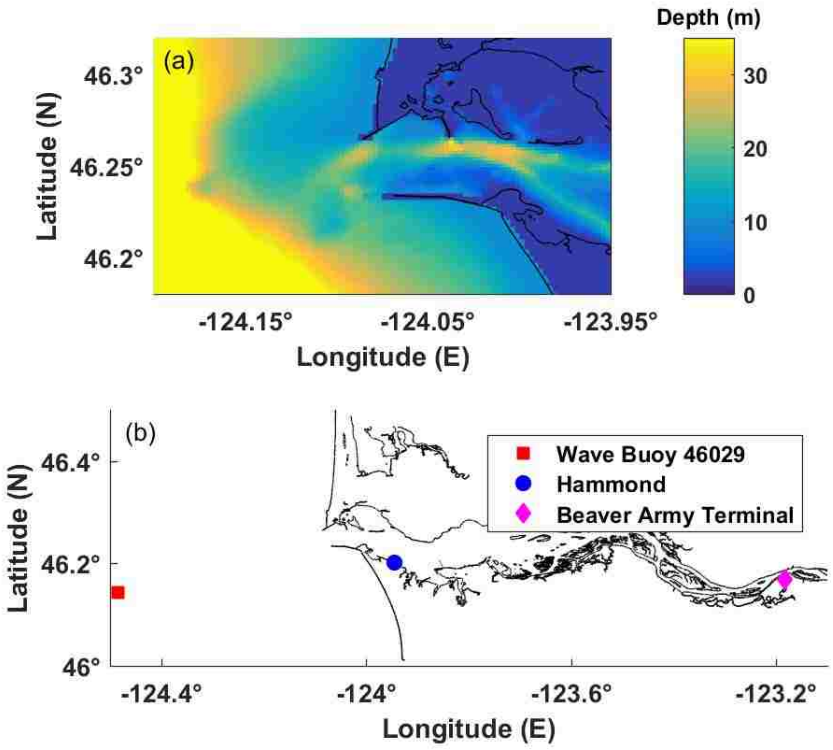

Figure 2.1: Study site at the MCR. (a) The bathymetry shows the influence of the three jetties and channel dredging. (b) Locations of the wave buoy 46029, tidal station at Hammond, and discharge measurement at Beaver Army Terminal.

The bathymetry at the MCR is complex due in part to the influence of maintenance dredging and three jetties which channelize flow and promote ebb currents of up to 3 m/s

(*Elias et al.*, 2012). The depth varies from 15-30 m between the estuary and the ocean (Fig. 2.1a). A shallow area just east of the jetties is called the "inner bar" and west of the jetties to longitude -124.17 is called the "outer bar", though no shoals are exposed during low tide (*Gonazález*, 1984).

2.2.2 Lidar instrumentation and experimental conditions

Airborne Lidar data were collected with a Riegl LD90-3800EHS-FLP instrument flown on a Cessna 172SP. The Lidar measures the distance between the plane and the water uncorrected for plane altitude or elevation. Pitch and roll accuracy was less than 0.01 degrees and heading accuracy was less than 0.025 degrees. The GPS was receiving Omnistar HP position correction information via satellite, which reduced 95% of the vertical position errors to less than 10 cm, based on the manufacturer's assessment. The IMU had a variable time offset and possible drift with respect to the Lidar clock which was corrected by using a method based on a Taylor's series expansion (*Hudson et al.*, 2017).

Data were analyzed from 26 flights flown on 20 days from May to September 2013, with most of the data collection from May 26th through June 10th. The May through June experiment spanned wave conditions with significant wave heights of 0.67 to 3.51 m, tidal heights of -1.88 to 1.71 m, and river discharge of 7,895 to 10,902 m^3/s (Fig. 2.2). These are all within the range of typical summer values at the MCR. The plane could only fly during daylight, which meant that no flight sampled an entire tidal cycle (Fig. 2.2c). Each flight flew multiple transects in and out of the mouth of the river. An example flight track from May 26th that included eight transects is shown in Figure 2.3a. Each transect was approximately 15 kilometers long and took the airplane 5-10 minutes to complete.

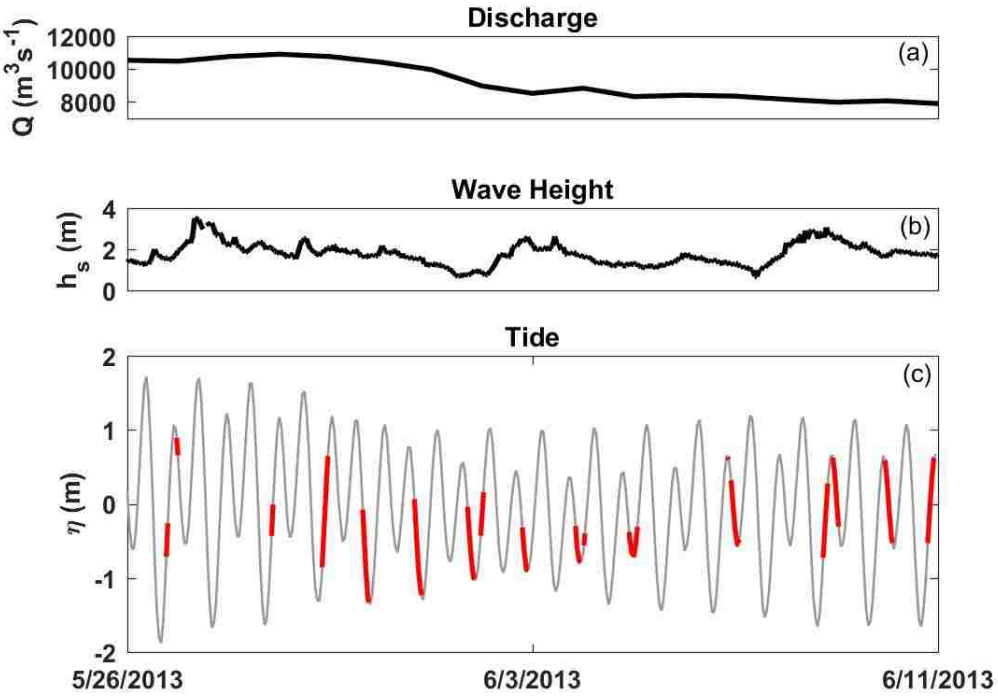

Figure 2.2: a) Discharge, Q, measured at Beaver Army Terminal, b) wave height, h_s, measured by buoy 46029, and c) tidal water surface elevation, η, measured at Hammond during the main data collection period. Red lines indicate Lidar flight times.

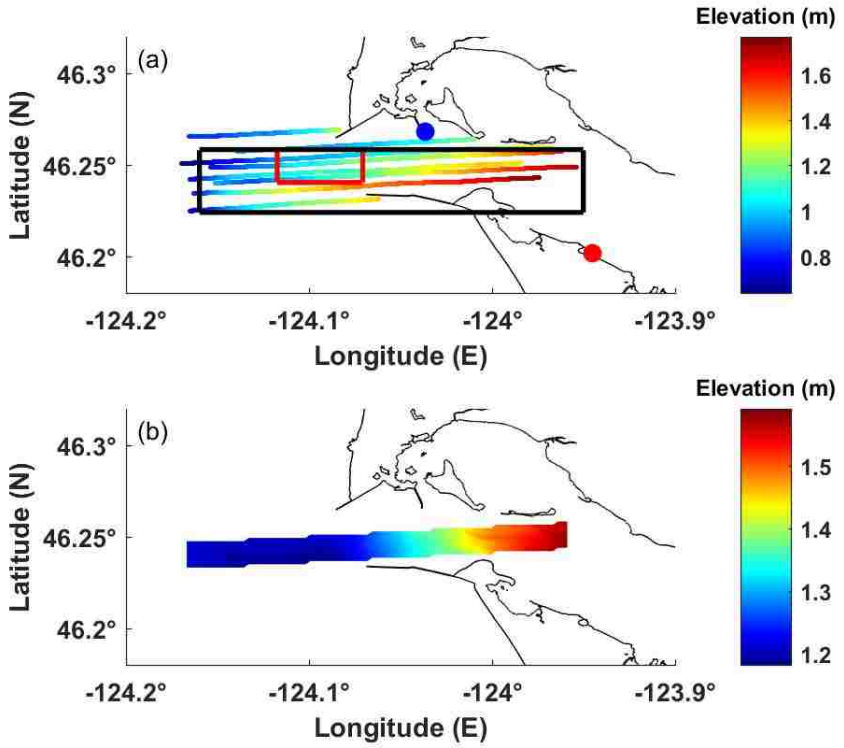

Figure 2.3: (a) Water surface elevation measured by Lidar during eight flight transects on May 26th. Location of the focus area (red box) where Lidar water surface elevation measurements were compared with concurrent in situ data collected at the NOAA Hammond tidal gauge (red dot) and historical data collected at the NOAA Jetty A tidal gauge (blue dot). Location of the Lidar water surface elevation measurements (black box) used in the surface slope calculations. (b) Model water surface elevation values used to calculate a model predicted surface slope.

2.2.3 Lidar measurement of elevation

Water surface elevation, η, is calculated with respect to mean sea level (MSL) using the Lidar, GPS, and the IMU. Three geometric corrections are applied to the raw Lidar distance measurement to obtain a corrected distance L. First, the distance between the Lidar and the IMU is added to give a new vector. This vector is then multiplied by a rotation matrix to obtain a vector whose z component is the vertical distance between the IMU and the water. The vertical distance between the IMU and GPS is then added to that to obtain a vertical distance between the GPS and a point on the ellipsoid with the latitude and longitude

coordinates output by the GPS. The GPS also outputs its height, h, above the WGS-84 ellipsoid. The difference between the ellipsoid and MSL (as approximated by the EGM96 geoid) at a particular latitude and longitude is called the undulation, N. The undulation varies by location and depends upon the choice of geoid. The elevation, η, of the water surface above or below MSL is then given as

$$\eta = h - L - N. \tag{2.1}$$

This elevation is an orthometric height which can be compared with tidal gauges. The elevation values were divided into flight transects and data were discarded on either end of the transects where the airplane was turning. Observations over land and clouds were also discarded.

Elevation values within the red box shown in Figure 2.3a were averaged spatially and temporally during each ten minute flight transect and compared with the closest concurrent tidal measurements at Hammond. The ten minute sampling time is very small compared to tidal timescales and the sampling time required for a similar measurement from a boat. I calculated the M2 amplitude by harmonic analysis (*Pawlowicz et al.*, 2002) of Lidar elevation data, concurrent Hammond data (NOAA station 9439011) and two months of hourly Jetty-A data from 1997 (NOAA Station 9440572). A reduced constituent set consisting of M2 and K1 constituents was applied due to the shortness of the record.

2.2.4 Lidar measurement of waves

The Lidar sampled at 3 kHz, which corresponds to a 0.5-1.0 m footprint and provides good resolution of the water surface elevation variation due to waves (Fig. 2.4). To isolate waves in the Lidar data a 5th order polynomial fit was subtracted from the raw elevation data. This removed any low frequency noise due to inaccurate plane motion corrections or timing errors. From this detrended data, significant wave height, h_s, was calculated as four times the standard deviation (*Dean and Dalrymple*, 1991) of 60,000 elevation measurements which roughly corresponded to 1 km of flight track. Wavelength was calculated as the inverse of the peak frequency of a wavenumber spectrum of a 2 km section of water surface elevation data.

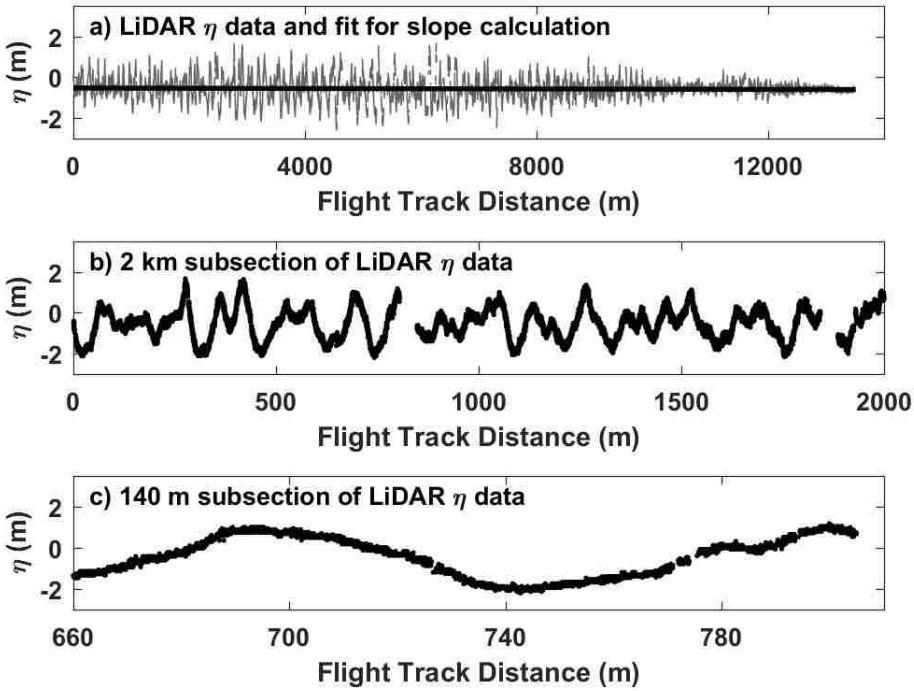

Figure 2.4: a) Example Lidar η data from one transect. The linear fit is used for the slope calculation. The airplane was flying west to east so a flight track distance of 0 is west of the mouth. b) Example of Lidar η data resolving several waves on a 2 km subsection of the transect. c) Example of Lidar η data showing an individual wave on a 140 m subsection of the transect.

Significant wave heights calculated from the Lidar data were compared with significant wave heights measured by offshore buoy 46029 (Fig. 2.1) to compute the wave amplification. Wave amplification is defined as

$$\beta = \frac{h_s}{h_{s0}} \tag{2.2}$$

where h_s is the local significant wave height and h_{s0} is the offshore significant wave height.

2.2.5 Lidar measurement of surface slope

The surface slope of each transect was calculated from a linear fit to all surface elevation data located within the black box of Figure 2.3a. Transects were excluded if they had fewer

than 100,000 points in the box or if more than half of their points in the box were missing due to land or clouds.

Surface slopes can be influenced by changes in wave heights (due to shoaling, breaking, or wave current interactions), which cause gradients in the radiation stress, S_{xx}, that depress or elevate the local mean sea level. Radiation stress is a function of the wavenumber, k, depth, d, and energy, $E = \frac{1}{16}\rho g h_s^2$. As the waves are amplified, h_s increases, subsequently increasing their energy and the radiation stress according to

$$S_{xx} = E\left(\frac{2kd}{\sinh 2kd} + \frac{1}{2}\right). \tag{2.3}$$

Gradients in radiation stress causes a change in surface slope, $\frac{\partial \eta}{\partial X}$, given by

$$\frac{dS_{xx}}{dX} = -\rho g d \frac{\partial \eta}{\partial X}. \tag{2.4}$$

2.2.6 Datasets for validation and comparison

Lidar significant wave heights were validated with measurements made by SWIFT (Surface Wave Instrument Float with Tracking) drifting wave buoys (*Thomson*, 2012). The SWIFTs estimate significant wave height using spectra of ten minute bursts of GPS Doppler velocities as a measure of wave orbital motion (*Herbers et al.*, 2012). They were deployed on five of the same days as the Lidar, and were released east of the jetties on ebb tide to drift out through the mouth. On some days they drifted back towards the mouth on flood tide but on other days they drifted north or south of the mouth with the prevailing current.

Lidar measurements of elevation, surface slope, and wave amplification were compared with numerical simulations made using the COAWST modeling system (*Warner et al.*, 2010), in which the 3D ocean circulation model (ROMS: Regional Ocean Modeling System) is two-way coupled to the phase-averaged wave propagation model (SWAN: Simulating WAves Nearshore) (*Akan et al.*, 2017). The model uses a 3-level nested grid with the highest resolution grid having a horizontal resolution of 200 m. Model predictions were made every half hour over the measurement period. Model predicted surface slope was calculated from a linear fit to model elevation values versus track distance. The location of the model elevation values used in the calculation is shown in Fig. 2.3b. The gridded model

latitudes and longitudes were first converted into universal transverse Mercator (UTM) coordinates and then into a track distance array.

Lidar measurements of tidal elevation were compared with measurements made by NOAA at the Hammond tidal gauge (Fig. 2.3a).

2.3 Results

2.3.1 Elevation

The Lidar elevations measured in the focus area at the MCR (Figure 2.3a; red box) were averaged for 260 flight transects and compared with the tidal levels measured at Hammond. The Lidar elevations agreed with the tidal elevation (Fig. 2.5) with an average difference of 0.01 m (Lidar > tidal) and RMSE of 0.39 m. The maximum tidal level measured by the Lidar was 1.0 m above MSL and the minimum was 1.96 m below MSL. The average difference is smaller than the datum uncertainty for the NOAA tide datum at the Columbia River which is 0.23 m (*NOAA*, 2015). The RMSE is similar in magnitude to previously published values of a shorter experiment comparing Lidar elevations to seven tidal gauges upriver of the mouth but the average difference is much smaller (*Hudson et al.*, 2017). The previous study used the same airborne Lidar system and found an average difference of 0.48 m with an RMSE of 0.41 m. The larger difference at the upriver locations may be due to a slightly different plane motion correction algorithm used in that study or larger datum uncertainties at the upriver location. The RMSE may be due to measurement errors or natural variability, which is discussed in more detail in section 2.4.

Harmonic analysis of the Lidar elevation data gave an M2 tidal amplitude of 0.83 +/- 0.16 m, which is in good agreement with the M2 amplitude of 0.86 +/- 0.01 m calculated from a two month long historical dataset from Jetty A (Fig. 2.3a). The Hammond data from the same time period gives an M2 amplitude of 0.93 +/- 0.00 m. This is larger than the Lidar and historical data at Jetty A, which suggests that there is amplification of the tide between Jetty A and Hammond.

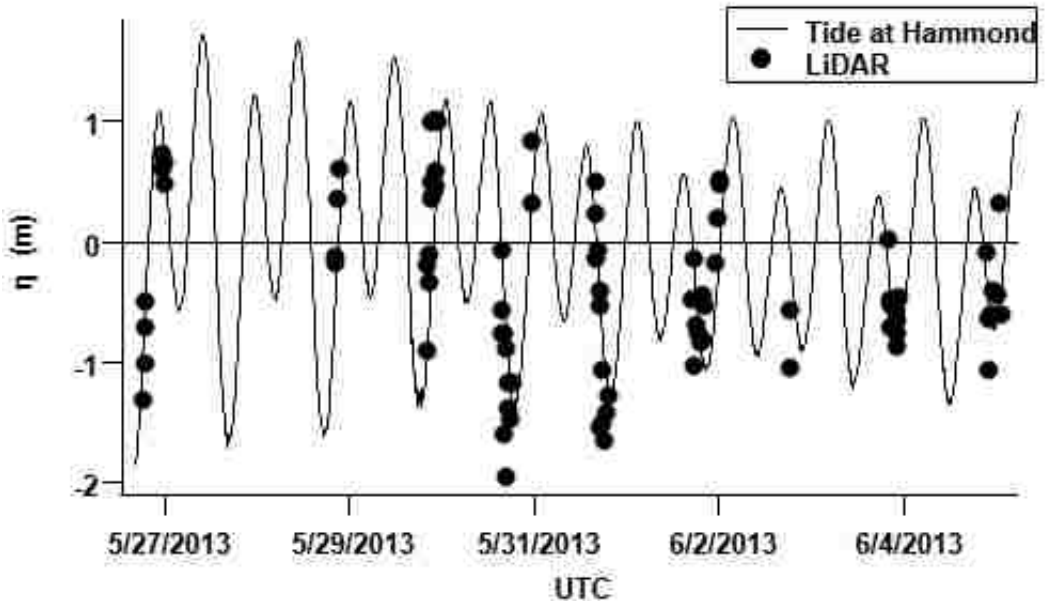

Figure 2.5: Water surface elevation from the tide gauge at Hammond and Lidar measurements inside the red box shown in Figure 2.3a.

2.3.2 Waves

Comparison with in-situ measurements

Lidar h_s measurements were compared with the SWIFT measurement that was taken closest in space to the Lidar transect. Due to logistical constraints of the sampling, Lidar transects and SWIFT drifts were chosen with as much, but no greater than 14 hours time separation. In all, 579 h_s values were compared and agreed well; the mean difference was 0.27 m (SWIFTs > Lidar) and the RMSE was 0.62 m. The maximum h_s measured by the Lidar during the comparison period was 2.25 m and the minimum was 0.55 m.

An example comparison of Lidar and SWIFT wave heights is shown in Figure 2.6 from May 26th as the SWIFTs drifted through the river mouth and the Lidar flew overhead. Both the Lidar and SWIFTs measured smaller waves ($h_s = 0.7$ m) inside the mouth east of longitude -124 and larger waves ($h_s = 1.48$ m) at the mouth near longitude -124.07. Data

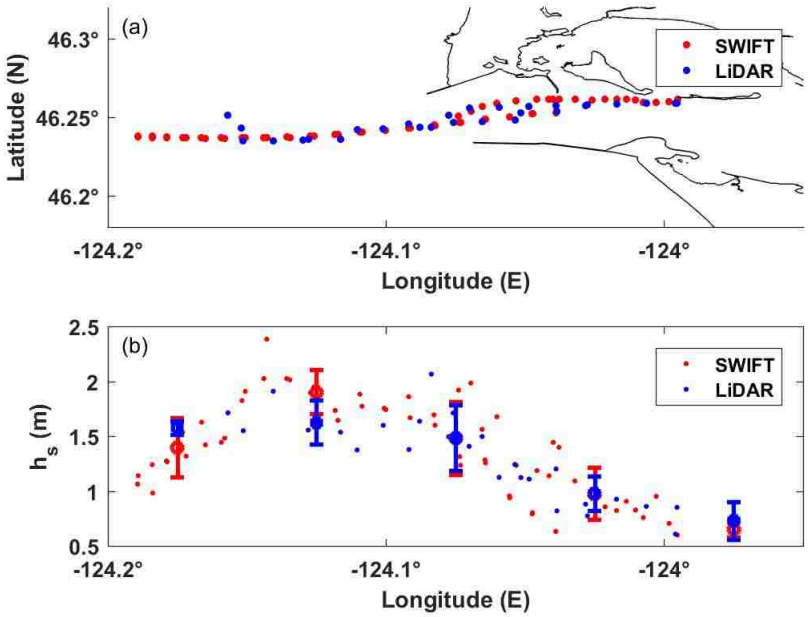

Figure 2.6: (a) Location and (b) magnitude of SWIFT and Lidar h_s measurements from May 26th.

from both platforms shows that wave heights increased further out to sea near longitude -124.125 and then decreased west of longitude -124.15.

Amplification due to wave-current interactions

Wave amplification occurs at river mouths due to the shoaling and refractive focusing of waves in shallower water and / or the action of surface currents opposing the wave propagation direction. Wave amplification was observed with the SWIFTs and Lidar, and predicted by the numerical model during ebb tides. The strongest wave amplification observed by the Lidar occurred on an ebb tide on May 31st (Fig. 2.7 a, c, e). Wave amplification derived from the Lidar, β_{Lidar}, was calculated using (2) with h_s measured by the Lidar referenced to h_{s0} measured by wave buoy 46029 offshore. The Lidar flight began around 16:00 and showed amplification close to the mouth. As the tide continued to ebb, the region of wave amplification extended further out into the ocean and became stronger near the mouth.

The flight continued until 19:00 when the amplification was still present but had decreased in magnitude.

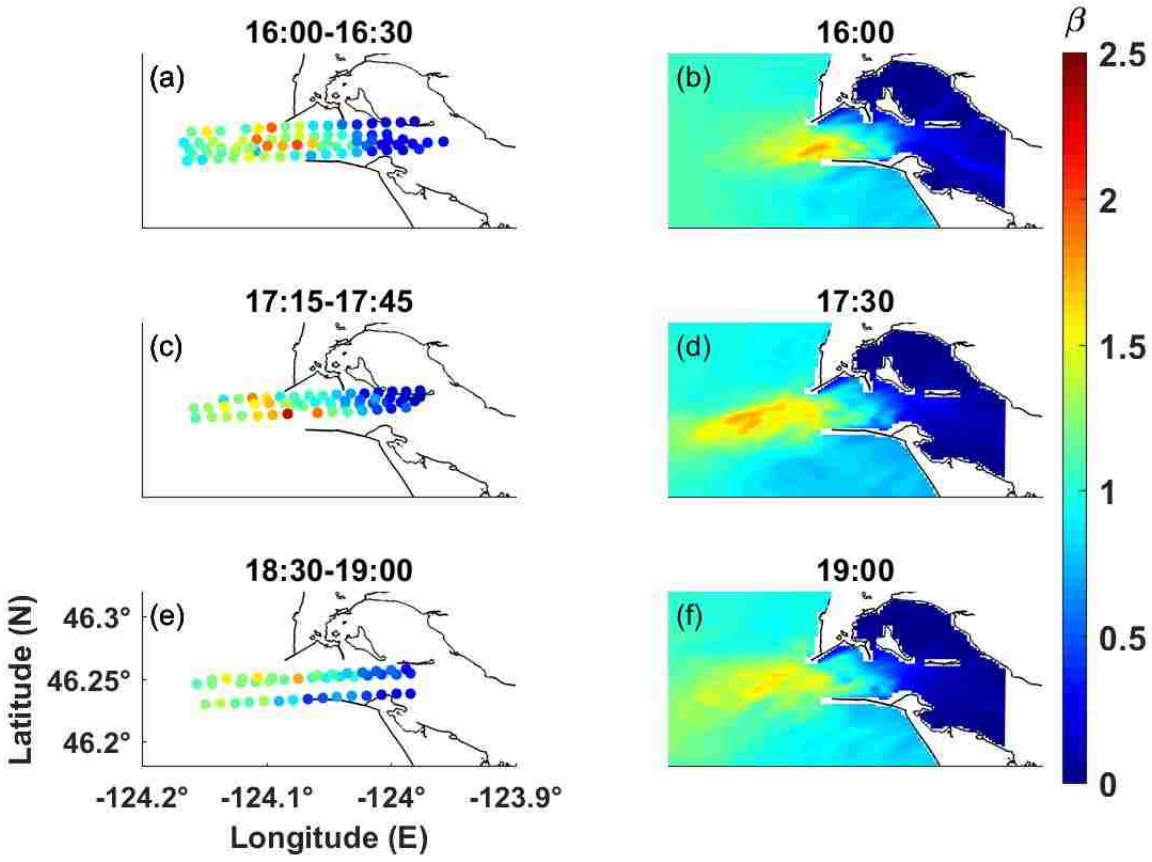

Figure 2.7: Maps of wave amplification measured by the Lidar (a, c, e) and calculated by the model (b, d, f) during an ebb tide on May 31st

The modeled wave amplification β_{model} was calculated using (2) with h_s calculated by the model and referenced to h_{s0} measured by wave buoy 46029 offshore. The model agreed with the Lidar, showing wave amplification beginning near the mouth at 16:00, spreading further into the ocean by 17:30, and decreasing in magnitude but not extent by 19:00 (Fig. 2.7 b, d, f).

Wave amplification at the MCR occurs as the waves propagate shoreward into shallower water and into a strong opposing ebb current. I further investigate the observed amplifica-

tion by analyzing the current, significant wave heights, and depth along a single transect of the May 31 flight. This one-dimensional analysis obscures the distinction between shoaling and refractive focusing over horizontal gradients in the bathymetry and the currents. Both are important processes at river mouths; this analysis quantifies the net combined effect of these processes. The westward current peaks between longitudes -124.1 and -124.2, which is also where the significant wave heights peak (Fig. 2.8a, b). The depth is shallower where this peak occurs (Fig. 2.8d), but I do not observe a response in wave height to every change in bathymetry east of this (Fig. 2.8a, d). Most of the waves on the flight transect shown in Figure 2.8 are intermediate waves ($\frac{d}{\lambda} < 0.5$), meaning that their wave heights are affected by the bottom and will increase as the depth decreases. As they propagate further east of -124.03, they encounter deeper water and lower opposing velocities, leading to decreased wave heights. Reductions in wave heights also are caused by wave breaking just west of -124.03 (*Zippel and Thomson*, 2017).

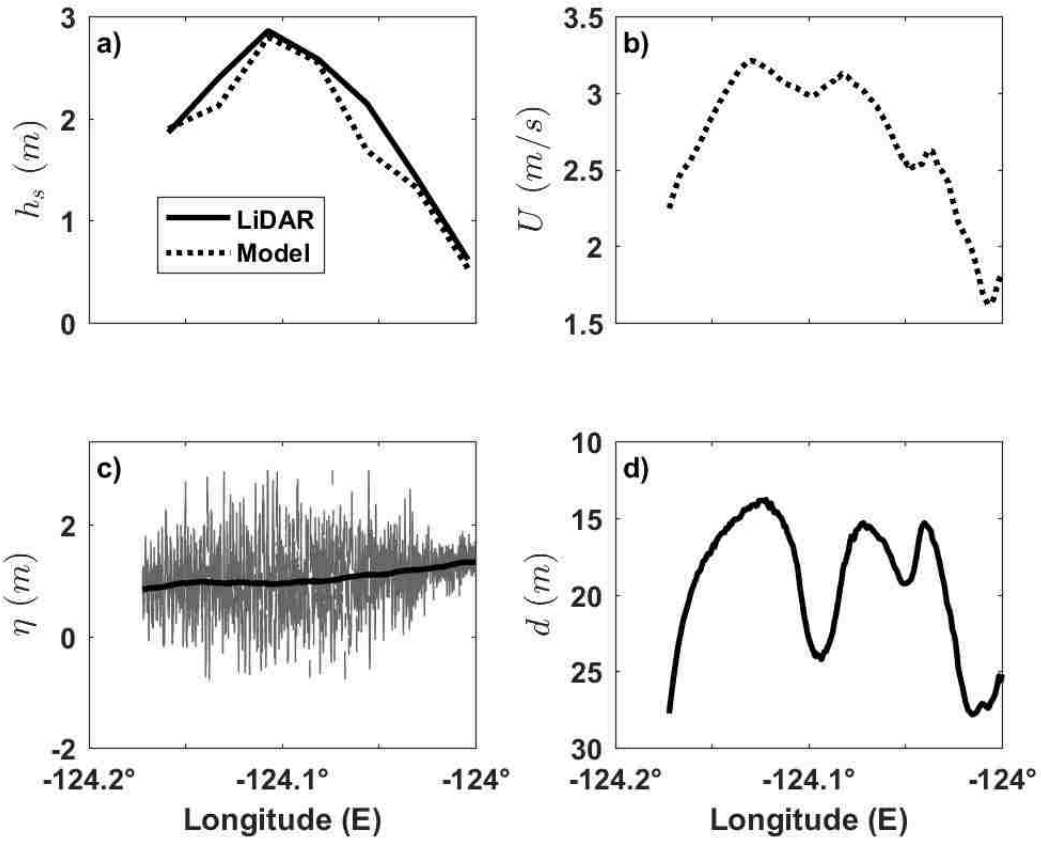

Figure 2.8: a) Significant wave heights, h_s, b) westward current velocity, U, c) surface elevation, η, and d) water depth, d, plotted vs. longitude. Data were acquired during ebb tide on May 31st along the 16:14-16:19 flight transect.

Analysis of seven transects from the flight shown in Figure 2.7 confirms that the wave amplification is dependent upon both current velocity and depth (Fig. 2.9). Wave amplification increases as the current increases and is stronger when η is below mean sea level due to shoaling. These results agree with the findings of *Gonazález* (1984) who came to the conclusion that wave-current interactions are the dominant physical mechanism governing wave amplification with bathymetric effects being of secondary importance. The related processes of wave breaking, refraction, and diffraction are not separated here, but likely all affect wave amplification. Although wave amplification is a complicated process at the MCR, Figure 2.9 demonstrates that it can be estimated from remotely sensed data. Due

to the dominant dependence on the opposing velocity, this presents a possible opportunity to estimate the river velocity from the wave amplification and water surface elevation measurements.

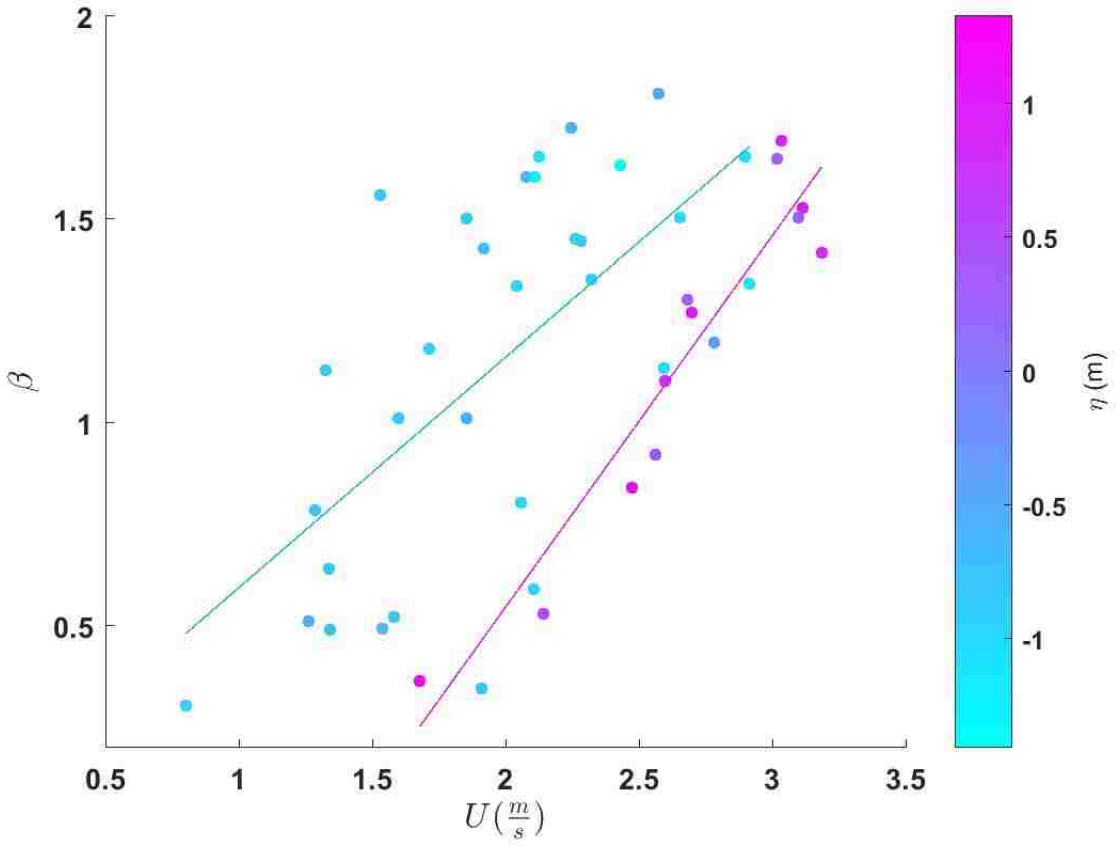

Figure 2.9: Wave amplification, β, as a function of westward current velocity, U, and water surface elevation, η. Linear fits are to all points where the water surface is above (magenta) and below (turquoise) mean sea level (MSL). MSL corresponds to $\eta = 0$.

2.3.3 Surface slope

The surface slope was calculated for each Lidar transect and compared with slope estimated from the numerical model output. The minimum and maximum measured slopes were $-0.000\,048$ and $0.000\,063$, corresponding to flood and ebb tides, respectively. Here, positive slopes are associated with higher water east of the mouth. Four Lidar transects are shown

in Figure 2.10 (a, b, c, d) during different tidal phases. The slope is negative on flood tide and positive on ebb. There is a kink in the ebb tide slope near -124.015 when η is below MSL (0) (Fig. 2.10 c). The model predictions agree with this pattern and are plotted for an entire tidal cycle (2.10 e, f, g, h). The model transects show a progression from negative slope on flood increasing to zero at high tide (Fig. 2.10 e), increasing to a positive slope with a kink below MSL on ebb (Fig. 2.10 f, g), and then decreasing from zero to a negative slope on ebb again (Fig. 2.10 h).

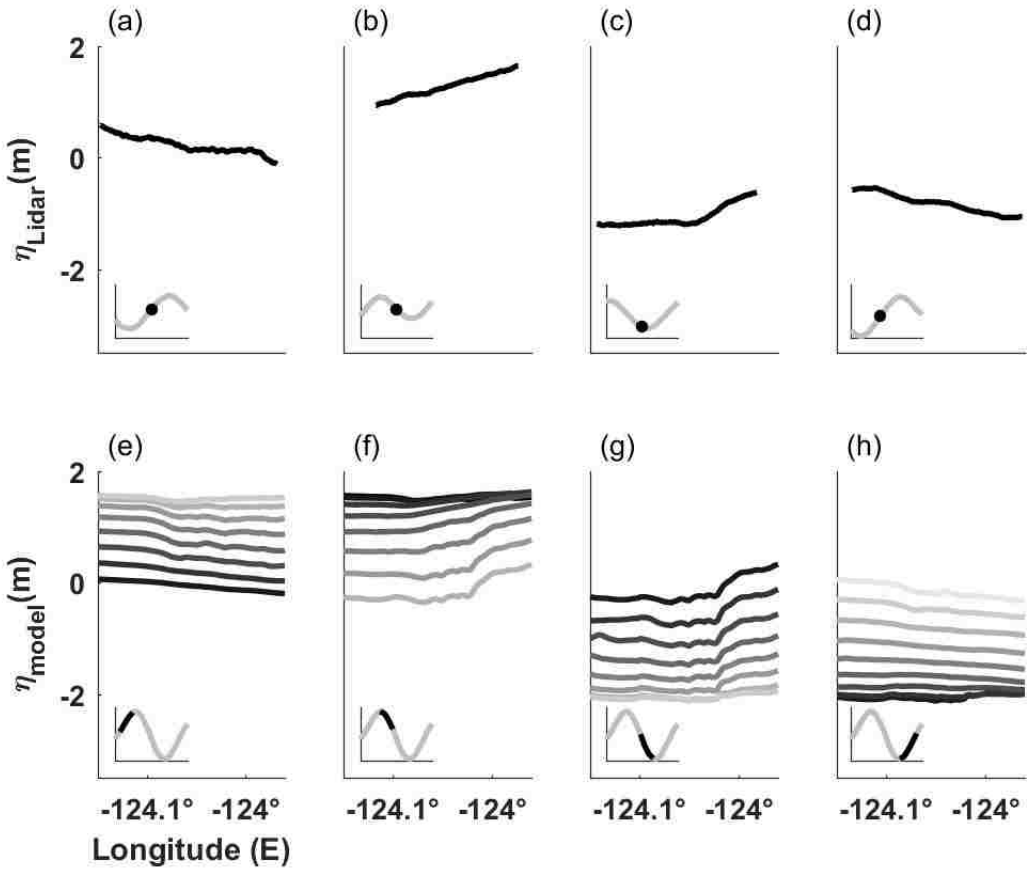

Figure 2.10: Lidar (a, b, c, d) and model (e, f, g, h) examples of the water surface elevation profiles during 4 phases of the tide. The Lidar profiles are from different tides because the Lidar never sampled a whole tidal cycle. The model profiles are all from the same tidal cycle. Time increments of the model profiles are 0.5 hours and time increases from the black line to the gray line.

The slopes calculated from the linear fits of the Lidar transect data were compared with the model slopes extracted at the same times. The average difference was 0.000 008 1 and the RMS of the difference was 0.000 019 with the average Lidar slope greater than the average model slope. A linear fit of the Lidar slopes vs the model slopes gave an r^2 value of 0.39 (Fig. 2.11 a). The differences between the Lidar and model slopes could be due to Lidar measurement errors or natural variability not resolved by the model. Sources of error and natural variability are discussed in section 2.4.

In order to investigate the Lidar and the model slopes in more detail, the slope of each Lidar transect was plotted versus time from high tide, averaged in half hour bins from high tide, and plotted with the half hour averages of the corresponding model slopes (Fig. 2.11 b). Both Lidar and model slopes show a sinusoidal pattern, with positive slopes during ebb and negative slopes during flood. After high tide the slope increases from zero as the tide ebbs and reaches its maximum slope two hours after high tide. It then continues to decrease during ebb until reaching zero at the end of ebb tide. As the tide changes to flood, the slope becomes negative and decreases to the minimum (negative) slope eleven hours after high tide. It then increases back to zero slope as high tide is approached. The Lidar measurements resolved the tidal variations and the model predictions agreed with the Lidar within the error bars for most of the tidal cycle (Fig 11 b). The tidal variation is strong in the average signal but the slope of each individual transect differs from the average due to the size of the tide and other factors such as measurement error, discharge, intermediate scale flow structures, upwelling, and wave setup.

2.3.4 Slope changes from wave-current interactions

Slope changes from wave-current interactions were investigated by examining gradients in energy and radiation stress in the cross-shore direction. Energy and radiation stress are related to significant wave height and will increase in areas where an opposing current amplifies the wave heights. Energy, calculated from Lidar and model h_s values, varies along the flight transect plotted in Figure 2.12 a). The energy peaks around longitude -124.1 where the significant wave height also had a peak (Fig. 2.8a). The wavelength, λ, varies

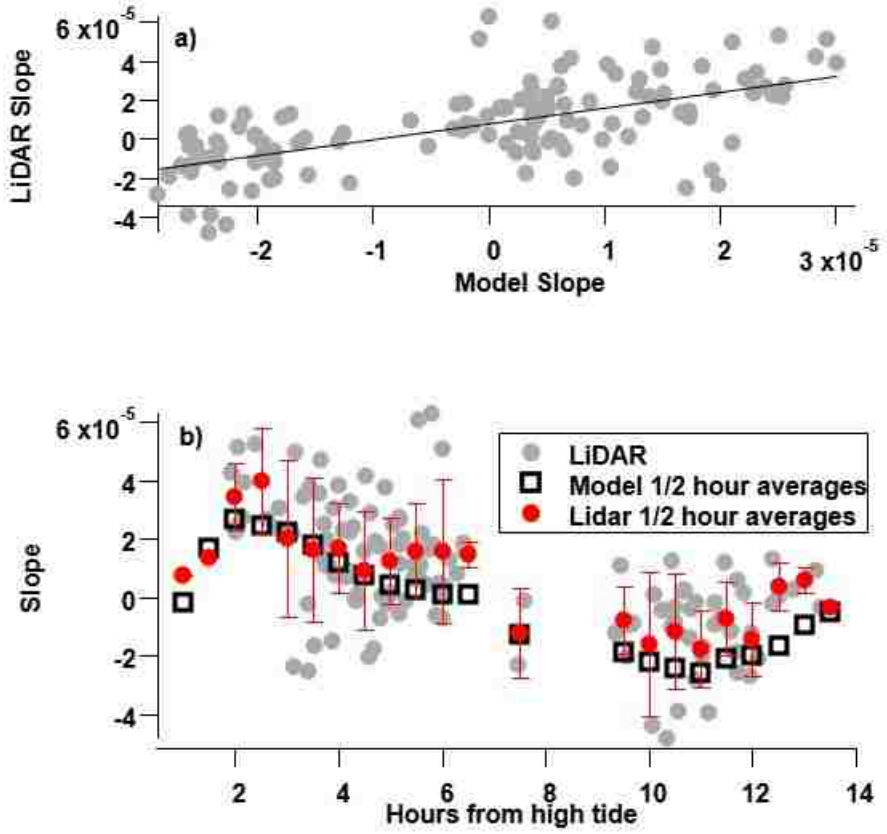

Figure 2.11: a) Slopes as measured with the Lidar and versus slopes calculated with the model. b) Slopes versus hours from high tide. Gray dots are Lidar slopes for each transect. Red dots are Lidar slope averages in half hour bins of hours from high tide with error bars of +/- 1 standard deviation. Black squares are model slope averages in half hour bins of hours from high tide.

along the flight transect (Fig. 2.12 b) but was modeled as lower than the Lidar measured for most of the track. The radiation stress also had a peak near longitude -124.1 and was lower in the model predictions due to the differing wavelengths. The surface slope due to the radiation stress divergence, $\frac{\partial \eta}{\partial X} waves$, changes from negative to positive over the length of the transect (Fig. 2.12 d). It is important to note that the estimates of the surface slope due to radiation stress gradients are an order of magnitude less than the measured surface slope. This suggests that the wave impact on surface slope is small compared with that due to tides.

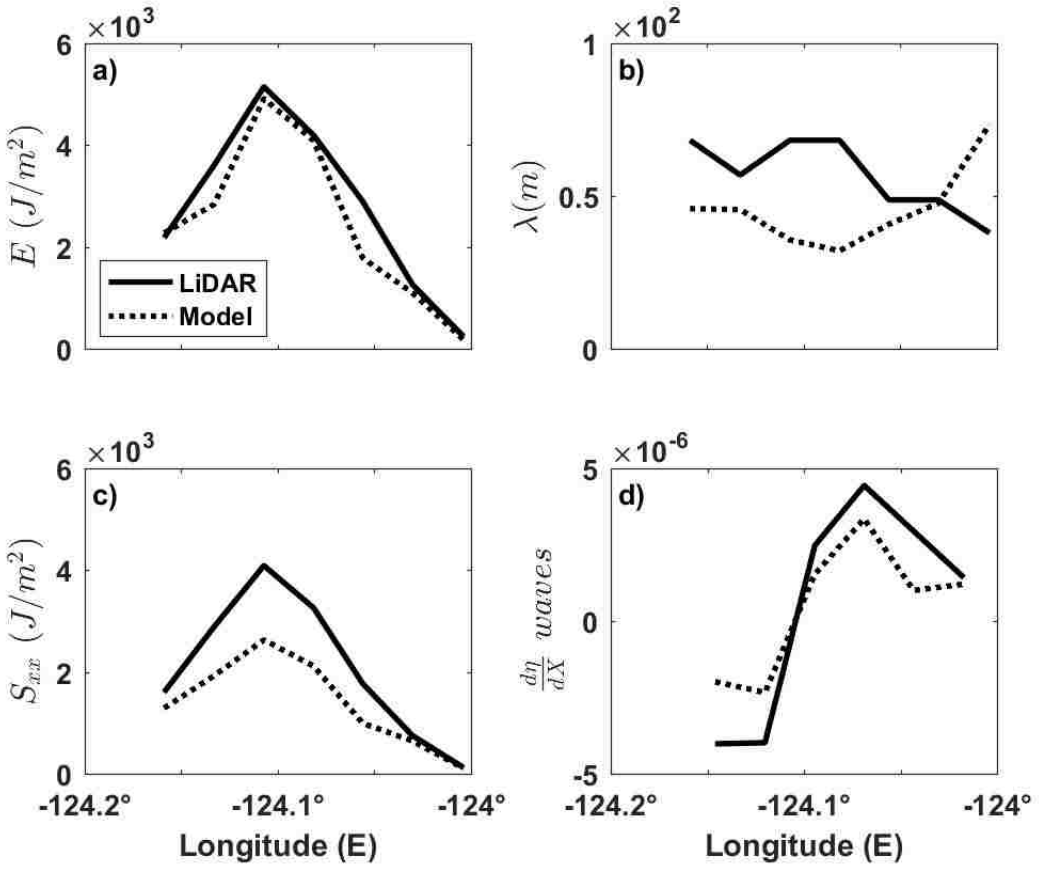

Figure 2.12: Wave energy, E, wavelength, λ, radiation stress, S_{xx}, and surface slope, $\frac{d\eta}{dX} waves$, vs. longitude along one flight transect. Data were acquired during ebb tide on May 31st along the 16:14-16:19 flight transect.

2.4 Discussion

The airborne Lidar measurements in this study resolved waves, water surface elevation, surface slope, and the changes of these parameters with the phase of the tide. A limitation of studying tidal changes using airborne Lidar is the daylight constraints of the flights. No complete tidal cycles were observed which meant changes in waves, water surface elevation, and surface slope with discharge were not resolved (Fig. 2.2). Complete tidal cycles would need to be observed under varying discharge conditions in order to separate out the tidal effects and determine whether discharge can be resolved. Waves were found to also influence the water surface elevation and surface slope, so a complete discharge study would require measurements of tidal cycles with similar offshore wave conditions.

The accuracy of the Lidar measurement of water surface elevation was determined by a comparison with the closest tidal gauge. The Lidar measurements compared so well with the tide gauge that the average difference of 0.01 m was smaller than the tide gauge datum uncertainty and the quoted Lidar instrument accuracy. The RMSE of 0.39 m was larger than the average difference and suggests errors which change in space or time rather than constant offset errors. Differences between the Lidar and tide gauge measurements may be due to measurement error or natural variability.

Measurement errors could cause a constant offset in the Lidar distance measurements or a time varying offset which depends on factors such as pitch and roll or location of the airplane. One example of a measurement error would be an incorrect distance between tide gauge MSL and the geoid height. Uncertainty between the tide gauge MSL and the geoid can be on the order of 1 m (*Hudson et al.*, 2017; *NOAA*, 2015) and may vary by location. The uncertainty between the tide gauge MSL and the geoid could have been larger in the location of the previous upriver experiment, causing a higher average difference between the Lidar elevation and the tide gauge elevation.

Another possible source of measurement error is a time offset or drift between the IMU and the Lidar. This would impact the calculation of η in equation (2.1) because H and L would not be collocated. If H and L are not collocated and the airplane is not flying at a constant altitude, then an incorrect L value would be used in equation (2.1). This type of

error is removed in the significant wave height calculation by the subtraction of the polynomial fit but it would have a large impact on the tidal elevation and slope measurements. An attempt was made to correct this possible error by using a method based on Taylor's series expansion (*Hudson et al.*, 2017).

Differences due to natural variability could be caused by the spatial separation between the tide gauge at Hammond and the location where the Lidar measured elevation. The water level is not the same at the mouth where the Lidar measured and at Hammond due to the propagation of the tidal wave. This difference varies with the phase of the tide. The level at Hammond would be higher than at the mouth during ebb and lower during flood. Harmonic analysis of the Hammond data and historical data at Jetty A showed different amplitudes of the M2 tide implying amplification of the tide between the two locations. Amplification of the tide would lead to non-linearly related water levels at the two locations.

In addition, the model output includes intermediate scale flow structures near the north jetty (Fig. 2.13a). These structures modulate the water elevation on spatial scales shorter than the Lidar transect and may also affect the tidal elevation and slope measurements. In particular, such structures are expected to display significantly more randomness than the tidal and discharge signals. While it is quite possible that the model captures these structures in a statistical sense, I do not expect that individual structures are well resolved. Since the water surface slopes on the edges of these structures are of a similar magnitude to the transect slopes, they may introduce a significant source of variability in the comparison between the Lidar measurements and the model slope outputs. Nonetheless, I observe evidence of such structures in both the Lidar and model, and they occasionally correspond in time. Figure 2.13b shows Lidar and model elevation data extracted for the Lidar flight transect shown in Figure 2.13a. The deviation from a more linear elevation profile (Figure 2.13b) appears to be associated with the presence of intermediate scale structures (Figure 2.13a), and is captured in the Lidar data. However, the variability east of the jetties differs and would lead to different computed slope values.

Surface slope has been previously studied with Lidar measurements upriver of where my measurements were made and found to be 0.000 018 (*Hudson et al.*, 2017). I observe slopes with a similar magnitude during ebb tide but larger and smaller slopes were also

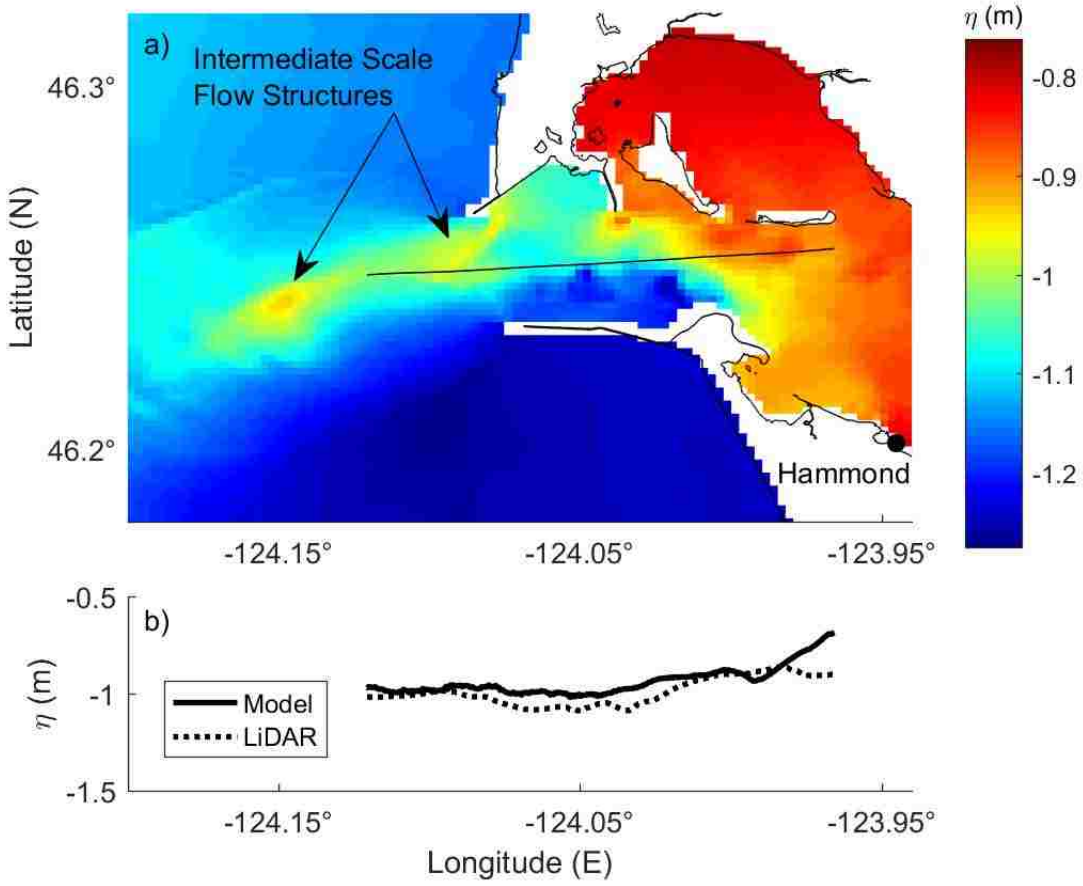

Figure 2.13: a) Model derived water surface elevations showing intermediate scale flow structures. Lidar flight transect location is shown as a black line. Black dot shows the location of the tidal gauge at Hammond. b) Model and Lidar water surface elevations along the flight transect.

measured due to the strong tidal signal near the mouth. The slope of 0.000 018 reported in (*Hudson et al.*, 2017) is a slope averaged over the tidal cycle from river kilometer 15 to river kilometer 75. They also reported a slope change near river kilometer 40 which they propose was due to changes in the river width. I would not expect my slope measurements to agree perfectly with those reported in *Hudson et al.* (2017) because the measurements were taken at different times and locations. Surface slope is expected to be dependent upon river width, phase of the tide, size of the tide, and discharge (*Jay et al.*, 2010).

The magnitude of surface slopes measured at the river mouth with Lidar indicate that SWOT may be able to resolve flood and ebb tidal variations. Average values of the water surface slope determined from the Lidar measurements are approximately 0.000 035 and −0.000 018 at peak flood and peak ebb, respectively, and corresponding model estimates are approximately 0.000 022 and −0.000 022 (Figure 2.11b). SWOT's slope accuracy is projected to be 0.000 017 (*Biancamaria et al.*, 2016), suggesting that the measured and modeled peak tidal slopes are within a factor of one or two of the projected accuracy. This puts the SWOT accuracy on the threshold of the required accuracy; tidal peaks in slope may be resolvable in a phase averaged sense over many passes, but the observed variability is likely to obscure the tidal signal in individual passes. The surface slope could also be influenced by wave current interactions but my Lidar measurements show these changes would be too small to be observable by SWOT for the relatively mild conditions measured during my experiment.

The Lidar wave height amplification study presented here is the first of its kind at a river mouth. Wave height amplification at the MCR has been modeled and studied before with waverider buoys and radar but the spatial extent of amplification has not previously been measured (*Akan et al.*, 2017; *Gonazález*, 1984; *Campana et al.*, 2016). The Lidar captured the magnitude and spatial extent of amplification during part of one ebb tide and the model agreed with those results. Lidar data were not acquired during the largest ebb tide possible at the MCR so wave amplification may be even larger in magnitude and extent on a larger ebb tide. Wave amplification caused surface slope changes but those changes were an order of magnitude smaller than changes due to the tide. These wave-driven slope changes are only indirectly related to discharge and so they risk contaminating estimates of discharge

from the surface slope at river mouths.

2.5 Conclusions

In this chapter I successfully used airborne Lidar data and a numerical model to study tidal changes at the mouth of the Columbia River. When compared with *in-situ* and model estimates, agreement was good for the following Lidar measurements:

- water surface elevation
- water surface slope
- surface gravity waves

The success of the airborne Lidar at resolving tidal changes of the water surface elevation and surface slope implies that airborne Lidar can be used to detect the tidal cycle and amplitude remotely.

Tidal variation was also detected by the Lidar in wave changes. Wave measurements showed amplification as the river velocity increased on ebb tide. The ability of the Lidar to detect wave changes with velocity leads to the possibility of remote sensing of velocity and therefore discharge as velocity increases with discharge.

Future research will be conducted to determine how waves, water surface elevation, and surface slope change with river discharge at river mouths. Discharge is often related to surface slope by Manning's equation in locations without tidal or wave influences. The work presented here documented the influence of tides and waves on the surface slope. Removal of these effects leaves the possibility of measuring discharge from water surface slope at river mouths.

Chapter 3

RIVER PLUME LIFTOFF DYNAMICS AND SURFACE EXPRESSIONS

3.1 Introduction

Coastal river discharge carries nutrients, sediments and contaminants into the coastal ocean, where the river water and its constituents play a central role in the circulation, morphology and ecosystem function of coastal waters (*Hickey and Banas*, 2003; *Syvitski et al.*, 2003; *Hickey et al.*, 2010; *Barkan et al.*, 2017). Accurate, distributed measurements of coastal river discharge are needed in order to understand river influences on coastal waters globally.

Discharge is traditionally measured using in-situ river stage gauges and rating curves (*Baldassarre and Montanari*, 2009), but measurements are sparse in some parts of the world due to either inaccessibility or economic constraints. Recently, researchers have been evaluating the feasibility of using remote measurements (*Bjerklie et al.*, 2003; *Durand et al.*, 2016; *Tuozzolo et al.*, 2019; *Nickles et al.*, 2019), which offer global coverage and the ability to estimate discharge in locations where it is difficult to install in-situ sensors. *LeFavour and Alsdorf* (2005) and *Altenau et al.* (2019) use remotely sensed water surface slope data to estimate discharge based on Manning's equation. However, the applicability of this approach is limited near the coast as Manning's equation is only valid in uniform flow conditions, where the water depth is constant through the river reach and the surface slope is parallel to the bed. Uniform flow conditions generally only occur well upstream of the river mouth and not in the 10-100 km adjustment region upriver of the mouth (*Lamb et al.*, 2012; *Chatanantavet et al.*, 2012). Between the coast and the region of uniform flow the hydraulic regime is in either a state of drawdown (M2 profile) or backwater (M1 profile), resulting in convex or concave water surface profiles, respectively (*Sturm*, 2010). Thus, estimates of discharge using Manning's equation and the water surface slope here will be over/underestimated. Alternate approaches not limited to uniform flow regions are

necessary if remote sensing data are to be used to estimate river discharge near the coast. Here I investigate the dynamics of the river plume liftoff and evaluate whether remote measurements of its surface expression could be exploited to give a more accurate estimate of the amount of freshwater entering the coastal waters.

3.2 Background

Liftoff occurs when buoyant freshwater from the river detaches from the bottom and flows over dense salty ocean water. The liftoff process is governed by two-layer hydraulics (*Armi and Farmer*, 1986) and described using the upper layer Froude number, which is the ratio of the depth averaged freshwater velocity to the gravity current propagation speed

$$Fr_1 = \frac{U_1}{\sqrt{g' h_1}}, \tag{3.1}$$

where g' is the reduced gravitational acceleration $(\Delta\rho_0/\rho_{ocean})g$, $\Delta\rho_0$ is the density contrast between fresh and ocean water, and h_1 is the depth of the freshwater flow (*Geyer and Ralston*, 2011). Liftoff occurs when the flow speed is reduced to the gravity current speed, i.e., $Fr_1 = 1$ (*MacDonald and Geyer*, 2004, 2005). This transition, and thus the liftoff location, occurs in the river channel during low discharge conditions or outside the river mouth during high discharge conditions.

Typically, discharge near the river mouth is described in terms of the freshwater Froude number

$$Fr_f = \frac{U}{\sqrt{g' h_s}}, \tag{3.2}$$

where U and h_s are the depth averaged velocity and shoreline depth, respectively. The shoreline depth is defined as the water depth at the river mouth. For a rectangular river, the Fr_f equation can be written in terms of discharge, Q, as

$$Fr_f = \frac{Q}{b_0\sqrt{g' h_s^3}}, \tag{3.3}$$

where b_0 is the width of the river at the mouth. Liftoff occurs at the river mouth when $Fr_1 = Fr_f = 1$. During low discharge conditions, $Fr_f < 1$ and the salt wedge propagates up into the channel a distance L_{sw}. The liftoff location is defined as the location of the

toe of the salt wedge (Figure 3.1a). During high discharge conditions, $Fr_f > 1$ and the freshwater stays attached to the shelf floor for a distance L_{lo} offshore until liftoff (Figure 3.1b). This distance, L_{lo}, is called the liftoff length.

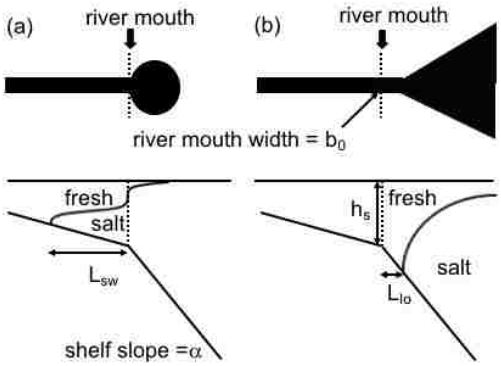

Figure 3.1: Schematic for (a) Low discharge: ($Fr_f < 1$) small plume with the salt wedge propagating up the river (b) High discharge: ($Fr_f > 1$) jet seaward of the mouth and then a large plume. The freshwater stays attached to the bottom of the shelf until liftoff. The width of the river mouth is b_0, the shelf slope is α, the depth of the water at the mouth is h_s, the length of the salt wedge is L_{sw}, and the liftoff length is L_{lo}.

Most rivers are usually in a state of low discharge ($Fr_f < 1$); however, understanding the dynamics during high discharge events is important because they are the primary drivers of morphological change (*Lamb et al.*, 2012). The process of offshore liftoff has been studied for decades due to the importance of buoyant surface jets from river and power plant outflows (*Safaie*, 1979; *Jones et al.*, 2007; *MacDonald and Geyer*, 2005). High discharge flow enters the ocean as a jet, slows due to lateral spreading and increased depth, and then lifts off when the upper layer Froude number reaches one. Using an analytical model, *Poggioli and Horner-Devine* (2018) predict that a ridge forms on the water surface with its peak at the liftoff location. The ridge becomes taller and moves further offshore as discharge increases. To my knowledge this ridge has not been measured yet, although the process of offshore liftoff has been studied before.

Previous studies of offshore liftoff have led to equations for either the depth at liftoff or the liftoff length. *Safaie* (1979) used laboratory data to obtain an empirical equation for

the depth at liftoff, $d_{lo} = 0.914 Fr_f^{1/2} h_s$. This equation can be converted to an equation for the liftoff length by approximating the depth at liftoff as $h_s + \alpha L_{lo}$, where α is the shelf slope. Defining the river mouth aspect ratio as $R_A = b_0/h_s$, the non-dimensionalized liftoff length predicted by the *Safaie* (1979) experiments is

$$\frac{L_{lo}}{b_0} = \frac{1}{\alpha R_A}(0.914 Fr_f^{1/2} - 1). \tag{3.4}$$

Jones et al. (2007) used scaling analysis based on the momentum and buoyancy of the discharge to derive a jet-to-plume length scale, $L_M = U(b_0 h_s)^{1/4}/\sqrt{g'}$, that can be expressed in terms of the freshwater Froude number as

$$\frac{L_{lo}}{b_0} = \left(\frac{1}{R_A}\right)^{3/4} Fr_f. \tag{3.5}$$

This equation was tested with measurements at the Columbia River by *Kilcher and Nash* (2010) who found their observations to be consistent with equation (3.5), but also emphasized that liftoff will only occur when the water depth is greater than one third of the jet-to-plume length scale. Therefore, any equation for the liftoff length should incorporate the depth dependence resulting from the shelf slope. Using the condition that liftoff occurs when the upper layer Froude number equals one, *Geyer and Ralston* (2011) showed that liftoff in the estuary channel occurs when the depth is

$$d_{lo} = \left(\frac{Q^2}{B^2 g'}\right)^{1/3} \tag{3.6}$$

where B is the width of the estuary. If I assume that the width of the freshwater jet offshore is the same as the width of the estuary ($b_0 = B$), and that the depth at liftoff is $h_s + \alpha L_{lo}$, then this equation predicts the following liftoff length outside the river mouth as

$$\frac{L_{lo}}{b_0} = \frac{1}{R_A \alpha}(Fr_f^{2/3} - 1). \tag{3.7}$$

The assumption that the width of the freshwater jet offshore is b_0 implies that the plume does not spread outside of the river mouth. While this assumption may hold for some cases, plume spreading may be important in determining the liftoff length as will be demonstrated in this work.

Recently, *Poggioli and Horner-Devine* (2018) used a two-layer hydraulic model of the river, estuary, and near-field river plume to study liftoff and included lateral plume spreading due to buoyancy. The model is hydrostatic, with the density and velocity assumed to be uniform in each layer and the velocity in the lower layer assumed to be negligible. A fit of the two layer hydraulic model gave an expression for the non-dimensionalized liftoff length as

$$\frac{L_{lo}}{b_0} = \gamma(Fr_f - 1)^n \tag{3.8}$$

where γ and n are dimensionless geometric constants that are assumed to vary with b_0, h_s, and α. Increasing the shelf slope was found to decrease γ which was found to be in the range of $O(10^{-2} - 1)$. A reasonable range of n was $1 < n < 1.4$ and it was found to be only weakly dependent upon b_0, h_s, and α. As γ and n are not known a priori, equation (3.8) describes the relationship between the liftoff length and the discharge but cannot be solved for the liftoff length of a specific river system even if Q, b_0, h_s, and α are known. The full model can be run to solve for the liftoff length based on specific values of Q, b_0, h_s, and α. A single equation that relates either liftoff length or ridge height to discharge in terms of b_0, h_s, and α would be useful for quantifying discharge if a remote measurement of the liftoff length or ridge height is possible. In order to test equations for the liftoff length and ridge height, I simulate river discharge into the coastal ocean using a three-dimensional numerical model that captures more of the physical processes than the two layer hydraulic model.

Numerical models are often used to study river plume dynamics. Idealized numerical models with simplified river and coastal bathymetry were extensively utilized to study coastal ocean dynamics driven by buoyancy inputs (*Garvine*, 1982, 1984, 1987; *O'Donnell*, 1990). More recently, three-dimensional numerical models with idealized setups similar to those used in this study, have been used to investigate the fate of buoyant coastal discharges in the near- and far-field with or without wind-driven dynamics (*Yankovsky and Chapman*, 1997; *Fong and Geyer*, 2001; *Hetland*, 2005; *Jurisa and Chant*, 2013; *Cole and Hetland*, 2016). Model simulations with realistic bathymetry and field conditions have also been used to study plume spreading (*Hetland and MacDonald*, 2008; *Hetland*, 2010) and frontal

processes similar to liftoff (*Ralston et al.*, 2010, 2017). Several of these studies highlighted the importance of high grid resolution near the river mouth. My study uses a high resolution model of a generalized river to determine how discharge, α, and R_A affect the location and water surface signal of liftoff.

In this chapter, I examine the relationship between the physical parameters of the river/ocean system and the liftoff process to evaluate if liftoff has a detectable water surface signal that could be used to estimate discharge. I derive theoretical expressions for the liftoff length and ridge height that depend on discharge, shelf slope, and the river mouth width to depth aspect ratio (section 3.3). An idealized numerical model (section 3.4) is used to reproduce the dynamics of liftoff for a range of shelf slopes, aspect ratios, and discharge values including when the salt wedge is present and when liftoff occurs outside the river mouth. Modeled estimates of liftoff lengths and ridge heights are compared to predictions by the equations presented in section 3.3, and momentum balances are examined to understand why a ridge forms (section 3.5). In section 3.6 I discuss two important processes, plume spreading and tides, that influence the liftoff process and may impact its detectability. I also compare the magnitude of the predicted liftoff water surface expression to the resolution of the upcoming SWOT altimeter in order to gauge the feasibility of a remote algorithm based on this approach. Lastly, I present my final conclusions and suggestions for future work (section 3.7).

3.3 Theory

Here I present derivations for the liftoff length and ridge height in terms of Q, b_0, h_s, α, and a spreading parameter κ. All of these variables that can be estimated or measured directly for most rivers except κ. I determine the range of values for κ in section 3.6.2.

3.3.1 Liftoff Length

I derive an equation for L_{lo} based on the assumption that the plume spreads on both sides at the speed of a gravity current, $\sqrt{g'h_1}$. The plume width, b, varies according to

$Udb/dx = 2\sqrt{g'h_1}$, which yields

$$\frac{db}{dx} = \frac{\kappa}{Fr_1}, \tag{3.9}$$

where κ is 2 for a surface trapped plume (*Hetland*, 2010; *Poggioli and Horner-Devine*, 2018). When the plume is not trapped at the surface, but instead attached to the bottom until the liftoff location, κ is between 0 and 1 (*Poggioli and Horner-Devine*, 2018). As the plume propagates away from the mouth the depth increases, the cross-sectional area of the plume increases and Fr_1 decreases toward 1. To capture this, the Froude number can be expressed in terms of the cross-sectional area, A, and depth h_1 as

$$Fr_1 = \frac{Q}{A\sqrt{g'h_1}}. \tag{3.10}$$

To account for the variation in A with x, I approximate the plume cross-section as a rectangle of width b and allow h_1 to increase linearly from h_s at the mouth according to the shelf slope α, $h_1 = h_s + \alpha x$. Thus, the area is

$$A = b(h_s + \alpha x). \tag{3.11}$$

Substituting (3.10) and (3.11) into (3.9) and integrating from b_0 to b yields an expression for the axial variation of the plume width in terms of the freshwater Froude number.

$$\frac{b}{b_0} = exp\left[\frac{\Gamma}{Fr_f}(h_*^{5/2} - 1)\right] \tag{3.12}$$

Here, $h_* = 1 + \alpha x/h_s$ is the dimensionless plume thickness before liftoff and $\Gamma = 2\kappa/(5\alpha R_A)$ is a parameter accounting for the spreading rate, shelf slope, and river mouth aspect ratio. Note that variations in the surface elevation, which are typically less than 2% of the flow depth (see Figure 3.5) are ignored in this formulation. At liftoff $Fr_1 = 1$, $x = L_{lo}$, and Q in equation (3.10) can be written in terms of Fr_f which gives

$$Fr_f = \left(1 + \frac{\alpha L_{lo}}{h_s}\right)^{3/2}\left[exp\left\{\frac{\Gamma}{Fr_f}\left(\left(1 + \frac{\alpha L_{lo}}{h_s}\right)^{5/2} - 1\right)\right\}\right]. \tag{3.13}$$

Equation (3.13) provides an implicit expression relating L_{lo} to Fr_f. For a known Fr_f, equation (3.13) can be solved using numerical methods to estimate L_{lo}. If I consider the case where plume spreading is negligible by setting κ to zero, then equation (3.13) reduces to

$$Fr_f = \left(1 + \frac{\alpha L_{lo}}{h_s}\right)^{3/2}, \tag{3.14}$$

which can be solved for the non-dimensionalized liftoff length

$$\frac{L_{lo}}{b_0} = \frac{1}{R_A \alpha}(Fr_f^{2/3} - 1). \tag{3.15}$$

This equation is equivalent to equation (3.7), which was derived by assuming a critical depth and zero offshore spreading (*Geyer and Ralston*, 2011). In section 3.6.2 I show that spreading is low when α is large enough such that Γ approaches zero. In this case, equation (3.15) provides a good estimate of L_{lo}.

3.3.2 Ridge height

I derive an equation for ridge height based on the steady one-dimensional x-momentum equation,

$$\bar{u}\frac{\partial \bar{u}}{\partial x} = -g\frac{\partial \eta}{\partial x} - \frac{C_D \bar{u^2}}{h}. \tag{3.16}$$

Equation (3.16) can be further simplified assuming a rectangular plume of area, A, (equ. 3.11), quadratic bottom drag with drag coefficient C_D, and $\bar{u} = Q/A$. Substituting b from equation (3.12) into equation (3.16) gives an expression for the water surface slope in terms of the non-dimensional depth

$$\frac{\partial \eta}{\partial h_*} = \frac{Q^2}{A^3 g}\frac{\partial A}{\partial h_*} - \frac{C_D h_s}{h \alpha g}\left(\frac{Q^2}{A^2}\right), \tag{3.17}$$

which can be integrated between the river mouth and the liftoff location to arrive at an expression for the ridge height, h_{ridge}

$$\frac{h_{ridge}}{h_s} = \frac{g'}{g} Fr_f^2 \left\{ \int_1^{1+\frac{\alpha L_{lo}}{h_s}} \frac{\frac{\Gamma}{Fr_f} 2.5 h_*^{5/2} + 1 - \frac{C_D}{\alpha}}{h_*^3 exp[\frac{2\Gamma}{Fr_f}(h_*^{5/2} - 1)]} \partial h_* \right\}. \tag{3.18}$$

When plume spreading is negligible ($\kappa = 0$), the integral simplifies to

$$\frac{h_{ridge}}{h_s} = \frac{1}{2}\frac{g'}{g}\left[\left(1 - \frac{C_D}{\alpha}\right)\left(Fr_f^2 - Fr_f^{2/3}\right)\right]. \tag{3.19}$$

The details of this ridge height derivation can be found in the Appendix.

3.4 Methods

3.4.1 Model description and configuration

In this study, I use the Regional Ocean Modeling System, ROMS (*Shchepetkin and McWilliams*, 2005), to investigate liftoff dynamics and water surface elevation changes with discharge. ROMS is a three-dimensional, free surface, primitive equation ocean model using orthogonal curvilinear coordinates in the horizontal direction and S-coordinates in the vertical direction. It solves finite-difference approximations of the Reynolds-averaged Navier-Stokes equations using the Boussinesq and hydrostatic approximations (*Shchepetkin and McWilliams*, 2005, 2009). ROMS was run in an idealized river/ocean system similar to configurations used by *Hetland* (2005), *Cole and Hetland* (2016), and *Qu and Hetland* (2019). This section describes the model configuration and the physical parameters used in the numerical simulations.

The model domain is 35 km in the alongshore direction and 48 km in the cross-shore direction (Figure 3.2). It has a 10 km long, 1.025 km wide, rectangular river that is lengthened to 61 km for low discharge runs to contain the salt wedge. The river has a bottom slope of 0.0001 and empties into an ocean with a constant shelf slope, vertical coastal wall, and 30 sigma layers with resolution focused near the surface and the bottom (Figure 3.2d). Shelf slopes of 0.001, 0.002, and 0.005 were chosen for comparison with previous studies e.g., *Yankovsky and Chapman* (1997), and *Poggioli and Horner-Devine* (2018). Sensitivity studies were conducted to determine the minimum resolution necessary to resolve the dynamics of plume liftoff and spreading near the mouth. The resolution in the cross-shore direction varies from 25 m to 200 m with the highest resolution at the river mouth. Water temperatures in the ocean and river water were set to 25 C to limit density differences to those due to salinity. The initial conditions were flow at rest and an ocean salinity of 32 psu. Chapman and Flather boundary conditions were used for sea-surface elevation and barotropic velocities, and gradient boundary conditions were used for baroclinic flows, temperature, and salinity. Quadratic drag was assumed for the bottom with a drag coefficient, $C_d = 0.003$. A $k - \epsilon$ turbulence closure scheme was used as the vertical mixing algorithm. The time needed for the model to reach a steady state was determined to be five days as

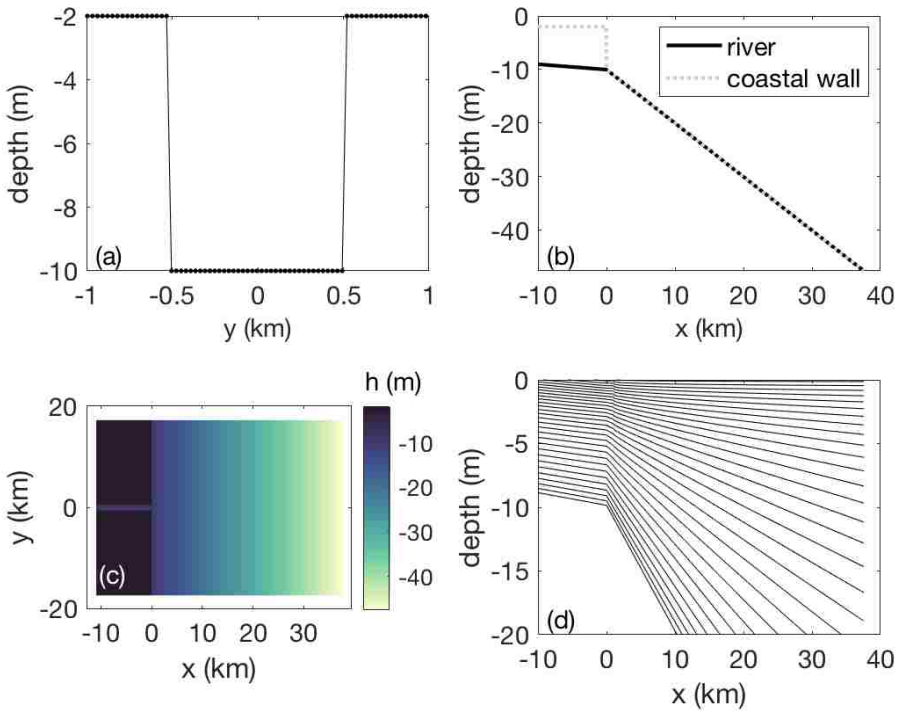

Figure 3.2: ROMS grid configuration: (a) rectangular river mouth (b) coastal wall (c) bathymetry for high Froude number runs and (d) sigma levels

the liftoff lengths were constant in time after that point. Model runs were completed for three shelf slopes, three shoreline depths, and ten discharge values characterized by their freshwater Froude numbers, as shown in Table 1.

Table 3.1: ROMS model run parameters. Low freshwater Froude numbers were 0.1, 0.2, 0.3, 0.4, and 0.5. High freshwater Froude numbers were 1.2, 2, 3, 4, and 5.

α	$h_s(m)$	Fr_f
0.001	10	low
0.001	10	high
0.002	10	high
0.005	10	high
0.005	5	high
0.005	15	high

3.4.2 Analysis Overview

The model output was analyzed differently during low and high discharge. The salinity structure was used to calculate the salt wedge length during low discharge and the liftoff length during high discharge. The water surface slope change was estimated for all conditions at the liftoff location and additionally at the river mouth during high discharge conditions. The plume spreading parameter was calculated during high discharge conditions from vertical cross-sections of salinity between the river mouth and the liftoff location.

3.4.3 Low discharge analysis

During low discharge conditions liftoff is in the channel and the distance between the river mouth and the liftoff location is the salt wedge length, L_{sw} (Figure 3.1a). Liftoff dynamics simulated for Fr_f between 0.1 and 0.5 are further investigated by examining changes in the salt wedge length and the water surface elevation. The salt wedge length is calculated as the distance between the river mouth and the location upstream where the mid-river salinity

in the bottom sigma layer is above 2 psu. Sea surface height, η, averaged over the final two days of model simulation is used to calculate the surface slope, $\frac{d\eta}{dx}$, over 10 km upriver and downriver of the toe of the salt wedge. The surface slopes above and below the toe of the salt wedge are calculated over 10 km except for the $Fr_f = 0.1$ and $Fr_f = 0.5$ flow cases. For the lowest flow case ($Fr_f = 0.1$), the toe of the salt wedge is less than 10 km from the edge of the model grid; therefore, the slope upriver of the toe is calculated between the toe and the model grid edge. For the highest flow case ($Fr_f = 0.5$), the toe of the salt wedge is less than 10 km from the river mouth; therefore, the slope downstream of the toe is calculated along the entire distance between the toe and the river mouth.

3.4.4 High discharge analysis

During high discharge conditions liftoff is outside the river mouth (Figure 3.1b) and the model output is first averaged over the final two days of simulation and then examined for different discharge, α, and R_A values. The liftoff length is calculated as the distance between the river mouth and the location of the maximum gradient of the salinity in the bottom sigma layer at the same alongshelf location as the middle of the river. The surface slope signature is quantified as the slope change between upriver and seaward of the mouth but additionally the slope change at the ridge peak is calculated. The ridge height is calculated as the height difference between the offshore peak water level and the water level at the river mouth.

3.4.5 Plume spreading analysis

Plume spreading dynamics are investigated in section 3.6.2 where I focus on the spreading parameter κ, which influences the liftoff length (eq. 3.13) and the ridge height (eq. 3.18). To calculate κ from the ROMS output the shape of the plume is found by determining which grid cells are in the plume at each location between the river mouth and the liftoff location. Grid cells are evaluated in each alongshore vertical salinity cross-section. Example alongshore vertical salinity cross-sections are shown in Figure 3.11e-f. Grid cells are considered to be in the plume if their salinity value is below a salinity threshold. The salinity threshold

is set for each vertical cross-section as the salinity where the sum of the freshwater flux in the plume grid cells is 85% of the total freshwater flux in that vertical cross-section. The plume cross-sectional area, A_{plume}, and average plume velocity, U_{plume}, are then calculated for the grid cells in the plume. The width of the spreading plume, b, is calculated as A_{plume} divided by the depth. The plume Froude number is calculated following equation (3.1) as $Fr_{\text{plume}} = \frac{U_{\text{plume}}}{\sqrt{g'h}}$ where h is the water depth. The plume spreading parameter, κ, is then calculated as $Fr_{\text{plume}}\frac{db}{dx}$ where Fr_{plume} is calculated for every vertical cross-section between the mouth and the liftoff location and then averaged, db is the width change of the plume between the mouth and the liftoff location, and dx is the distance between the mouth and the liftoff location.

3.5 Results

In this section the dependence of the liftoff process on discharge, α, and R_A is presented for both low and high discharge conditions. Modeled estimates of L_{lo} and h_{ridge} are compared to the analytical predictions (Eqs. 3.13 and 3.18) derived in section 3.3.

3.5.1 Low discharge results

Model output confirms that when $Fr_f < 1$ the salt water intrudes up through the mouth and liftoff occurs upstream in the river channel (Figure 3.3 d-f). As discharge increases, the higher flow pushes the salt wedge closer to the mouth, decreasing L_{SW} (Figure 3.3 d-f and Figure 3.4 a-b). These findings are consistent with *Poggioli and Horner-Devine* (2015) who explored the details of the relationship between L_{SW}, discharge, and channel geometry. In this study I did not conduct simulations for different channel geometries at low discharge but instead focused on the water surface signal changes with discharge.

The water surface signal associated with liftoff when $Fr_f < 1$ is a decrease of the water surface slope at the toe of the salt wedge (Figure 3.3a-c). This water surface slope change moves closer to the mouth as the discharge increases and L_{SW} decreases (Figure 3.4a-b). The slope of the upstream M1 backwater curve increases with discharge as expected for a gradually varied flow profile upstream of $x = L_{SW}$ (Figure 3.4a). Downstream of liftoff the water surface slope is small. Physically this occurs because the interfacial drag coefficient

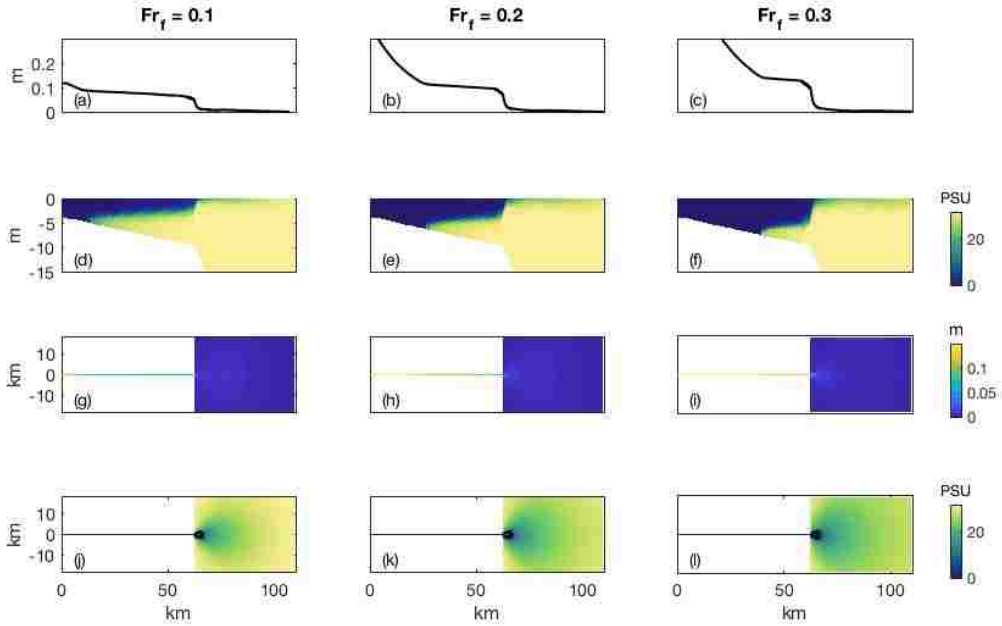

Figure 3.3: Low discharge examples of the water surface elevation and salinity structure for $\alpha = 0.001$ and $R_A = 103$: (a)-(c) Side view line plots of water surface elevation at the location of the middle of the river. (d)-(f) Side view cross-sections of salinity with depth at the location of the middle of the river. (g) – (i) Plan view images of the water surface elevation. (j)-(l) Plan view images of the surface salinity with the 6, 8, and 10 PSU contours plotted as black lines.

between the freshwater and the salt wedge is typically on the order of ten times smaller than the drag coefficient of the river bottom. For increasing discharge, the difference between the M1 slope upriver of liftoff and the slope downriver of the liftoff location increases until $Fr_f = 0.3$ where it decreases due to the short length of the salt wedge (Figure 3.4c).

Another water surface slope change occurs at the mouth of the river (Figure 3.4a) where the salinity structure changes to a laterally spreading thin surface plume (Figure 3.3d-f & j-l). This sharp change is primarily due to the plume spreading alongshore because it is no longer constrained by the river channel (Figure 3.3j-l). The dramatic slope change may be a consequence of the square edges of the modeled river mouth, which are more abrupt than natural river mouths. After the dramatic slope change at the river mouth the water surface elevation shows no structure offshore (Figure 3.3g-i).

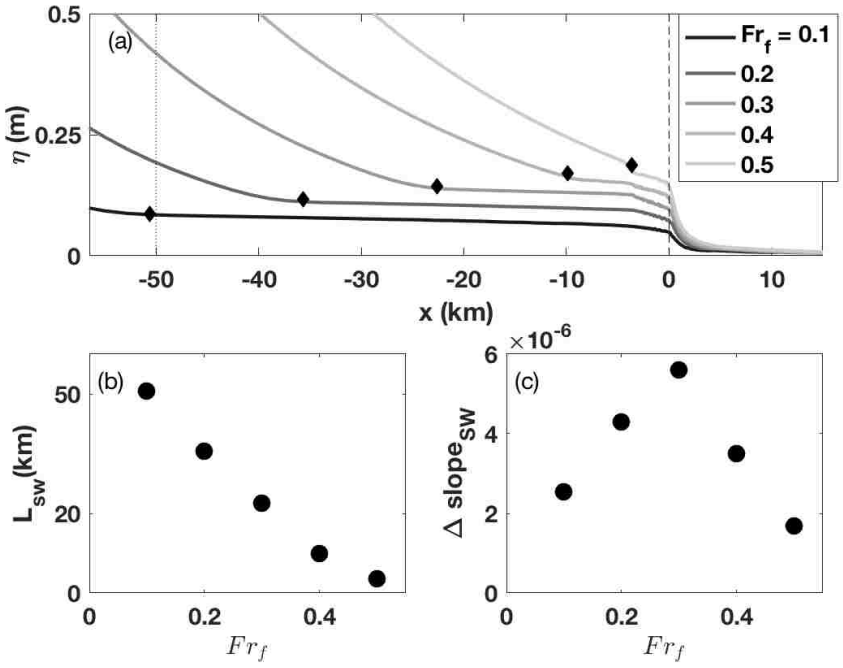

Figure 3.4: (a) Sea surface elevation, η, during low discharge for Fr_f from 0.1 to 0.5 with the toe of the salt wedge marked by a diamond, the river mouth marked with a vertical dashed line, and the location where the 5 water surface elevations are distinct by 0.1 m marked with a dotted line. (b) Salt wedge length as a function of Fr_f. (c) Water surface slope change at the toe of the salt wedge.

3.5.2 High discharge results

When $Fr_f > 1$ the freshwater exits the river mouth as a jet that stays attached to the bottom of the shelf until it has slowed down enough to lift off (Figure 3.5d-f). At the liftoff location it spreads laterally into an oval shaped plume and is confined to a near-surface layer (Figure 3.5d-f and j-l). With an increase in discharge, the size of the plume increases and the freshwater stays attached to the bottom further offshore, thus leading to an increase in L_{lo} (Figure 3.5d-f and j-l and Figure 3.6b).

In high discharge conditions, the water surface forms a three-dimensional ridge outside the river mouth, which increases in size with discharge (Figure 3.5g-i). The ridge forms on the water surface as the result of a positive surface slope between the mouth and the liftoff location and the dramatic decrease of the water surface slope at liftoff. The formation of this positive slope seaward of the mouth will be discussed further by examining the conservation of momentum in section 3.5.5.

As discharge increases the ridge peak increases in height and moves further from the mouth (Figure 3.6a). At the highest discharge corresponding to $Fr_f = 5$ the ridge becomes unstable in my simulations and no longer has the shape of a well-defined peak (Figure 3.6a). The distance between the mouth and the ridge peak is the ridge length, L_{ridge}, which for the purposes of this chapter will be considered equal to L_{lo} because the peak of the ridge is directly above the liftoff location (Figure 3.5a-f).

Upriver of the mouth the water surface slope is an M2 profile (*Sturm*, 2010), whose slope increases with discharge (Figure 3.6a). The slope change between the upriver M2 profile and the positive slope seaward of the mouth also increases with discharge (Figure 3.6c).

3.5.3 Liftoff length dependence on α and R_A

The dependence of the liftoff length on discharge, α, and R_A is explored in Figure 3.7, which shows dimensionless liftoff lengths computed from ROMS output compared with analytical model predictions of equations (3.13), and (3.15), and the *Poggioli and Horner-Devine* (2018) hydraulic model. Note that the *Poggioli and Horner-Devine* (2018) model returns no prediction for some high Fr_f values because no hydraulic solution exists. For

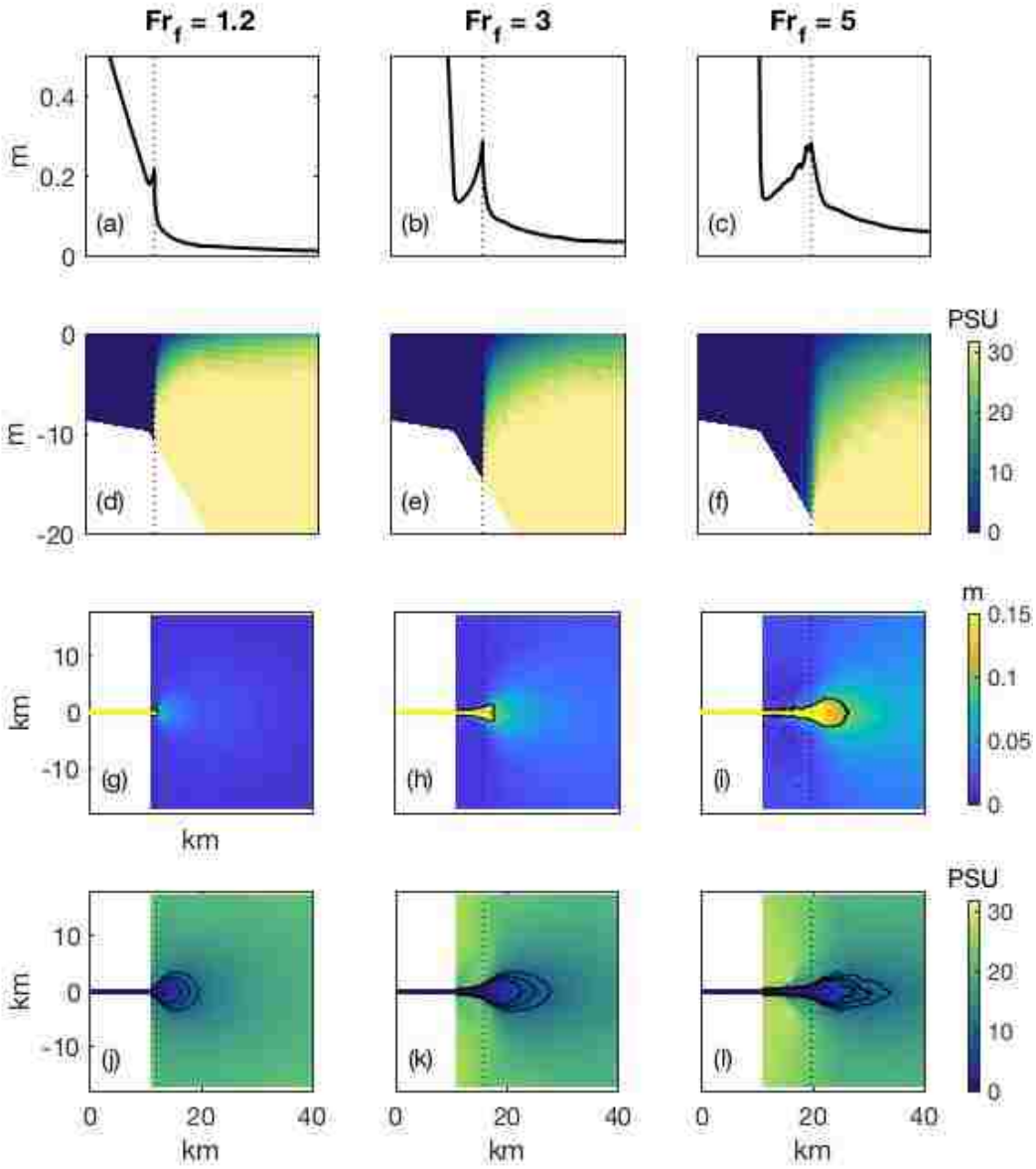

Figure 3.5: High discharge examples of the water surface elevation and salinity structure for $\alpha = 0.001$ and $R_A = 103$. The liftoff location is marked with a dotted line. (a)-(c) Side view line plots of water surface elevation at the location of the middle of the river. (d)-(f) Side view images of salinity with depth at the location of the middle of the river. (g) – (i) Plan view images of the water surface elevation with the 0.1 m elevation contour plotted as a black line. (j)-(l) Plan view images of surface salinity with the 6, 8, and 10 psu contours plotted as a black line.

all values of α and R_A, liftoff occurs further offshore as Fr_f increases, consistent with the expectation that liftoff is further away from the mouth as discharge increases (*Safaie*, 1979; *Jones et al.*, 2007; *Geyer and Ralston*, 2011; *Poggioli and Horner-Devine*, 2018). The river width is approximately 1 km so the simulated dimensional liftoff lengths are between 1 km and 8 km.

The relationship between L_{lo} and Fr_f also depends on shelf slope and river mouth aspect ratio. Higher values of α result in shorter liftoff lengths for all freshwater Froude numbers because the increase in cross-sectional area results in more rapid flow deceleration. The inverse dependence between liftoff length and shelf slope is consistent with prior models (*Safaie*, 1979; *Geyer and Ralston*, 2011; *Poggioli and Horner-Devine*, 2018). The river mouth aspect ratio also influences the liftoff location; a higher aspect ratio results in a smaller L_{lo} as predicted by *Safaie* (1979),*Jones et al.* (2007), and *Geyer and Ralston* (2011). A higher aspect ratio results in a larger bottom area relative to the plume volume, which causes an increase in the effective bottom drag on the plume. The elevated bottom drag decelerates the plume quickly and the plume lifts off close to the river mouth. It is important to note that in my simulations the channel width has been held fixed and R_A is only varied by changing h_s. I expect, however, that the same result would be obtained by changing the channel width because a larger channel width would also mean a larger bottom area relative to the plume volume. Once the channel width is larger than the Rossby radius the flow separates from the channel wall within the estuary. This process will further influence the dynamics near the river mouth, but consideration of earth's rotation is beyond the scope of the present study.

Predictions of L_{lo} based on equation (3.13) show good agreement with the ROMS results and the *Poggioli and Horner-Devine* (2018) hydraulic model for the full range of Fr_f, α, and R_A values (Figure 3.7). In these predictions, the spreading rate κ is not known *a priori*. For each set of runs with a fixed α and R_A, κ is determined by minimizing the error between the equation (3.13) and the ROMS predicted liftoff lengths for the range of Fr_f values. Thus, each thick solid line in Figure 3.7 was computed with a single value of κ, which ranges from -0.18 to 0.22. The κ values were also entered into the *Poggioli and Horner-Devine* (2018) hydraulic model to compute the L_{lo} and the predictions agree well with those of equation

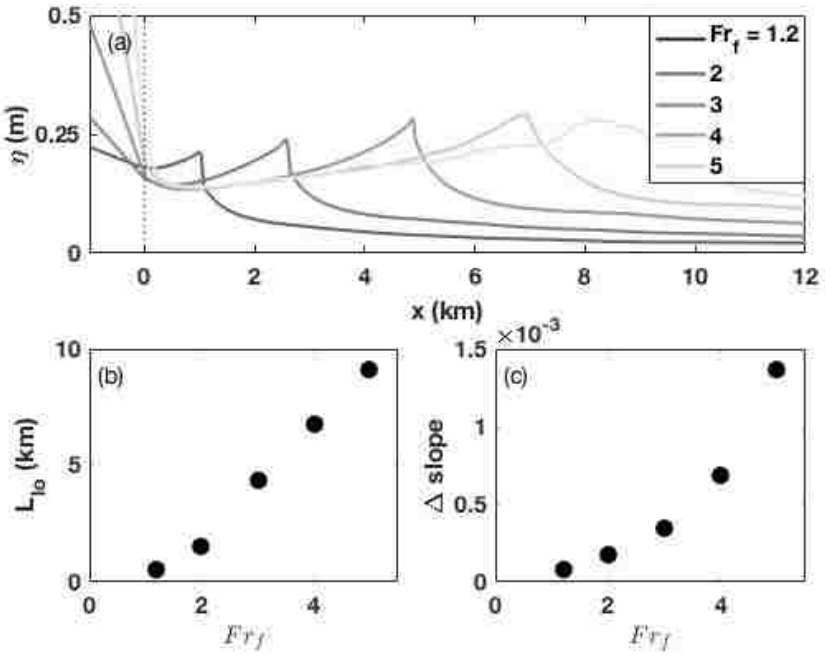

Figure 3.6: High discharge with $\alpha = 0.001$ and $R_A = 103$ (a) Sea surface height, η, versus cross-shore distance for 5 freshwater Froude numbers from 1.2 to 5. The river mouth is marked with a dotted line. (b) Liftoff length as a function of Fr_f. (c) Water surface slope change at the river mouth.

(3.13) (Figure 3.7). In section 3.6.2 I determine the spreading rate from the ROMS salinity fields directly and show that the values of κ from these fits are consistent with the observed spreading.

Predictions of L_{lo} for the case with no plume spreading ($\kappa = 0$, Eq. 3.15) are also shown in Figure 3.7. They increase with Fr_f, decrease for higher values of α (Figure 3.7a) and R_A (Figure 3.7b). The liftoff lengths predicted with Eq. 3.15 match well with those calculated from the ROMS output for the case when the shelf slope is 0.005 (Figure 3.7b). However, the agreement breaks down for lower values of the shelf slope (Figure 3.7a). This suggests that liftoff is controlled by depth variation on steep shelves and spreading has a secondary influence. Both appear to be important on gentle shelves.

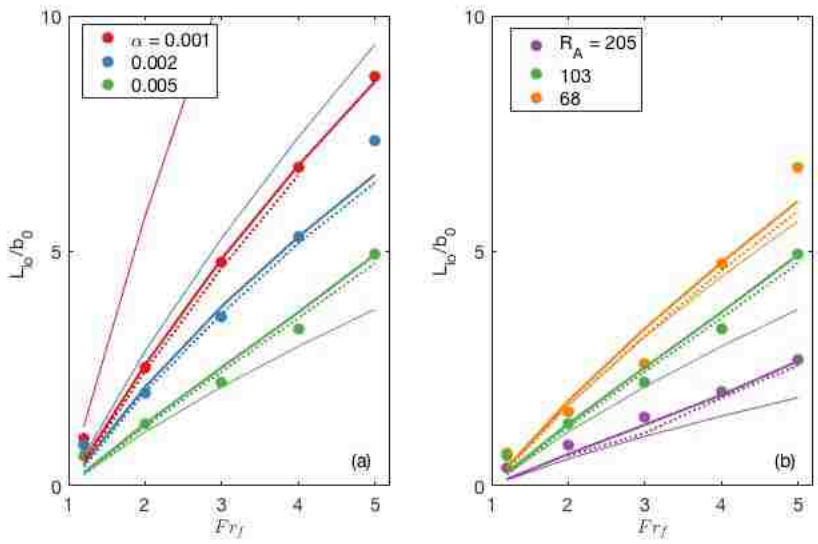

Figure 3.7: Normalized liftoff lengths versus freshwater Froude number for (a) three shelf slopes ($R_A = 103$) and (b) three river mouth aspect ratios all with a shelf slope of $\alpha = 0.005$. Filled circles are ROMS estimates, thick solid lines are calculated with equation (3.13) and κ is optimized to minimize the difference with the ROMS estimates. Thin solid lines are calculated with equation (3.15) where $\kappa = 0$ and dashed lines are calculated with the *Poggioli and Horner-Devine* (2018) model using the optimized κ values.

3.5.4 Ridge height dependence on α and R_A

The dependence of the ridge height on discharge, α, and R_A is explored in Figure 3.8. For almost all values of α and R_A the ridge height increases monotonically as discharge increases. Ridge height decreases for freshwater Froude numbers above 3 and $\alpha = 0.001$ because the water surface elevation at the mouth increases (Figure 3.6a) and I have defined ridge height as the height difference between the offshore peak and the water level at the river mouth. The ROMS output shows that ridge height depends more strongly on shelf slope than aspect ratio (Figure 3.8). Both the ROMS output and equation (3.18) predict ridge height will increase with shelf slope for all freshwater Froude numbers (Figure 3.8a). When the aspect ratio is small ($R_A \leq 103$) and $Fr_f \geq 3$ equations (3.18) significantly overpredicts the ridge height determined from the ROMS output (Figure 3.8). I expect that this is because the size and shape of the plume base that makes contact with the seafloor deviates more from the rectangular planform assumed in the derivation of equation (3.18) when R_A is low and Fr_f is high. As a result, the bottom drag felt by the plume in the bottom-attached region is higher than that predicted by the analytical model, and the ridge height is over predicted. This is further explored by examining the momentum balance in section 3.5.5.

Equation (3.19) is a simplified version of equation (3.18) where $\kappa = 0$. It agrees best with equation (3.18) and the ROMS output for $\alpha = 0.005$ (Figure 3.8). It underestimates h_{ridge} when $\alpha = 0.002$ and predicts negative values when $\alpha = 0.001$. The negative values are not shown on Figure 3.8a. This highlights the importance of plume spreading when $\alpha \leq 0.002$, which will be discussed further in section 3.6.2.

3.5.5 Momentum balance

The mechanism responsible for ridge formation can be understood by examining the momentum balance terms based on the ROMS output. Here I consider a single high discharge run ($Fr_f = 3$, $\alpha = 0.001$ and $R_A = 103$) to illustrate the dynamics (Figure 3.9). The three dominant terms in the depth-averaged x-momentum balance are the advection, bottom stress, and pressure,

$$\bar{u}\frac{\partial \bar{u}}{\partial x} + \frac{\tau_b}{\rho h} + g\frac{\partial \eta}{\partial x} = 0 \tag{3.20}$$

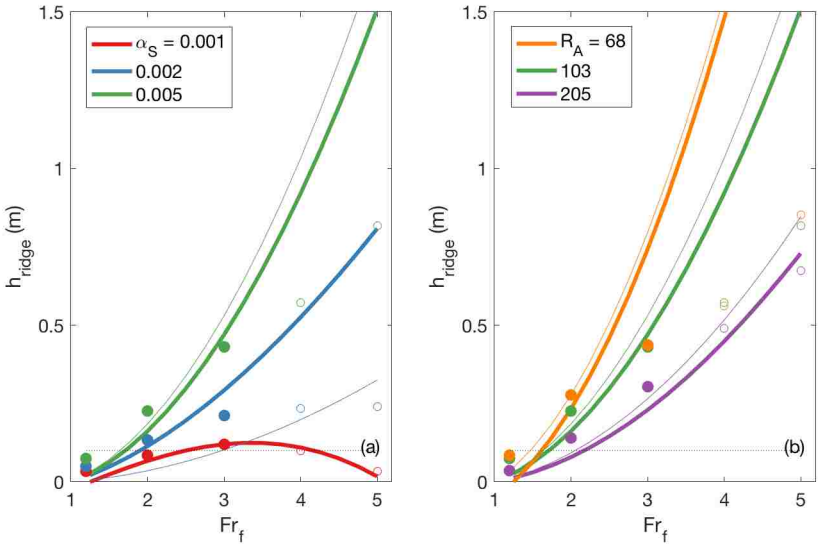

Figure 3.8: Ridge heights for (a) three shelf slopes ($R_A = 103$) and (b) three channel aspect ratios for a shelf slope of 0.005. Filled circles are ROMS estimates for $Fr_f \leq 3$ and open circles are ROMS estimates for $Fr_f \geq 3$. Thick lines were calculated with equation (3.18) and thin lines were calculated with equation (3.19) where $\kappa = 0$. The predicted SWOT vertical accuracy of 0.1 m is shown as a dotted line.

where $\bar{u}$ is the depth averaged cross-shore velocity and τ_b is the bottom stress. The residual of these terms is essentially zero (Figure 3.9c), confirming that the magnitudes of the other momentum terms are negligible. The momentum terms in equation (3.20) are examined to understand the water surface elevation in the river, between the river mouth and the liftoff location, and seaward of the liftoff location. In this high discharge run there is no salt water in the lower reaches of the river and the momentum balance is primarily between the pressure and bottom stress terms. The water surface elevation profile displays the drawdown and M2 behavior predicted by hydraulic models (*Sturm*, 2010); the flow gets shallower and accelerates as it approaches the river mouth, resulting in a positive, increasing advection term (Figure 3.9c). The water surface slope and the corresponding pressure term are negative (Figure 3.9 a and c). The bottom stress is increasing due to the accelerating velocity and its magnitude balances the advection and pressure terms (Figure 3.9c).

At the mouth, the depth increases and the water spreads laterally. As a result, the velocity decreases and the advection term switches sign suddenly, becoming negative (Figure 3.9c). Between the river mouth and the liftoff point the dominant balance is between the advection term, which slowly decreases in magnitude seaward, and the bottom stress term, which is positive and also decreases seaward as the velocity decreases (Figure 3.9c). The pressure term has to balance the advection and stress terms, resulting in a small but positive pressure term and a positive surface slope (Figure 3.9a and c).

At liftoff the bottom stress term drops to zero immediately as the plume loses contact with the bottom (Figure 3.9b-c). The plume layer thins rapidly and accelerates, causing the advection term to switch sign and increase to a local maximum immediately offshore of the liftoff point. These two changes require that the surface slope also changes sign, resulting in a peak in the water surface elevation at the liftoff location (Figure 3.9a-c). Thus, the ridge is due to the decceleration of the flow in the region between the mouth and the liftoff point, which leads to an imbalance between the advection and bottom stress terms. As discharge increases, the advection term increases more than the bottom stress term, which leads to a larger imbalance and therefore a higher ridge (Figure 3.8).

Seaward of the liftoff point the momentum balance is between the pressure term and the advection term, since bottom stress is zero (Figure 3.9c). The rapid acceleration experienced

by the plume at liftoff decreases seaward so the magnitude of the advection term and the compensating pressure term both decrease. Further from the mouth, all three terms decrease to near zero and the water surface elevation decreases to the surrounding water level (Figure 3.9a and c).

It is important to note that the momentum balance presented above is depth averaged, so interfacial stress in the plume offshore of the liftoff point is not evident. I expect that a full three-dimensional momentum balance would indicate a dominant order balance between deceleration of the plume as demonstrated by a decrease in the horizontal advection term and the interfacial mixing and observed by *Kilcher et al.* (2012).

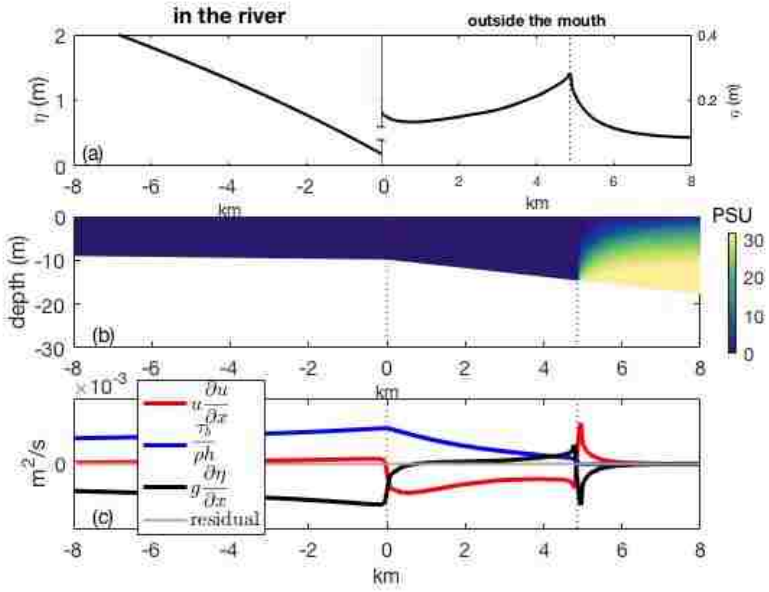

Figure 3.9: Water surface elevation profile, cross-shore salinity cross-section and x-momentum terms for $Fr_f = 3$, $\alpha = 0.001$ and $R_A = 103$. The river mouth is marked with a dotted red line and the liftoff location is marked with a dotted blue line. (a) Water surface elevation. Note that the scales for the surface elevation inside and outside the river mouth are different, and indicated on the left and right y-axes, respectively. (b) Side view of salinity. (c) Three dominant terms of the x-momentum equation and their residual.

3.6 Discussion

Modeled liftoff lengths and ridge heights compare well with analytical solutions (Figure 3.7 and 3.8) presented in this study. Given the importance of the liftoff location on coastal morphology and surface signature, I further investigate the liftoff length dependence on Fr_f (section 3.6.1). In addition, I provide a physical description of the spreading parameter κ, and describe its dependence on the shelf slope (section 3.6.2). The role of barotropic tidal processes in changing the liftoff location and the ridge height is discussed in section 3.6.3. Finally, in section 3.6.4, I compare the magnitudes of the slope and elevation signals predicted by the numerical model with the predicted accuracy of the upcoming satellite altimeter SWOT to determine if SWOT has the potential to detect the liftoff location and use it to estimate discharge.

3.6.1 L_{lo} comparisons

Two example comparisons of the liftoff lengths predicted by equations to ROMS liftoff lengths are shown in Figure 3.10. All of the equations predict L_{lo} will increase with Fr_f but the *Jones et al.* (2007) predictions are much lower than those of the other equations and of the ROMS estimates. This is most likely due to the fact that the *Jones et al.* (2007) equation has no dependence on shelf slope. The *Safaie* (1979) equation underestimates L_{lo} when α and R_A are high (Figure 3.10a) and overestimate L_{lo} when α and R_A are lower (Figure 3.10b). This behavior is consistent with my equation (3.15) that does not include spreading, which indicates the *Safaie* (1979) equation may not capture the physics of spreading correctly for all cases. This may be due to laboratory experimental constraints from which the equation was derived. My equation (3.13), which includes spreading, predicts liftoff lengths that are closest to the ROMS predictions.

3.6.2 Plume spreading and attachment

I observe that plume spreading depends on α, R_A, and Fr_f. Here, two contrasting examples are considered to further investigate the dependence on these parameters, focusing in particular on how spreading is represented by κ. For low freshwater Froude number

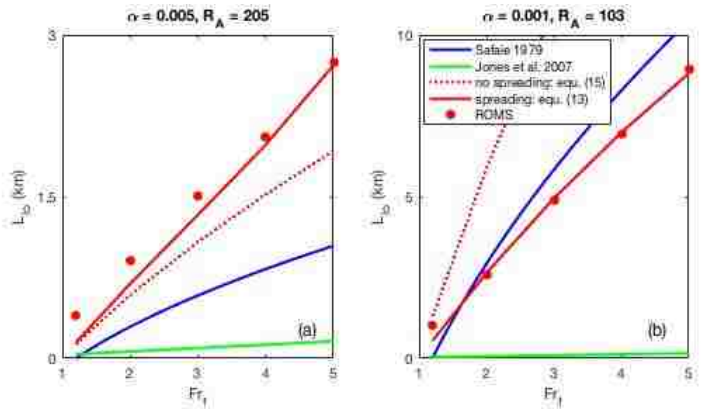

Figure 3.10: Liftoff length comparison of equation predictions to ROMS estimates for (a) $\alpha = 0.005$ and $R_A = 205$ and (b) $\alpha = 0.001$ and $R_A = 103$

($Fr_f = 1.2$) and shelf slope 0.001, the plume starts spreading immediately after exiting the river mouth (Figure 3.11a); however, the attachment to the bottom narrows as the flow gets farther away from the river mouth (Figure 3.11c, e). At higher discharge ($Fr_f = 4$) and a steeper slope (0.005), the plume exiting the river mouth barely spreads before liftoff (Figure 3.11b, f). The analytical expressions derived in section 3.3 quantify this spreading behavior through the spreading parameter κ according to equation (3.9). In section 3.5.3, I used κ as a fitting parameter in my analysis of liftoff length (Figure 3.7). Here, I describe the observed trends in κ and evaluate how it is related to the model simulated spreading.

The liftoff lengths shown in Figure 3.7 were calculated assuming κ does not vary with Fr_f. The κ values used in the L_{lo} estimates were determined by minimizing the difference between the liftoff lengths calculated with equation (3.13) and the ROMS estimates of L_{lo}. The estimated κ values are shown on Figure (3.12a) and suggest that κ increases as the shelf slope decreases for a constant aspect ratio. Furthermore, κ is negative for the steeper shelf slopes. The negative values, which indicate a narrowing plume, are a result of the approximation of the plume shape as a rectangle in equation (3.11); the rectangular plume must narrow to compensate for the rapid deepening as it moves offshore.

In order to test whether the optimized κ values generated by the above fitting procedure correctly represent the physical spreading process, I compare them with an estimate κ

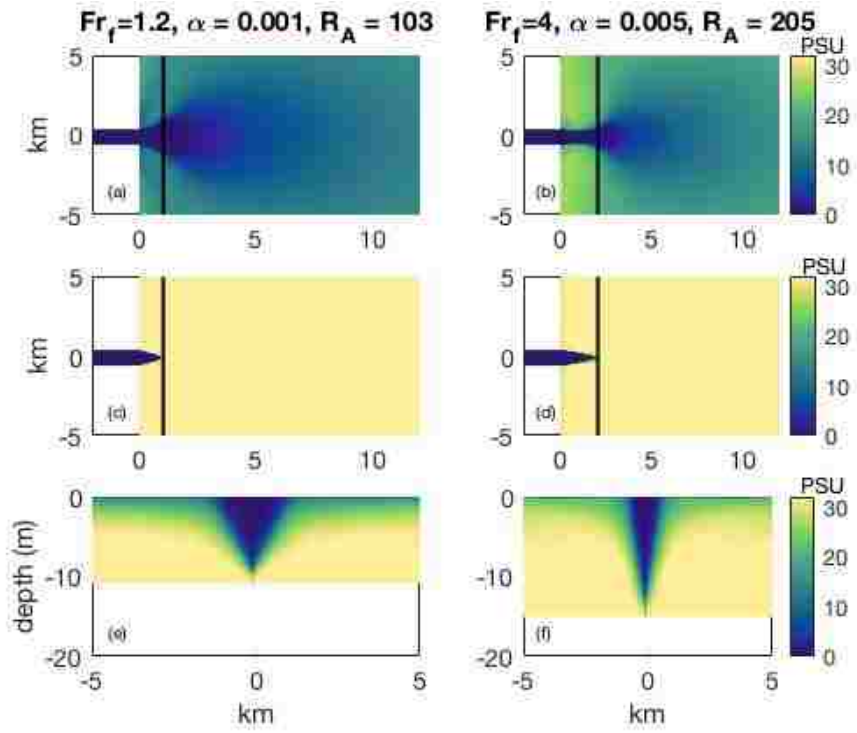

Figure 3.11: Salinity cross-sections for the cases with a large κ ($Fr_f = 1.2, \alpha = 0.001, R_A = 103$) and small κ ($Fr_f = 5, \alpha = 0.005, R_A = 205$): a-b)surface, c-d) bottom, e-f) vertical at the liftoff location. The liftoff location is marked with a black line on the surface and bottom cross-sections.

derived from spreading observed using the model output. The methodology for estimating spreading rates and κ from the model output was described in detail in section 3.4.5. This analysis confirms that κ values derived from the observed spreading increases as the shelf slope decreases but also varies with Fr_f (Figure 3.12a). When the model derived κ values are averaged over Fr_f they agree well with the optimized values for the smaller shelf slopes (Figure 3.12a). However, the average κ values do not agree as well with the optimized values for the steeper shelf slopes due to higher variability with Fr_f. The variability suggests there is a dependence of the spreading rate on Fr_f. The dynamics of this dependence have not been investigated here but the apparent decrease in κ as Fr_f increases for the $\alpha = 0.005$ and $R_A = 205$ case is consistent with observations in near field plume spreading of a change from a convergent plume to a divergent plume (*Yuan and Horner-Devine*, 2013). Despite the differences in the estimated κ values, the liftoff lengths calculated using κ values derived from the freshwater flux agree well with the liftoff lengths extracted from the ROMS output (Figure 3.12b).

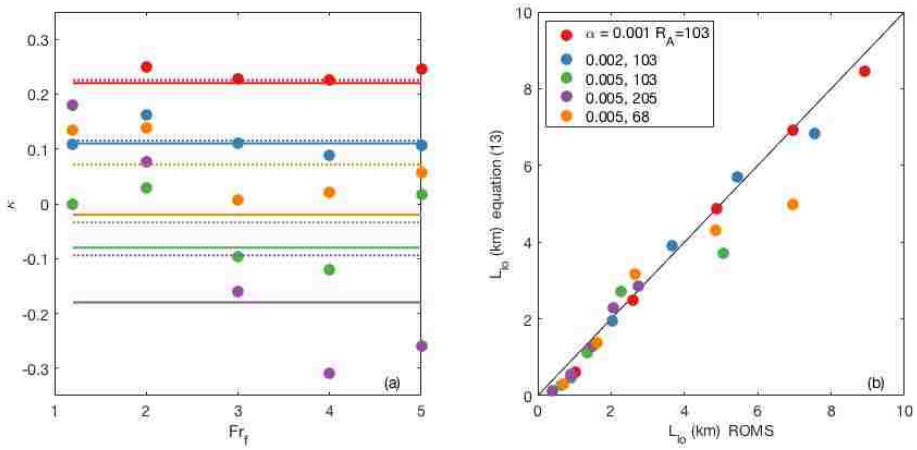

Figure 3.12: Estimations of the spreading parameter and its effect on L_{lo} calculations (a) κ as a function of α, R_A, and Fr_f. Solid lines are the κ values determined by minimizing the difference between the liftoff lengths calculated with (3.13) and the ROMS estimates of L_{lo}. Circles are calculated from the freshwater flux, dashed lines are averages of the circle values over Fr_f. (b) Liftoff lengths calculated with equation (3.13) and κ from the freshwater flux calculation vs. liftoff lengths estimated from the ROMS output.

3.6.3 Tidal influence on the ridge

Model results discussed so far do not take into account the role of barotropic tides, which change the dynamics of many coastal processes associated with riverine discharge (*Liu et al.*, 2009; *MacCready et al.*, 2009; *Suanda et al.*, 2017). To gauge the importance of tides on liftoff dynamics and their surface signature, I conduct an additional simulation with a 1.5 m amplitude M_2 semidiurnal tide ($\alpha = 0.001$, $h_s = 10$ m, and $Fr_f = 2$).

Tidal variability in the location and height of the ridge are shown in Figure 3.13. The ridge peak is closest to the mouth during high tide and farthest from the mouth during low tide (Figure 3.13c). Flood tide with an opposing current to the river flow effectively lowers the net offshore velocity and Fr_f in equations (3.13) and (3.15). The lower Fr_f leads to a shorter L_{lo} and therefore reduces L_{ridge}. Ebb tide has the opposite effect, amplifying the offshore current, effectively raising the Fr_f, and increasing L_{lo} and L_{ridge}. Ridge height is also modulated by tidal propagation; it is at a maximum on flood tide and minimum at high tide (Figure3.13b). The highest ridge heights occur during peak tidal flood velocity when the tidal current opposes the river velocity leading to a significant velocity gradient between the river mouth and the liftoff location. This strong velocity gradient is manifested as a large advective acceleration term in equation (3.16). Since the bottom stress term is decreasing due to spatial flow deceleration, a larger pressure term is needed to balance the advection term. The smallest ridge heights occur during slack high tide when the advection term is closer to balancing the bottom stress term. The maximum ridge height change due to the tide is 0.04 m and the maximum distance that the peak moved over the tidal cycle is 1.7 km. On average, the tide lowers the height of the ridge from 0.085 m to 0.077 m for this run (Figure 3.13b). This could be due to tidally induced mixing, tidal convergence, or the complex interaction between the phase of the tide and the time scale associated with the liftoff process and ridge formation.

These results show that while the tide does affect the ridge height and position it does not eliminate the ridge from the surface. For lower discharge conditions (e.g. $Fr_f \approx 1$) or large tidal amplitudes, the tidal signal may dominate the water surface elevation signal. A more detailed investigation of the influence of tides on the water surface signature of liftoff

is left for future work.

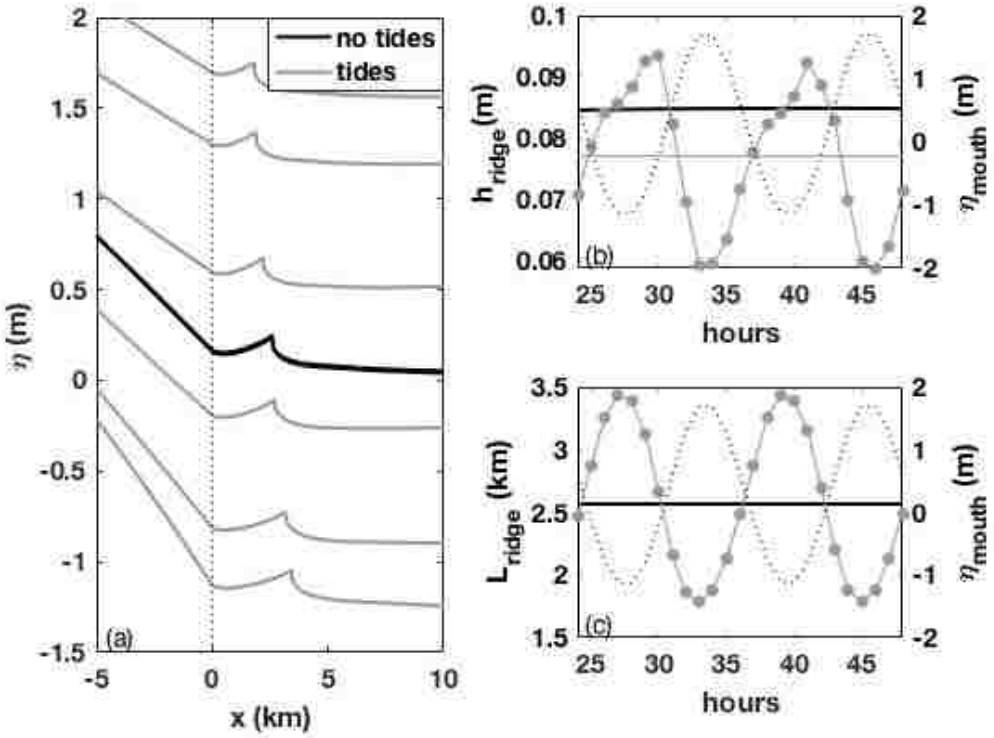

Figure 3.13: Tidal influence on the ridge after running the model for 24 hours. (a) water surface elevation without tides (black) and 6 water surface elevation profiles over 6 hours of the tide (gray) (b) ridge height, h_{ridge}, in gray and water surface elevation at the mouth, η_{mouth}, as a dotted line. The solid black line marks h_{ridge} without the tide and the solid light gray line marks the average h_{ridge} with the tide. (c) distance from the river mouth to the ridge peak, L_{ridge}, in gray and η_{mouth} as a dotted line.

3.6.4 Implications for SWOT measurements of Q at the river mouth

Satellite altimeters such as SWOT detect water surface elevation and water surface slope, which may be used in remote sensing estimates of discharge. Modeled water surface elevation and slope changes can be compared to the predicted accuracy of SWOT measurements to determine if they can be used to estimate discharge.

The predicted water surface elevation accuracy of SWOT measurements is 0.1 m per km^2

(*Rodriguez*, 2016). Thus, a change in the water surface elevation of at least 0.1 m per km^2 is detectable. This accuracy can be compared to water surface elevation changes upstream, at the river mouth, and at the ridge peak to determine if a detectable relationship to discharge exists. In order to distinguish between two discharge values by their water surface elevations their levels must be distinct by at least 0.1 m per km^2. The five low discharge cases all have water surface elevation levels that are distinct from each other by at least 0.1 m at a location 50 kilometers upstream of the mouth (Figure 3.4a). In the estuary, the water surface elevation is higher than the elevation in the ocean by 0.1, 0.15, 0.2, 0.22, and 0.24 m for Fr_f = 0.1, 0.2, 0.3, 0.4, 0.5, respectively (Figure 3.4a). These differences are not large enough for SWOT to be able to distinguish between all of the Fr_f values. At the river mouth, the water surface elevation differences between the five low discharge cases are $\leq$ 0.1 m and therefore not detectable by SWOT. During high discharge conditions, the water surface elevation differences between the five discharge cases are not distinguishable at the river mouth, but are all distinct by more than 0.1 m one kilometer upstream of the mouth (Figure 3.6a), which means SWOT may be able to estimate discharge from the water surface elevation level one kilometer upstream of the mouth during high discharge conditions. Offshore, the ridge heights range from 0.03 to 0.85 m, with the values for $Fr_f < 2$ lower than 0.1 m and therefore not measurable by SWOT (Figure 3.8). The ridge heights of the $Fr_f > 1.2$ steep shelf cases are all distinct by more than 0.1 m and therefore distinguishable by SWOT. When the shelf slope is 0.001, only the $Fr_f = 3$ case has a ridge height above 0.1 m. The cases with a shelf slope of 0.002 have ridge heights above 0.1 m for Fr_f between two and five but the differences between the values are less than 0.1 m. These results suggest that a detectable relationship between ridge height and discharge is strongest for high discharge cases ($Fr_f > 2$) when the shelf is steep ($\alpha \geq 0.005$).

The predicted slope accuracy of the SWOT measurements is 1.7×10^{-5} (*Rodriguez*, 2016). This can be compared to slope changes at the toe of the salt wedge, the river mouth, and the ridge peak. The slope changes at the toe of the salt wedge were on the order of 6×10^{-6} (Figure 3.4c), which is below the predicted SWOT accuracy. This implies that SWOT slope measurements will not be able to distinguish between the five low discharge runs based on the slope changes at the toe of the salt wedge. The observed slope changes

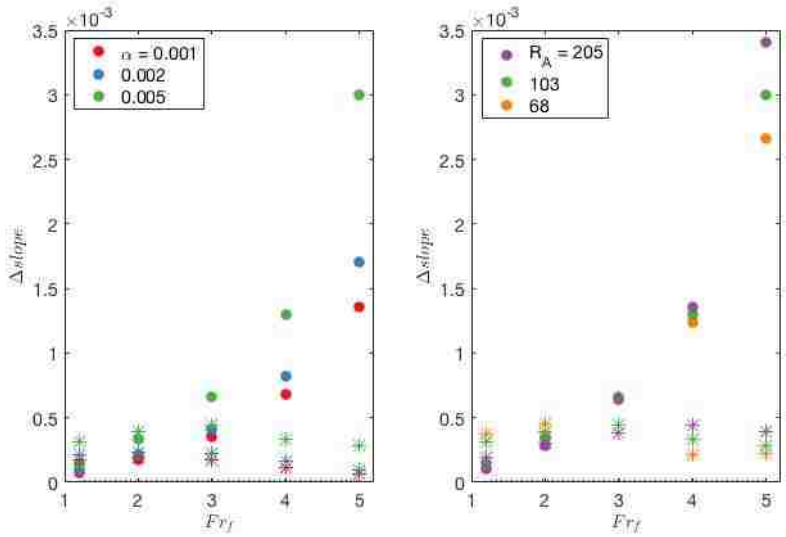

Figure 3.14: Water surface slope changes at the river mouth (filled circles) and at the ridge peak (stars) for (a) three shelf slopes and (b) three river mouth aspect ratios. The predicted SWOT slope accuracy of 1.7×10^{-5} is plotted as a dotted line.

at the mouth during high discharge are on the order of 1.5×10^{-3}, which is larger than the predicted slope accuracy of SWOT (Figure 3.14). The slope changes at the mouth also varied enough between the five high discharge cases for SWOT to be able to distinguish between all five for all of the shelf slopes and shoreline depths studied (Figure 3.14). The slope change at the river mouth also depends on the river bed slope, which makes discharge estimates from that slope change difficult without prior knowledge of river bathymetry. A more robust way to measure discharge remotely from a slope signal would be to locate where liftoff occurs due to the slope changing from positive to negative at the ridge peak. The slope change at the ridge peak is smaller than the slope change at the river mouth (Figure 3.14), but still larger than the SWOT predicted accuracy. It does not increase with discharge, which means it can be used most effectively as a method of determining the liftoff location instead of as a method of directly estimating discharge. Once the liftoff location is determined, then equations (3.13) or (3.15) may be used to calculate discharge.

The results presented here cover a range of shelf slopes, aspect ratios, and freshwater Froude numbers, which may have water surface signals observable by SWOT. Although

rivers such as the Amazon can have aspect ratios greater than 100 and floods with $Fr_f > 5$, smaller rivers typically have values of R_A on the order of 10-100 and Fr_f on the order of 1-3. In Figure 3.15 I investigate the range of liftoff lengths and ridge heights that are predicted by equations (3.13) and (3.18), in terms of Fr_f, α, and R_A. For a fixed aspect ratio of 103, the liftoff length is highest when the shelf slope is shallow and Fr_f is high (Figure 3.15a). For comparison, predictions for the Connecticut, Columbia, and Mississippi rivers are shown that correspond to typical values of R_A and Fr_f during flood conditions. The derived equations predict liftoff lengths of 500 m, 1500 m, and 10,000 m and ridge heights of 0.07 m, 0.08 m, and 1.05 m for the Connecticut, Columbia, and Mississippi rivers respectively (Figure 3.15b and d). These predictions suggest that the ridge heights for the Connecticut and Columbia rivers may be just below the threshold of detection by SWOT, but the Mississippi river may be above it. Therefore, the ridge may be detectable in the water surface elevation signal of the Mississippi river but only detectable in the water surface slope signals of the Connecticut and Columbia rivers.

3.7 Conclusions

In this study I use a three-dimensional numerical model to investigate the dependence of the river plume liftoff process on river discharge, shelf slope and the river mouth aspect ratio. The modeled liftoff location and the water-surface elevation at the liftoff location agree well with analytical expressions derived assuming that the upper-layer Froude number is unity, and the primary order steady-state cross-shelf momentum balance is between advective acceleration, barotropic pressure gradient and the bottom stress.

I identified water surface elevation signals related to the liftoff process that could be useful for remote sensing of river discharge during high ($Fr_f > 1$) and low ($Fr_f < 1$) discharge conditions. During high discharge conditions a ridge forms at the liftoff point on the water surface. The surface slope and ridge height vary with discharge, and are large enough to be detected in most cases by the upcoming satellite altimeter SWOT. Derived expressions that predict the ridge location and height in terms of discharge, shelf slope, river mouth aspect ratio, and plume spreading compare well the results obtained with the numerical model. Plume spreading is found to be negligible between the river mouth and

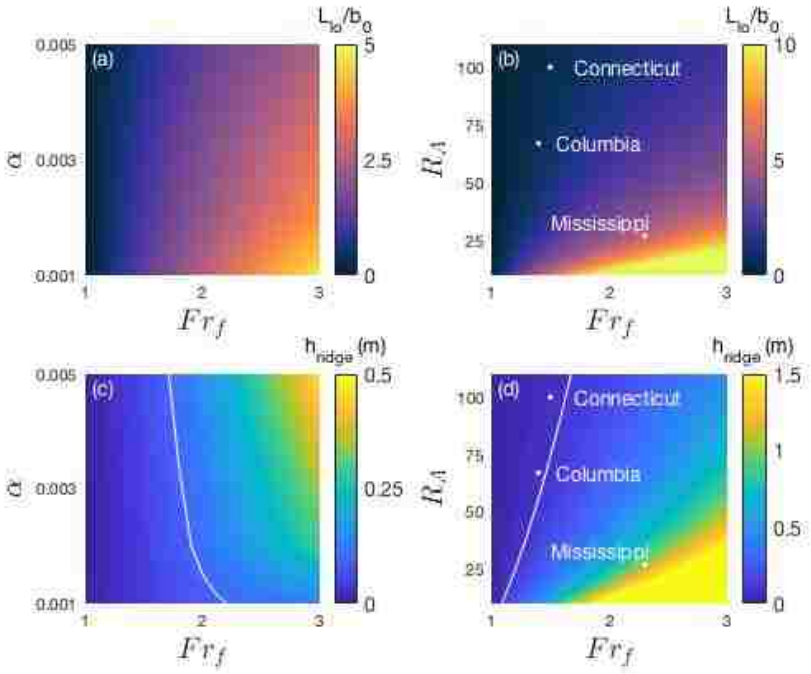

Figure 3.15: Normalized liftoff lengths and ridge heights for typical aspect ratios and shelf slopes. (a) Normalized liftoff lengths for an aspect ratio of 103 and a range of shelf slopes (b) Normalized liftoff lengths for a shelf slope of 0.005 and a range of aspect ratios (c) Ridge heights for an aspect ratio of 103 and a range of shelf slopes with the predicted SWOT accuracy of 0.1 m marked as a white line (d) Ridge heights for a shelf slope of 0.005 and a range of aspect ratios with the predicted SWOT accuracy of 0.1 m marked as a white line. Possible ridge heights for peak floods of three rivers with different aspect ratios assuming the shelf slope for all of them is 0.005.

liftoff for shelf slopes steeper than 0.005, further simplifying the relationship between liftoff location and discharge. The liftoff ridge is still present with the addition of moderate amplitude tides, but the ridge location and height are modulated.

During low discharge conditions water surface slope and elevation changes can also be related to discharge, however their magnitudes are smaller than will likely be detectable by SWOT. This study does not account for changes in water surface elevation due to waves, upwelling, and downwelling, which are expected to further influence the structure of the water surface elevation field near the river mouth. Investigation of these processes is left for future work. Finally, results from this study indicate that low and high discharge conditions can be distinguished by the presence or absence of the ridge and SWOT measurements of the location or height of the ridge can be used to estimate discharge.

Chapter 4

REMOTE SENSING OF RIVER BOTTOM ROUGHNESS

4.1 Introduction

Numerical and analytical models of flow in rivers, floodplains, and tidal estuaries require estimates of bed roughness (*Godin*, 1999; *Wang et al.*, 2011; *Helaire et al.*, 2019). In a tidally influenced river channel the amplitude and phase of the tidal propagation depend on the effective drag (*Ralston et al.*, 2019). River discharge algorithms are being developed to estimate discharge from satellite altimetry such as data from the upcoming Surface Water and Ocean Topography (SWOT) mission, yet all of these algorithms require a friction factor such as Manning's coefficient to characterize the roughness (*Bonnema et al.*, 2016). Extensive research has been done to estimate values of Manning's coefficient for different river bed materials (*Arcement and Schneider*, 1989), but the drag coefficient depends not only on the characteristic particle size of the bed material but also on how the particles are grouped to form dunes and ripples (*Nikora et al.*, 1998).

The drag coefficient, C_d, is defined as the the squared friction velocity, u_*^2, normalized by a reference velocity squared

$$C_d = \frac{u_*^2}{u^2}, \tag{4.1}$$

where the reference velocity is often measured one meter above the bed (*Sanford and Lien*, 1999). It has previously been measured using moored acoustic Doppler current profilers (ADCPs) (*Fong et al.*, 2009; *Xu et al.*, 2017), which are expensive and difficult to deploy. A remote sensing technique to measure C_d would be an improvement in ease of deployment over ADCP measurements and could provide more information about the spatial variability of C_d than a point measurement from an *in situ* instrument.

Remotely sensed surface turbulence data could be used to measure C_d if the connection between the bottom generated turbulence and the surface is understood. *Nezu and Nakagawa* (1993b) published equations for vertical profiles of the three fluctuating components

of the velocity: u', v', and w'. The exponential form of the equations was derived but the constant coefficients were found using laboratory measurements. The equations show the velocity fluctuation profiles depend on u_* and decrease exponentially above the bed as

$$u'_{rms} = \sqrt{\overline{u'^2}} = u_* 2.3 exp(\frac{-z}{H}) \tag{4.2}$$

$$v'_{rms} = \sqrt{\overline{v'^2}} = u_* 1.63 exp(\frac{-z}{H}) \tag{4.3}$$

$$w'_{rms} = \sqrt{\overline{w'^2}} = u_* 1.27 exp(\frac{-z}{H}) \tag{4.4}$$

where z is the distance above the bottom and H is the water depth. These equations were tested over a range of flow regimes in laboratory experiments by *Auel et al.* (2013). They found the equations correctly described the vertical profiles of u'_{rms}, v'_{rms}, and w'_{rms} in a wide channel regardless of the Froude or Reynolds numbers of the flow. This suggests these equations could be used to estimate u_*, and therefore C_d, from surface measurements of u'_{rms}, v'_{rms}, and w'_{rms}, in wide channels over a range of conditions.

4.1.1 C_d from $\overline{u'w'}$

Drag coefficients have been calculated before using *in situ* measurements of the $\overline{u'w'}$ stress (*Fong et al.*, 2009; *Xu et al.*, 2017).

The $\overline{u'w'}$ stress has been observed in the field to be highest near the bed and decrease vertically (*Talke et al.*, 2013). It was measured in the laboratory for depth ranges from $z/H = 0.2$ to $z/H = 0.85$ and found to be higher throughout those depths for rough channels than smooth channels (*Balachandar and Bhuiyan*, 2007). In order to study $\overline{u'w'}$ throughout the water column, a normalized Reynolds stress can be written as

$$\tau_{uw} = -\frac{\overline{u'_z w'_z}}{u_z^2} \tag{4.5}$$

where u, u', and w' are all measured at the same depth, z. The $\overline{u'w'}$ drag coefficient calculations were based on the *Nezu and Nakagawa* (1993b) equation that predicts $\overline{u'w'}$ normalized by the squared friction velocity is only a function of z/H. This equation was derived from the Navier-Stokes equations for high Reynolds number flows where viscosity is negligible

and no secondary currents are present (*Nezu and Nakagawa*, 1993b).

$$-\frac{\overline{u'w'}}{u_*^2} = \left(1 - \frac{z}{H}\right) \tag{4.6}$$

The friction velocity can be calculated using equation (4.6) with ADCP Reynolds stress and depth measurements (*Stacey et al.*, 1999). Combining equations (4.1) and (4.6) gives an equation for the drag coefficient in terms of the Reynolds stress

$$C_d = -\frac{\overline{u'w'}}{(1 - z/H)u^2}. \tag{4.7}$$

Fong et al. (2009) used ADCP velocity data measured one meter above the bed, approximated $z/H = 0$, and calculated C_d as the slope of fits to

$$C_d = -\frac{\overline{u'w'}}{u^2}. \tag{4.8}$$

4.1.2 C_d from $\overline{u'v'}$

Calculations of C_d from $\overline{u'w'}$ are not possible from remotely sensed surface data because w and w' cannot be detected using PIV. Near the surface, a blockage layer develops due to the kinematic boundary condition where the vertical velocity fluctuations decrease and their energy is redistributed into the horizontal velocity fluctuations (*Shen et al.*, 1999). In order to use v'_{rms} instead of w'_{rms} at the surface I need a method of estimating the relationship between $\overline{u'w'}$ and $\overline{u'v'}$. If I make the assumption that they scale according to $\overline{u'w'} = u'_{rms}w'_{rms}$ and $\overline{u'v'} = u'_{rms}v'_{rms}$, then I can combine equations (4.2), (4.3), and (4.4) to write $\overline{u'w'}$ in terms of $\overline{u'v'}$ as

$$\overline{u'w'} = \overline{u'v'}\frac{1.27}{1.63} = 0.78\overline{u'v'}. \tag{4.9}$$

While there is no physical reason why $\overline{u'w'}$ should be correlated with $u'_{rms}w'_{rms}$ and $\overline{u'v'}$ should be correlated with $u'_{rms}v'_{rms}$, these assumptions are tested in section (4.3.4) where our C_d analysis assumes that they are correlated.

A normalized Reynolds stress throughout the water column can be written as

$$\tau_{uv} = \frac{0.78|\overline{u'_z v'_z}|}{u_z^2}. \tag{4.10}$$

where u, u', v' are all measured at depth z, and the absolute value has removed the directionality of the stress. The directionality of the stress is removed because it does not have a relationship to bottom roughness in the same way that $\overline{u'w'}$ does via the friction velocity term in the equation (4.6) for a logarithmic velocity profile. There may be a horizontal velocity gradient of the river flow but it is due to shear stress from the sides of the river or from secondary flows that generate lateral shear (*Yang et al.*, 2013) rather than from bottom roughness.

In order to calculate C_d using measurements of $\overline{u'v'}$, equation (4.7) needs to be written in terms of $\overline{u'v'}$

$$C_d = \frac{0.78|\overline{u'v'}|}{(1 - z/H)u^2}. \tag{4.11}$$

Using the same approximation as *Fong et al.* (2009) that $z/H = 0$ for data one meter above the bed gives an equation for C_d in terms of $\overline{u'v'}$ as

$$C_d = \frac{0.78|\overline{u'v'}|}{u^2_{1mab}}. \tag{4.12}$$

Near the surface an approximation of $z/H = 0.95$ and a surface reference velocity can be used to give

$$C_d = \frac{15.6|\overline{u'v'}|}{u^2_{surface}}. \tag{4.13}$$

This equation for C_d assumes $\overline{u'v'}$ is correlated with $u'_{rms}v'_{rms}$, which may not be true unless the turbulent fluctuations are due to boils expanding symmetrically. A C_d equation that does not depend on this assumption would be more applicable where the turbulence is not in the form of symmetrical boils.

4.1.3 C_d from TKE

Another turbulence statistic that may be useful in calculating C_d is the turbulent kinetic energy, which is defined as

$$TKE = 1/2(\overline{u'^2} + \overline{v'^2} + \overline{w'^2}) \tag{4.14}$$

(*Kundu et al.*, 2015). It can be written in terms of the friction velocity by combining equations (4.2), (4.3), and (4.4) to obtain

$$TKE = 4.78u^2_* exp(-2\frac{z}{H}). \tag{4.15}$$

At the river bed $z/H = 0$ and equation (4.15) simplifies to

$$TKE_{bed} = 4.78u_*^2. \tag{4.16}$$

At the water surface $z/H = 1$ and equation (4.15) simplifies to

$$TKE_{surface} = 0.65u_*^2. \tag{4.17}$$

This scaling implies that TKE is approximately one order of magnitude smaller on the water surface than near the bed. Solving these equations for the friction velocity gives

$$u_*^2 = \frac{TKE_{bed}}{4.78} = \frac{TKE_{surface}}{0.65} \tag{4.18}$$

Substituting this value of u_* into equation (4.1) gives equations for the drag coefficient estimated from TKE measurements at the river bed and the surface.

$$C_d = \frac{u_*^2}{u^2} = \frac{TKE_{bed}}{4.78u^2} = \frac{TKE_{surface}}{0.65u^2} \tag{4.19}$$

4.1.4 Parameterization of bed roughness

The two main factors to be considered when determining the bottom roughness of a channel are the materials that compose the bed and the shape of the bedforms (*Arcement and Schneider*, 1989; *Cowan*, 1956). *Jellesma* (2013) parameterized the total Nikuradse roughness, k_N, as the sum of the grain size, D_{90}, and the Nikuradse roughness of the primary and secondary dunes

$$k_N = k'_N + k''_{N,p} + k''_{N,s} \tag{4.20}$$

where $k'_N = D_{90}[m]$ and the primary and secondary dune roughness values are given by

$$k''_{N,p} = 1.1\delta_p(1 - e^{-25\delta_p/\lambda_p}) \tag{4.21}$$

$$k''_{N,s} = 1.1\delta_s(1 - e^{-25\delta_s/\lambda_s}) \tag{4.22}$$

where the subscript p stands for primary and the subscript s stands for secondary. The dune height, δ, and length, λ, have units of meters. This parameterization takes into account both the size characteristics of the bed material and the shape of the bedforms. It also accounts for the fact that the bedforms often take the shape of smaller dunes on top of larger dunes.

4.1.5 Remote sensing of turbulence

Calibrated infrared (IR) imagery measures the temperature of the thermal boundary layer at the water surface. The thermal boundary, or skin layer is $O(1$ mm) thick and cooler than deeper water when there is a net heat flux from the water to the air (*Saunders*, 1967). This cool skin layer can be disrupted by waves (*Jessup et al.*, 1997) or coherent structures such as boils (*Chickadel et al.*, 2009) and the disruptions can be detected in IR imagery. Infrared movies of the surface can be analyzed using particle imaging velocimetry (PIV) techniques to extract the surface velocity. *Chickadel et al.* (2011) showed surface velocities and turbulence statistics extracted from PIV analysis of IR imagery agreed well with *in situ* measurements near the surface.

Visual imagery of the surface can be used to measure surface velocities in the laboratory when the water is seeded with particles. *Johnson and Cowen* (2017) used PIV in the laboratory to measure surface velocities, calculate dissipation, and calculate u_* using a relationship derived by *Nezu* (1977).

$$\frac{\langle\epsilon\rangle H}{u_*^2} = \frac{E}{\sqrt{z/H}} exp(-3z/H) \tag{4.23}$$

where $\langle\epsilon\rangle$ is the ensemble average of the dissipation and E is an empirically derived constant that depends on the bottom roughness. *Johnson and Cowen* (2017) used $E = 4.76$ for a smooth bed, $E = 12$ for a rough bed, their remotely sensed velocity data to calculate $\langle\epsilon\rangle$, and then calculated u_*^2 using equation (4.23).

4.2 Methods

4.2.1 Coherent Structures Experiment: COHSTREX09

Surface and water column velocity and turbulence measurements were made at 10 sites on a tidal section of the Snohomish River during a two week experiment. The five flood tide sites and five ebb tide sites are shown on Figure 4.1a. The study sites were approximately 15 km upstream of the river mouth and salinity intrusions were observed at the beginning of ebb tides and the end of flood tides. Instruments were mounted on a 65-ft research barge that had two retractable pilings holding it stationary in the river flow but allowing for vertical

movement as the tide changed the water level.

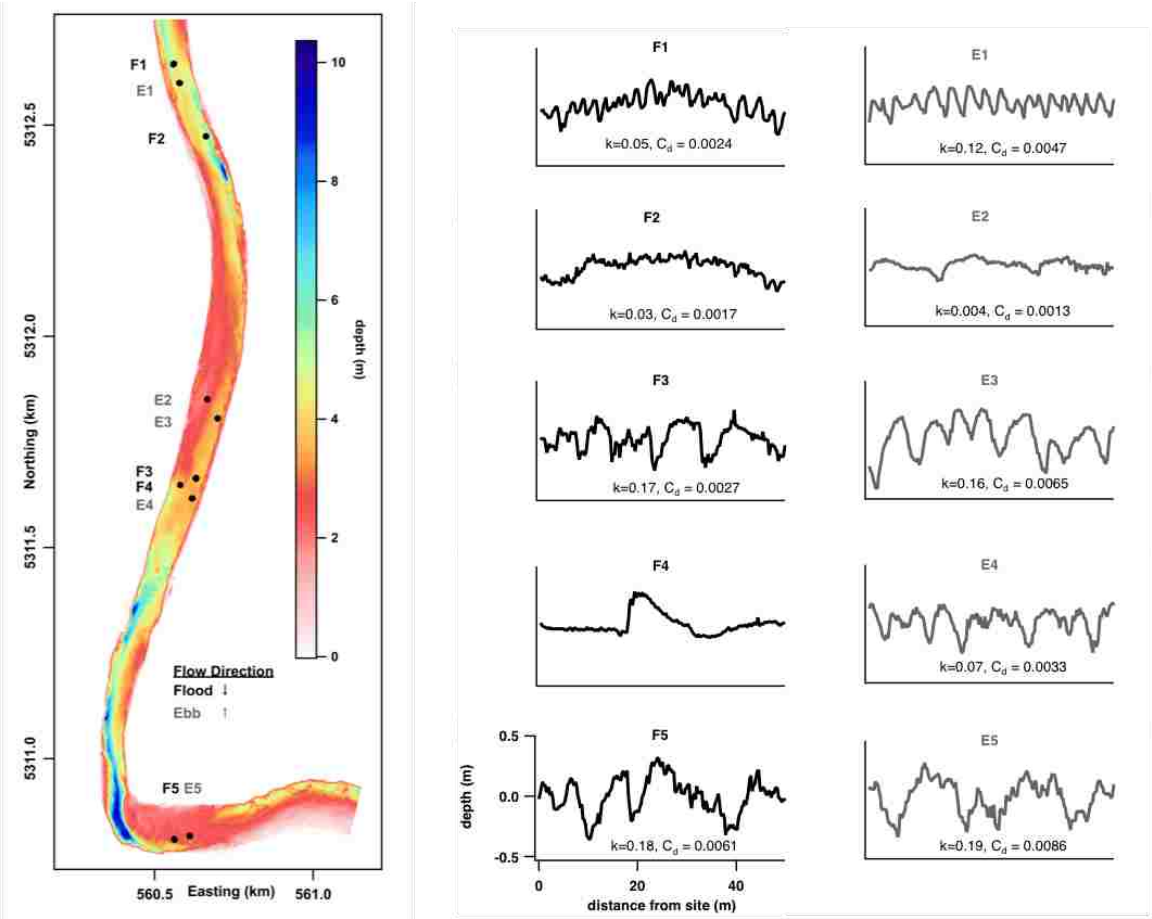

Figure 4.1: Snohomish River bathymetry a) Experiment sites consisting of 5 ebb tide sites (E1-E5) and 5 flood tide sites (F1-F5) b) 50 meter transects of the bathymetry upstream of the sites. Flow direction on a) is from top to bottom during flood tide and bottom to top during ebb tide. Flow direction on b) is from right to left.

4.2.2 Measurement of bed roughness

The bathymetric features were measured before and after the experiment by a boat mounted multibeam sonar. The features consisted of combinations of ripples and semi-periodic dunes that varied between sites but not temporally over the duration of the experiment. The average water depths of the sites varied from 2.48 m to 4.88 m.

The total Nikuradse roughness was calculated using equation (4.20) at 9 of the 10 sites. Site F4 (Figure 4.1) was excluded from the analysis because the bathymetry transect did not have repeating sinusoidal bedforms. Sediment samples were not collected during the experiment but nearby historical surveys showed a grain size of 1 mm (*DeVries*, 2015), which gives a k'_N of 0.001 m. The Nikuradse roughness values due to the primary and secondary dunes were calculated using equations (4.21) and (4.22). The primary and secondary dune heights and lengths were calculated from spectra of bathymetry transects upstream of each site. The dune length was calculated as

$$\lambda = 1/f_{peak} \tag{4.24}$$

where f_{peak} is the frequency of the peak in the spectrum. The dune height was calculated as

$$\delta = \frac{2\sqrt{h_p \Delta f}}{0.6} \tag{4.25}$$

where h_p is the height of the peak in the spectrum and Δf is the frequency bin width of the spectrum.

4.2.3 Velocity measurements

Surface velocity measurements were made using PIV techniques applied to IR imagery and *in situ* velocity measurements were made by an ADCP. ADCP velocity measurements were used to calculate C_d from data one meter above the bed for the entire tidal period. Surface velocity measurements were only used when the flow was almost steady and the depth averaged acceleration as measured by the ADCP was less than 0.1 m/s^2.

4.2.4 Stratification

Tidal intrusion of the salt wedge causes stratification that significantly reduces surface turbulence (*Beuzen et al.*, 2016). Stratification decouples the surface water from the bottom where bed roughness causes the turbulence. Salinity was measured throughout the experiment to enable us to control for this effect. Conductivity-Temperature-Depth instruments (CTDs) were deployed on the river bed and surface to continuously measure salinity stratification and CTD casts were performed every half hour. The remotely sensed surface data

used in the C_d calculations was acquired when the salinity difference between the surface and bed measurements was less than 0.5 PSU. ADCP data were not eliminated during times of stratification because the velocity measurements used in the C_d calculations were taken one meter above the bed and I did not observe significant salinity stratification in the bottom meter of water.

IR PIV

Infrared imagery of the surface was collected at 20 Hz and analyzed using PIV techniques to produce velocity maps. The velocity maps were then subsampled to an area of the image where the velocities were not influenced by the subsurface frame. Spectra were calculated of three minute sections of the data and fit to $f^{-5/3}$ between 0.1 and 2 Hz. Figure 4.2 shows example spectra for times when there was low energy, wave contamination, and good velocity data. Only data with a fit R^2 above 0.9 were used in the C_d calculations. A good spectral fit to $f^{-5/3}$ indicated the turbulence was consistent with a turbulent cascade of energy from large to small scales (*Kundu et al.*, 2015), whereas a fit with a low R^2 value indicated either it was early in the tide and the turbulent field was not fully developed, there was noise in the IR imagery, or surface waves were causing a peak in the spectrum.

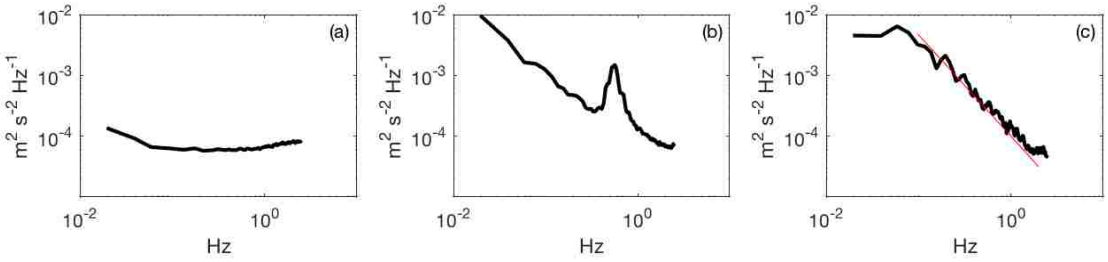

Figure 4.2: Example PIV velocity spectra a) low energy b) wave contamination c) good spectra with $f^{-5/3}$ shown in red.

ADCP

A downward facing 1200 kHz ADCP (RDI) was mounted on an A-frame that was immediately downstream of the IR imager field of view (*Talke et al.*, 2013). It measured velocity

at 1 Hz in 0.25 m depth bins from the river bottom up to 1.5 m below the surface. The Reynolds stresses and three components of velocity were extracted from the four beams using the methods outlined in *Stacey et al.* (1999).

4.3 Results

4.3.1 Parameterization of bed roughness

The ten study sites show a range of bed roughness characteristics (Figure 4.1). Several sites have periodic patterns of dunes, while F2, E2, and F4 have small scale roughness and less periodic large scale features. The roughness characteristics of sites E2 and E3 are very different even though the two sites are less than 100 m apart.

An example of the bed roughness parameterization method is shown for site F3 in Figure 4.3. The bathymetry transect upstream of the site shows two scales of roughness. Small scale roughness is superimposed on larger dunes. A power spectrum of 50 m of the bathymetry transect (Figure 4.3b) has a prominent primary peak corresponding to the larger dunes and a smaller secondary peak corresponding to the small scale roughness. The secondary peak was chosen by visually inspecting each spectrum. Dune heights and lengths were calculated following the methods outlined in section (4.2.2). The primary dune height of site F3 is 0.24 m and the secondary dune height is much smaller at 0.05 m. The primary dune length is 8 m and the secondary dune length is 1.33 m. The dune heights of all of the study sites ranged from 0.01 - 0.36 m and the dune lengths ranged from 0.66 - 16 m. The k values of the sites were calculated using equation (4.20) for 50 m, 100 m, and 150 m upstream bathymetry transects. The k values calculated with the 50 m transects were most strongly correlated with C_d values discussed in Section 4.1.1. The minimum k value calculated was 0.005 and the maximum was 0.19.

The roughness parameterization can also be calculated ignoring the smaller scales of roughness using equation (4.20) without the $k''_{N,S}$ term. This reduces the k as shown in Figure 4.4a. The offset can be approximated with the average difference of 0.017 m so that the full parameterization can be estimated using $k''_{N,S} = 0.017$ in equation (4.20) instead of manually finding the secondary peak in every spectra. This simplified calculation of k can

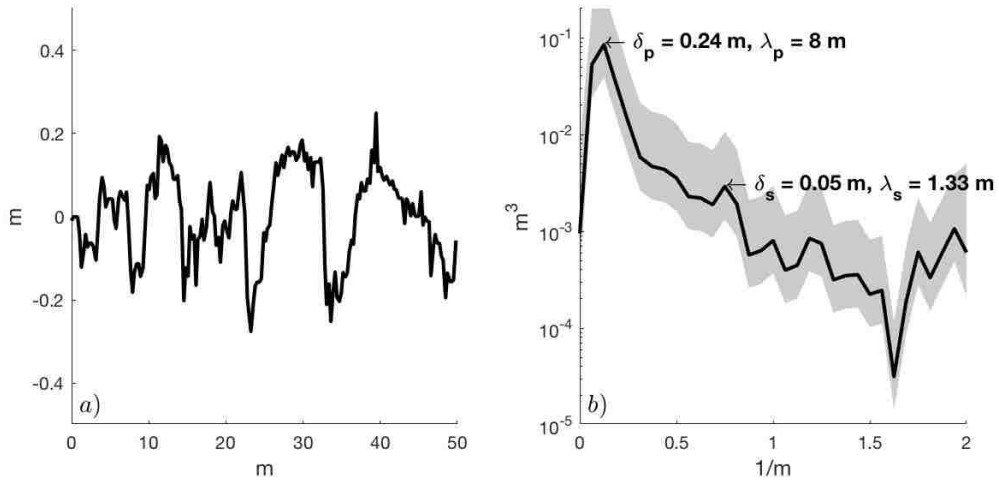

Figure 4.3: a) Sample bathymetry transect upstream of site F3 b) Power spectrum of the bathymetry transect showing the primary and secondary dune heights, δ, and lengths, λ. The shading shows the 95% confidence interval of the spectrum.

be applied to multiple bathymetry transects to estimate the sensitivity of k to the nearby bathymetry.

Nine bathymetry transects were extracted at each site to derive an estimate of the error in the k values. Four were to the left of the original transect and four were to the right. The transects spanned a nine degree angle as shown in Figure 4.5. The average k values are shown in Figure 4.4b versus the original k values. The sites with the largest error bars are the two sites with the highest k values, which are the two sites located closest to the bend in the river (F5 and E5 on Figure 4.1). The nine bathymetry transects for E5 shown in Figure 4.5 highlight how some transects overlay a deep hole near the curve while other transects do not. Sites where the bathymetry is non-uniform in the cross-stream direction have k values that are sensitive to the angle of the bathymetry transect used in the calculation.

4.3.2 C_d from $\overline{u'w'}$ Stress

Drag coefficients were calculated using ADCP measurements of the $\overline{u'w'}$ stress 1 meter above bottom (mab) following the methods of *Fong et al.* (2009) (equation 4.8). A linear fit to the

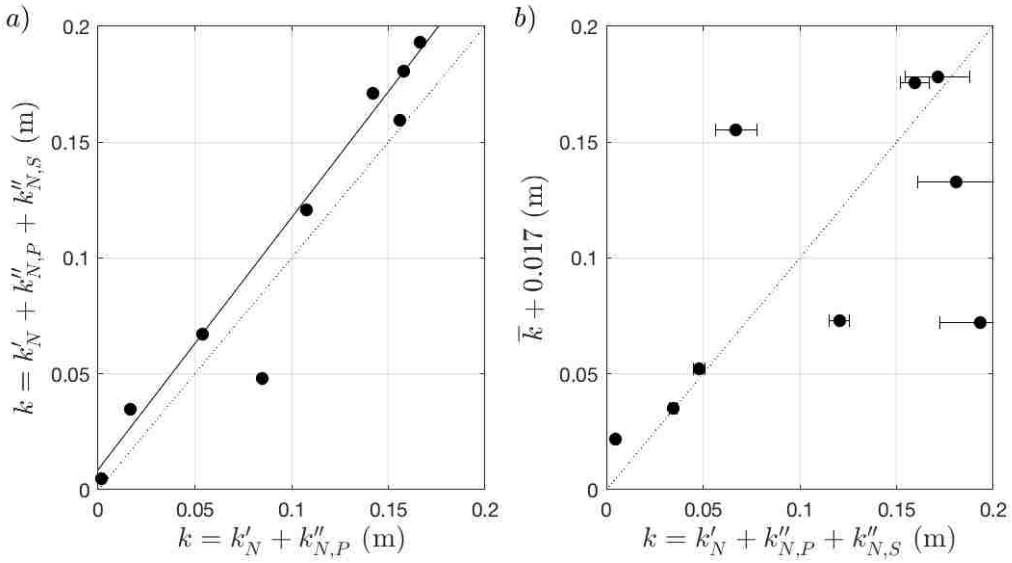

Figure 4.4: a) k calculated using both the primary and secondary versus k calculated with only the primary peak. The dashed line is the one to one line for reference and the solid line is a robust fit to the data. b) k calculated using both the primary and secondary versus an average k from 9 bathymetry transects at the same site using only the primary peak and adding the 0.017 m offset to account for the secondary peak. Error bars are the standard error of the k values from the 9 transects.

ADCP measurements of $\overline{u'w'}$ versus the reference velocity 1 mab has an R^2 of 0.72 for the example tide shown in Figure 4.6a for site E5. The slope of a fit through the origin gives a C_d of 0.0073. The maximum velocity during this tide was 0.63 m/s and the average velocity was 0.31 m/s. This analysis is repeated for all twenty tides yielding C_d values that show a strong trend of increasing with the k values calculated in Section 4.3.1 (Figure 4.6b). When the individual tidal C_d values are averaged at each site the minimum C_d value is 0.0013 and the maximum is 0.0086. A robust linear fit to the average C_d values versus k has an R^2 of 0.93 (Figure 4.6b). The robust linear fit method gives a fit that is less sensitive to outliers. The algorithm uses iteratively reweighted least squares with a bisquare weighting function (*Huber*, 2004). Another method of calculating C_d at each site is to combine the $\overline{u'w'}$ and u data from all tides at that site and then use equation 4.8. This analysis yields a very strong correlation between C_d and k (Figure 4.7a) with an R^2 value of 0.95. The

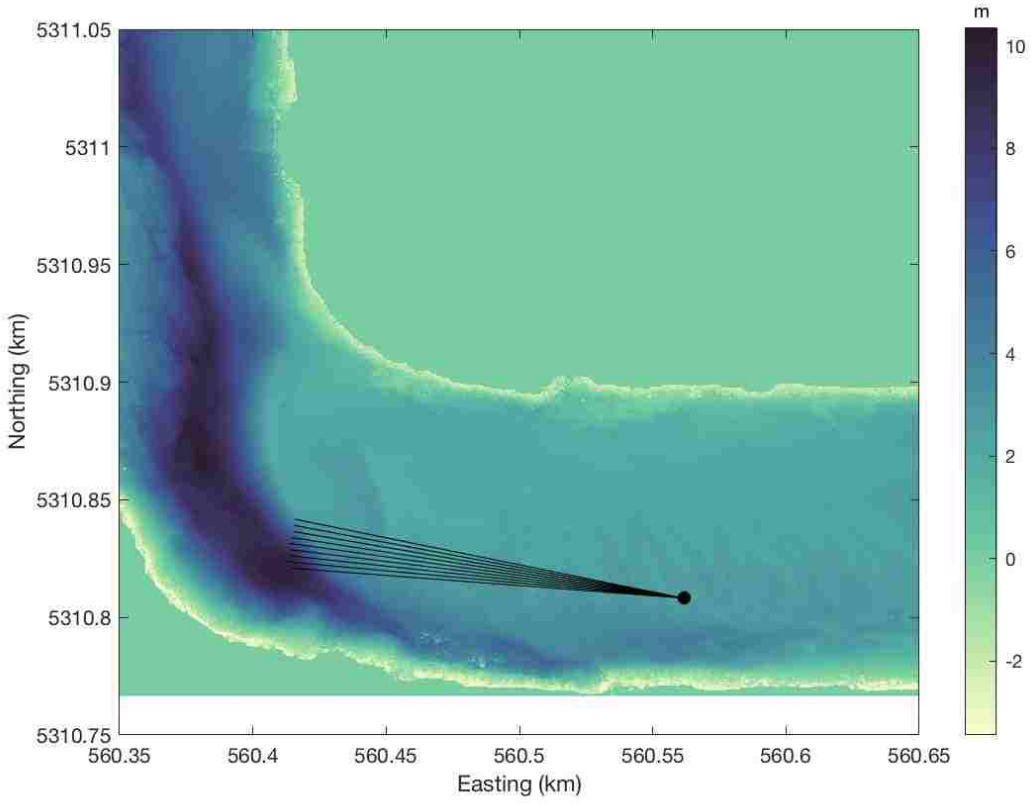

Figure 4.5: Nine bathymetry transects extracted from site E5 showing a span of nine degrees.

strong correlation between C_d and k implies the k parameterization is correctly describing the bottom roughness that is causing a drag force on the moving fluid.

The vertical structure of $\overline{u'w'}$ in the water column is explored in Figure 4.7b where the normalized Reynolds stress, τ_{uw}, is shown for eight depth bins at four sites with different k values. The values closest to the river bed show τ_{uw} increases with k. This correlation continues up through the water column until the top point where the sites with $k = 0.03$ and $k = 0.12$ have indistinguishable τ_{uw} values. The site with $k = 0.03$ had many boat wakes, which may have corrupted the τ_{uw} measurements leading to an erroneously high value. The strong correlation of τ_{uw} with k throughout the water column suggests Reynolds stress at the surface can be used to estimate C_d. The $\overline{u'w'}$ component of the Reynolds stress can't be

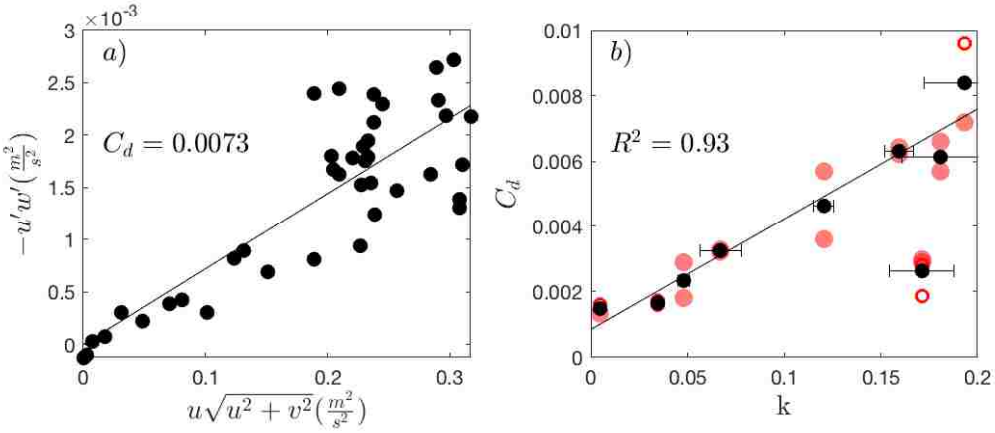

Figure 4.6: ADCP data one meter above the bed: calculation of C_d using $\overline{u'w'}$ in equation (4.8). (a) Example calculation of C_d for one tide at site E5. C_d is the slope of $\overline{u'w'}$ vs. $u(u^2 + v^2)^{1/2}$ (b) C_d calculated for twenty tides at the nine sites. Red circles are the measurements at each tide and black circles are the average C_d for each site. Solid red circles are tides where the R^2 of the fit was > 0.5 and open red circles are the tides where the R^2 of the fit was < 0.5. Error bars are the standard error of the 9 k values calculated at each site in Section 4.3.1. The black line is a robust fit to the site averages.

used to estimate C_d using surface measurements because remote sensing does not measure w'. A turbulence statistic is needed that is not dependent on w in order to measure C_d remotely at the surface.

4.3.3 C_d from surface TKE

Turbulent kinetic energy depends on all three components of velocity but it does not go to zero at the surface even though w goes to zero. As the surface is approached, energy is transferred from the vertical components of velocity to the horizontal components of velocity (*Shen et al.*, 1999). In order to relate the surface TKE to the bottom roughness I first show that TKE near the bed is related to the bottom roughness and that this relationship propagates up through the water column. Drag coefficients calculated with TKE data measured 1 mab (equation 4.19) show a linear trend of increasing with k with a fit R^2 of 0.72 (Figure 4.8a). Four examples of water column profiles of TKE show a strong trend of TKE increasing with k throughout the water column (Figure 4.8b). The site shown

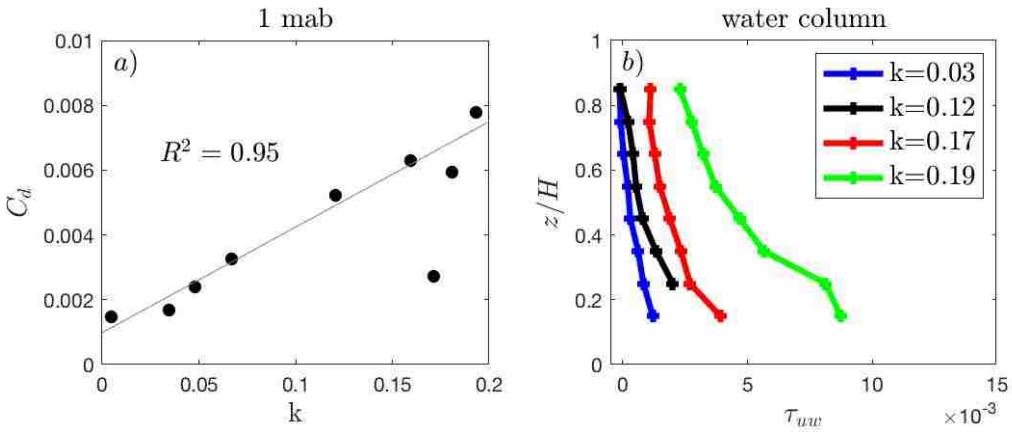

Figure 4.7: ADCP $\overline{u'w'}$ data: (a) C_d vs. k for each site where C_d has been calculated by combining all of the tides at each site and then using equation (4.8). The black line shows the robust fit. (b) Vertical profiles of τ_{uw} calculated with equation (4.5) at four sites with roughness ranging from $k = 0.03$ to $k = 0.19$.

with a k of 0.03 had many boat wakes in the data, which may have contributed to the higher TKE value near the surface. The overall trend of TKE increasing throughout the water column with k implies a surface measurement of TKE may be related to bed roughness.

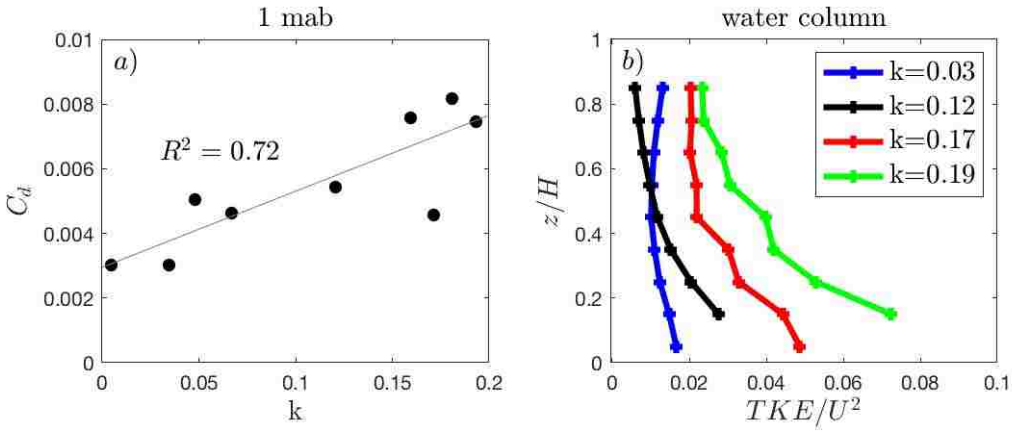

Figure 4.8: ADCP TKE data: (a) C_d vs. k for each site where C_d has been calculated by combining all of the tides at each site and then using equation (4.19). (b) Vertical profiles of normalized TKE at four sites with roughness ranging from $k = 0.03$ to $k = 0.19$.

Estimates of C_d based on surface TKE measurements (equation 4.19) rely on the rela-

tionship between the surface TKE and u_*^2 given in equation (4.18). This relationship is tested by comparing u_*^2 values computed with ADCP data 1 mab with u_*^2 values computed with surface data (Figure 4.9a). The ADCP measurements of u_*^2 show an increase and then a decrease near the end of the measurement period (Figure 4.9a). Estimates of u_*^2 from the surface TKE (equation 4.18) also show the same pattern. Spectra of the surface velocity data at the beginning of the tide did not fit a $f^{-5/3}$ profile with $R^2 > 0.9$ because the turbulence had not yet become fully developed but the u_*^2 estimates from the surface data still agreed well with those estimated from the ADCP data. The maximum u_*^2 values calculated from the surface data are higher than those calculated from the ADCP data. This may be due to waves causing higher TKE values. The presence of waves causes a peak in the velocity spectra, which lowers the R^2 value of an $f^{-5/3}$ fit. There are a few u_*^2 points that have R^2 values above 0.9 but still have u_*^2 values higher than those calculated with the ADCP data. This implies there may be conditions under which the surface TKE overestimates u_*^2 or that the *Nezu and Nakagawa* (1993b) coefficients found in the laboratory are not correct for the flow in this field data set.

Drag coefficient values estimated from surface TKE measurements (equation 4.19) show an increase with k (Figure 4.9b). They also show remarkable agreement with estimates of C_d from ADCP $\overline{u'w'}$ data for several tides. The average difference between the surface TKE estimates of C_d and the ADCP estimates of C_d is 0.0007 with a standard deviation of 0.0016.

4.3.4 C_d from $\overline{u'v'}$ Reynolds Stress

The horizontal Reynolds stress, $\overline{u'v'}$ is another turbulence statistic that may be useful for surface calculations of C_d. The Reynolds stress method of calculating C_d using $\overline{u'w'}$ cannot be used at the surface because w' is zero at the surface. *Shen et al.* (1999) showed that the turbulent energy from w' gets transferred to u' and v' near the surface, which implies $\overline{u'v'}$ may be useful as a proxy for $\overline{u'w'}$ if the relationship between $\overline{u'v'}$ and $\overline{u'w'}$ is known.

The relationship between $\overline{u'w'}$ and $\overline{u'v'}$ is explored in Figure 4.10 where vertical profiles are shown for two tides at different sites. There is a strong correspondence between $\overline{u'w'}$

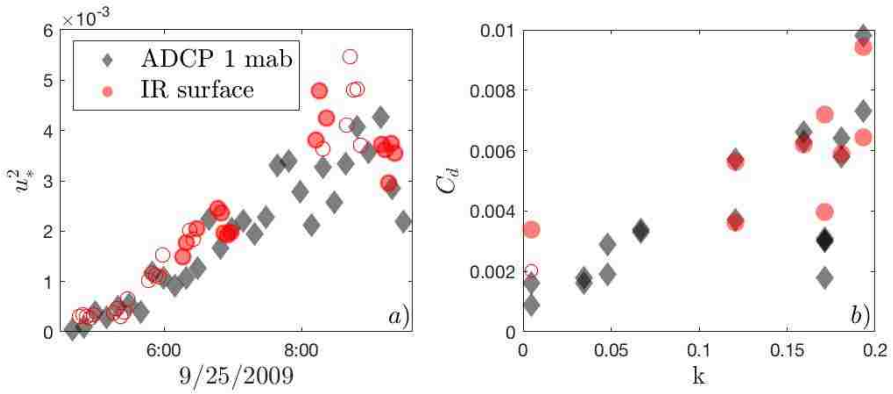

Figure 4.9: (a) Friction velocity calculated using ADCP data 1 mab (equation 4.6) and IR surface TKE data (equation 4.18) for a sample tide. Open circles indicate the R^2 of a fit of the IR velocity spectra to $f^{-5/3}$ was below 0.9 and filled circles indicate R^2 was greater than 0.9. b) C_d calculated as the slope of $u'w'$ vs. $u(u^2+v^2)^{1/2}$ for all 20 tides with the ADCP 1 mab and C_d calculated with IR TKE data using equation (4.19). The open circle indicates the R^2 of a fit of the IR velocity spectra to $f^{-5/3}$ was above 0.88 and the filled circles indicate $R^2 > 0.9$.

and $\overline{u'v'}$ at both sites with $\overline{u'v'}$ being smaller than $\overline{u'w'}$. At the site shown in Figure 4.10a, $\overline{u'v'}$ becomes negative halfway up the water column. The sign of $\overline{u'v'}$ is related to horizontal velocity gradients that are not related to bottom roughness, whereas the sign of $\overline{u'w'}$ is related to vertical velocity gradients that are related to bottom roughness. The equation derived for C_d based on $\overline{u'v'}$ (4.13) uses the absolute value of $\overline{u'v'}$. Figure 4.10 shows that while $\overline{u'w'}$ and $\overline{u'v'}$ are strongly related they are not equal and differences need to be accounted for in calculations of C_d. These profiles do not extend all the way up to the very near surface where *Shen et al.* (1999) predicted the energy from w' would be transferred to u' and v' so the exact relationship at the surface is not shown in this dataset.

An estimate of C_d from ADCP measurements of $\overline{u'v'}$ instead of $\overline{u'w'}$ (equation 4.12) is shown in Figure 4.11a for one example tide where the ratio between $\overline{u'w'}$ and $\overline{u'v'}$ has been derived using the *Nezu and Nakagawa* (1993b) profiles of u'_{rms}, v'_{rms}, and w'_{rms} (Section 4.1.2). The C_d calculated using equation (4.12) is 0.004, which is much smaller than the C_d of 0.0073 calculated using $\overline{u'w'}$ and shown in Figure 4.6a for the same tide. There are many low value $\overline{u'v'}$ points and a linear fit gives an R^2 of 0.04. When the $\overline{u'v'}$ calculation of C_d is

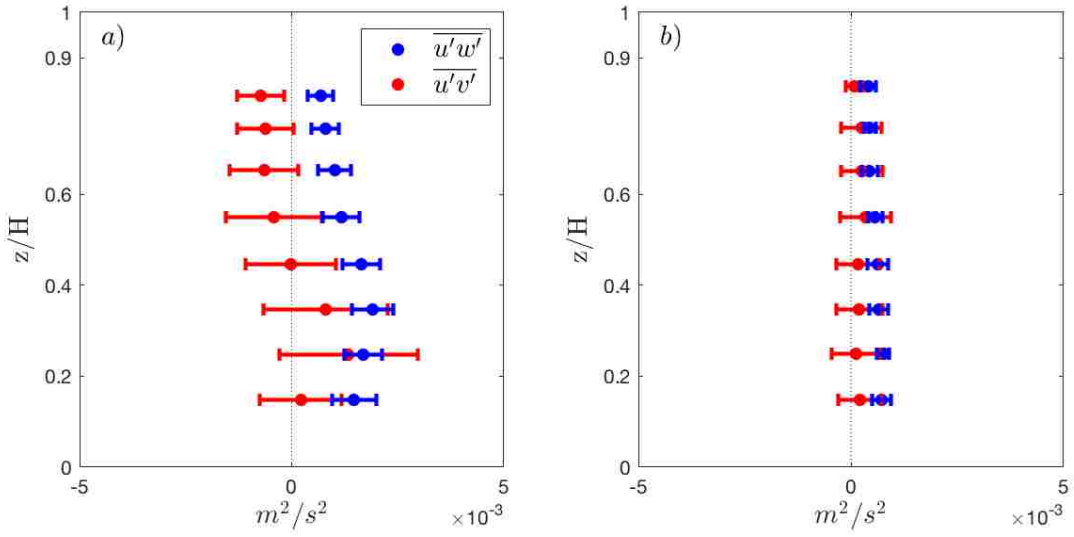

Figure 4.10: Vertical profiles of the Reynolds stress: (a) example tide where $\overline{u'v'}$ is negative near the surface (b) example tide where $\overline{u'v'}$ is positive near the surface.

repeated for the twenty tides, the values are lower than those calculated with $\overline{u'w'}$ but the site averages are correlated with k with an R^2 of 0.51 (Figure 4.11b). Figure 4.12a shows C_d values calculated after combining the $\overline{u'v'}$ data from multiple tides at each site and then computing C_d using equation 4.12. The C_d values computed with this method are very close to those calculated by computing the C_d for each tide and then taking the average as shown in Figure 4.11a. They are very similar because there is less tidal variability in the $\overline{u'v'}$ estimates of C_d than there was in the $\overline{u'w'}$ estimates. The combined tidal C_d values shown in Figure 4.12a are correlated with k ($R^2 = 0.50$) but not as strongly as those calculated using $\overline{u'w'}$ and shown in Figure 4.7a. This implies the relationship between bottom roughness and $\overline{u'v'}$ is not as strong as the relationship between bottom roughness and $\overline{u'w'}$.

Figure 4.12b explores how the normalized horizontal stress, τ_{uv}, changes with depth at four sites with different k values. The three sites with lower k values do not have τ_{uv} profiles that are as distinct with depth as the τ_{uw} profiles were in Figure 4.7b. The site with $k = 0.19$ has larger τ_{uv} values than any of the other sites but the profile in the water column does not show a smooth trend of decreasing from the bottom to the top. The site with $k = 0.17$

has larger τ_{uv} values than the site with $k = 0.12$ at every depth bin except for the top two. The site with $k = 0.03$ has a lower τ_{uv} value than the other sites for the bottom two depth bins but then increases vertically in the upper half of the water column. That site had many boat wakes that may have caused the higher $\overline{u'v'}$ values. These results suggest a C_d calculated with surface $\overline{u'v'}$ values may be only weakly related to bottom roughness.

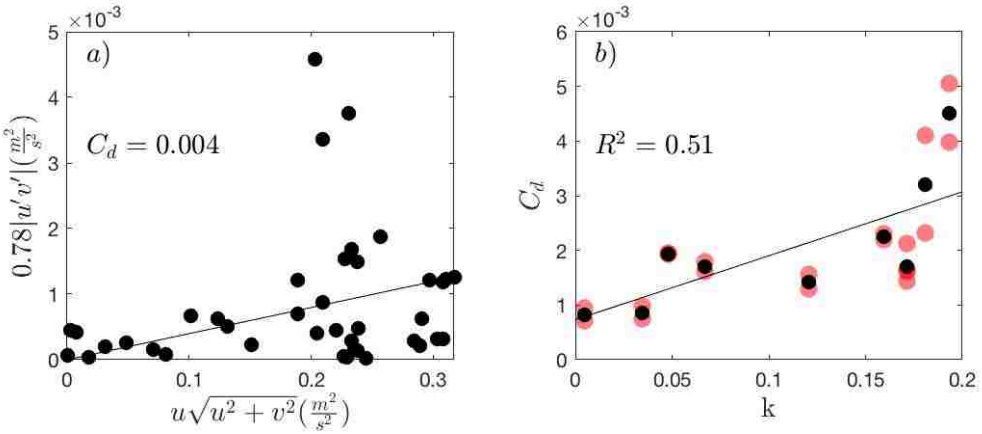

Figure 4.11: ADCP data one meter above the bed: calculation of C_d using $\overline{u'v'}$ in equation (4.12). (a) Example calculation of C_d for one tide at one site. C_d is the slope of $0.78|\overline{u'v'}|$ vs. $u(u^2 + v^2)^{1/2}$ (b) C_d calculated for twenty tides at the nine sites. Red circles are the measurements at each tide and black circles are the averages over all the tides at each site.

Drag coefficients calculated with surface $\overline{u'v'}$ measurements (equation 4.13) show an increase with k but have a large spread of values for sites with high k values (Figure 4.13). They agree well with values calculated with ADCP $\overline{u'w'}$ measurements 1 mab for some tides but not well for other tides. The average difference is 0.0028 and the standard deviation is 0.007. One tide has a particularly high C_d value of 0.024 that is far above the value of 0.007 value calculated with the ADCP data. That tide occurred at site E3, which was the closest site to the side of the river (Figure 4.1a). This indicates the $\overline{u'v'}$ measurement might be higher due to shear stress from the side of the river. When this is the case, $\overline{u'v'}$ is not a good proxy for $\overline{u'w'}$ and bottom roughness cannot be estimated from $\overline{u'v'}$ measurements.

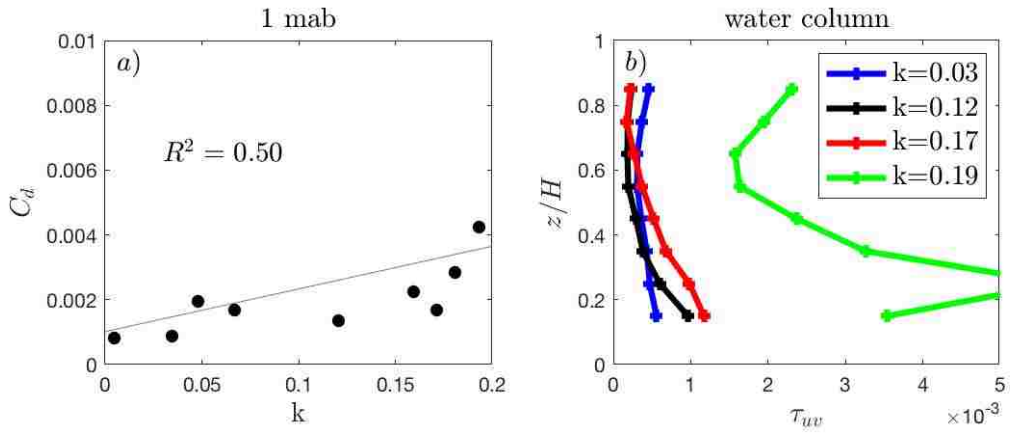

Figure 4.12: ADCP $\overline{u'v'}$ data: (a) C_d vs. k for each site where C_d has been calculated by combining all of the tides at each site and then using equation (4.12). (b) Vertical profiles of τ_{uv} calculated with equation (4.10) at four sites with roughness values ranging from $k = 0.03$ to $k = 0.19$.

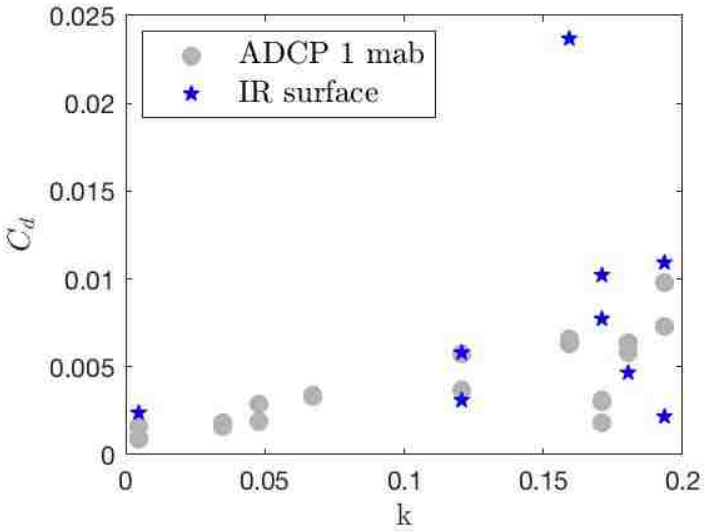

Figure 4.13: Comparison of C_d calculated with remotely sensed IR surface $\overline{u'v'}$ data (equation 4.13) and ADCP $\overline{u'w'}$ data measured 1 mab (equation 4.8).

4.3.5 Comparison of C_d calculation methods

Drag coefficients calculated with ADCP data 1 mab using $\overline{u'w'}$, $\overline{u'v'}$, and TKE all show a trend of increasing with k (Figure 4.14). The C_d values calculated with $\overline{u'v'}$ are smaller

than those calculated with $\overline{u'w'}$ because $\overline{u'v'}$ is not a good proxy for $\overline{u'w'}$ one meter above the bed. It can only be used as a proxy for $\overline{u'w'}$ if the energy from w' has been transferred to u' and v'. The energy from w' is only transferred to u' and v' very near the surface due to the surface boundary condition (*Shen et al.*, 1999). One meter above the bed the energy from the vertical direction has not been transferred to the horizontal directions so $\overline{u'v'}$ measures a purely horizontal shear stress instead of a vertical shear stress. The horizontal shear stress is not directly dependent on bottom roughness as the vertical shear stress is. Turbulent kinetic energy is related to bottom roughness because turbulence is generated by shear production and the shear depends on the bottom drag. The relationship is evident in equation 4.15 for TKE written in terms of u_*^2. Drag coefficients calculated with TKE 1 mab are higher than those calculated with $\overline{u'w'}$ 1 mab (Figure 4.14). The TKE calculation used here (equation 4.19) depends on the *Nezu and Nakagawa* (1993b) turbulent intensity profile equations that may not be accurate at the river bed.

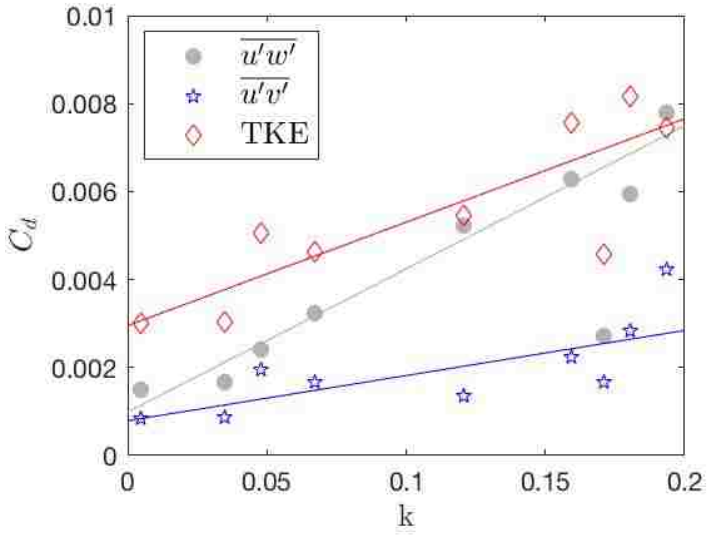

Figure 4.14: Comparison of C_d calculated with ADCP 1 mab $\overline{u'w'}$ data (equation 4.8), $\overline{u'v'}$ data (equation 4.12), and TKE data (equation 4.19).

Drag coefficients calculated with surface TKE and $\overline{u'v'}$ data also show trends of increasing with k and agree very well with values calculated with ADCP data measured 1 mab

for several tides (Figure 4.15a). The C_d values calculated with the TKE agree better with the C_d values calculated with the ADCP than those calculated with $\overline{u'v'}$. This highlights the fact that $\overline{u'v'}$ is a measure of horizontal shear stress and while it may be related to the vertical shear stress and therefore bottom roughness, it is also dependent on other factors such as the distance from the edge of the river. A comparison of the C_d values calculated with remotely sensed TKE versus those calculated with the *in situ* ADCP data shows remarkably good agreement for six of the nine tides measured (Figure 4.15b). Three tides show higher values calculated from the remotely sensed TKE data than those calculated with the *in situ* ADCP data. Two of those higher values were from tides where the ADCP fit had an $R^2 < 0.5$. The third value was from site F3 where the C_d value calculated with the ADCP data appears lower than expected for the k value calculated from the sonar data (Figure 4.6). The explanations for the three higher C_d values and the excellent agreement of the other six values implies the remote sensing method of using the surface TKE is a good method for calculating C_d.

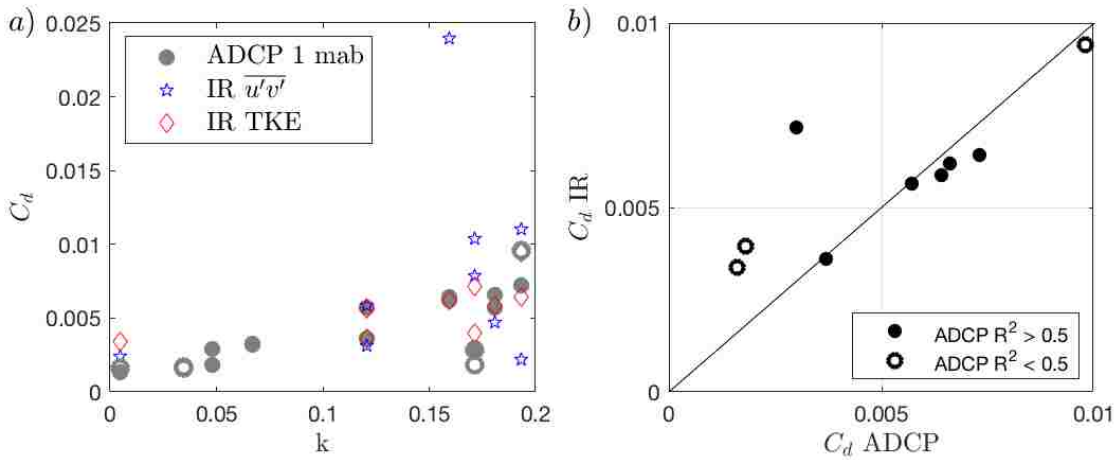

Figure 4.15: a)Comparison of C_d calculated with ADCP $\overline{u'w'}$ data (equation 4.8) and C_d calculated with remotely sensed surface $\overline{u'v'}$ and TKE data (equations 4.13 and 4.19) Solid circles are tides where the ADCP fit had an $R^2 > 0.5$ and open circles are where $R^2 < 0.5$. b) C_d calculated with remotely sensed TKE data from IR PIV measurements versus C_d calculated with ADCP $\overline{u'w'}$ measurements 1 mab. Solid circles are tides where the ADCP fit had an $R^2 > 0.5$ and open circles are where $R^2 < 0.5$. The one to one line is plotted for reference.

4.4 Discussion

This chapter has demonstrated two techniques for remote sensing of bottom roughness using IR imagery of the surface. The magnitudes of the drag coefficients calculated with the remotely sensed surface turbulent kinetic energy and Reynolds stress are in the range of values previously measured in other rivers and used in numerical models of river flow. The turbulent kinetic energy method gave C_d values from 0.0034 to 0.0094 and the Reynolds stress method gave C_d values from 0.0022 to 0.0240. *Fong et al.* (2009) measured C_d values from 0.0039 to 0.0166 in Three Mile Slough of the Sacramento-San Joaquin Delta and *Li et al.* (2004) measured C_d values from 0.0012 to 0.0069 in the James River Estuary. A typical value used in modeling studies is 0.003 (*Kukulka and Jay*, 2003; *Ralston et al.*, 2019). This value is slightly lower than 0.0034, which is the lowest C_d calculated with the surface TKE and slightly higher than 0.0022, which is the lowest C_d calculated with the surface $\overline{u'v'}$. The average C_d of the nine sites calculated with the 1 mab ADCP data was 0.0041. While 0.003 may be the best C_d value to use if no data are available, these results show there is probably significant variability in the actual values within the section of the river being modeled.

The remote sensing technique of measuring surface turbulence statistics and relating them to bottom roughness worked well for a specific set of conditions and assumptions. A cool skin layer needed to be present for the velocities to be detected in the imagery. This occurred mostly at night under clear skies. Rain, jumping fish, seals, passing logs, reflections, boat waves, and wind waves corrupted the IR imagery velocities used in the C_d calculation. The surface C_d equations were based on the assumption that the turbulence intensity profiles could be described by the *Nezu and Nakagawa* (1993b) equations (4.2, 4.3 and 4.4). That assumption is not valid when the salt wedge or strong secondary currents are present.

The salt wedge can reduce bottom generated turbulence that reaches the surface due to its lower near-bottom velocities and the impact of stratification on turbulence (*Beuzen et al.*, 2016). The equations presented here for calculating C_d from remote measurements of surface turbulence statistics are only applicable in the absence of the salt wedge. When the salt wedge is present the surface turbulence is cut off from the bottom roughness and

the near bed velocity may be in the upstream direction, while the surface velocity is in the downstream direction. The salt wedge cannot be directly observed in an IR image but the effects of the salt wedge on the turbulence can be observed. *Beuzen et al.* (2016) observed almost no boils at the surface when the salt wedge was present and a dramatic increase in the amount of boils as soon as the salt wedge retreated. The analysis of the remotely sensed data presented in this chapter was conducted without excluding data due to stratification. After the analysis was completed, it was found that the stratification was never above 0.5 PSU for the data where the turbulence spectra fit an $f^{-5/3}$ spectra with an R^2 above 0.9. Although this criteria is not a direct measure of the salt wedge absence, the strong relationship suggests it can work well to identify times when the salt wedge is absent.

The bottom roughness parameterization presented here uses a spectral method that does not take into account asymmetry in the bedforms. Asymmetry in the bedforms affects turbulence generation (*Cisneros et al.*, 2020), and can lead to changes in the drag coefficient observed between ebb and flood tides (*Fong et al.*, 2009). The sampling scheme used in my experiment did not allow me to examine one location on ebb and flood tides to test for asymmetry. I sampled ebb flood tides at locations that were close to each other but the water reaching those sites experienced different roughness characteristics as it approached the sites because the bathymety varied upstream and downstream of the sites (Figure 4.1). Future research is needed to develop and test a roughness parameterization that includes asymmetry and determines its effect on C_d.

4.5 Conclusions

Here I have used remotely measured surface turbulent kinetic energy and Reynolds stress statistics to estimate drag coefficients for six sites in the Snohomish River. Drag coefficient equations were derived from the *Nezu and Nakagawa* (1993b) turbulent intensity profile equations. The drag coefficients estimated from the remotely sensed data were compared to drag coefficients calculated from *in situ* ADCP data measured one meter above the river bed. Estimates of the drag coefficient from the remotely sensed turbulent kinetic energy statistics were closer to the *in situ* measured drag coefficients than those estimated from

measurements of the remotely sensed Reynolds stress. Both the drag coefficients estimated from the *in situ* data and those estimated from the remotely sensed data were correlated with a parameterization of the river bed roughness from transects of sonar scans.

The results presented here show remote sensing of bed roughness is possible from IR imagery of the surface. Future work could extend the applicability of these results by implementing these techniques with IR imagery from unmanned aerial vehicles.

Chapter 5

CONCLUSIONS

5.1 Summary

The goal of this thesis was to gain understanding of remotely sensed variables that can be used in the estimation of discharge at the river mouth with the added motivation of placing the findings in the context of the upcoming SWOT altimeter mission. Because the SWOT sensor has not yet been launched, Chapter 2 used airborne Lidar data to explore remotely sensed water surface elevation signals. The Lidar successfully measured the water surface elevation at the mouth of the Columbia River but time constraints of the data collection limited the range of discharge conditions observed. A wider range of discharge conditions was studied in Chapter 3 using a ROMS model of a generalized river. Chapter 4 explored the relationship between remotely sensed turbulence statistics and river bottom roughness, which is a key parameter in discharge estimation algorithms. Some of the remotely sensed variables studied in this thesis could be observed by SWOT, while others needed higher resolution instruments such as Lidar and infrared cameras.

The Lidar data examined in Chapter 2 proved useful for measuring surface gravity waves, water surface slope, and water surface elevation. The water surface elevation data compared well with in-situ data and could therefore be used to study the tidal cycle and amplitude. The water surface slope data compared well with ROMS output and showed strong tidal modulation. Time limitations of the field experiment meant that the water surface slope was not measured during similar tidal conditions but different river discharge conditions. This is the type of data that needs to be collected in order to fully understand the relationship between the water surface slope and discharge at the river mouth. Discharge can be estimated from remote measurements of velocity, which was found to be correlated with wave amplification. The correlation depended on the water level with respect to mean sea level but the Lidar had the ability to measure the water level at the same time as

the wave amplification. Chapter 2 showed high resolution instruments such as Lidar can measure wave amplification, water surface elevation, and water surface slope. These results indicate lower resolution instruments such as SWOT should be able to measure water surface elevation and slope changes with enough accuracy to determine the phase of the tide, but the exact relationship between the water surface elevation and discharge at the mouth of a tidally influenced river is left as an area of future research.

The ROMS modeling of a generalized river in Chapter 3 describes the shape of the water surface elevation at the river mouth from very low discharge to very high discharge. During low discharge, the water surface elevation changes are not large enough for a SWOT measurement to be used to estimate discharge near the river mouth. During high discharge, the water surface elevation one kilometer upstream of the mouth has a strong enough signal to estimate discharge from a SWOT measurement. No equation exists yet to estimate discharge from those measurements, but this is left as an area of future research. Offshore of the river mouth, a ridge developed during high discharge at the location where the freshwater separated from the seafloor. The location and height of the ridge varied with discharge and could provide an alternative method of estimating discharge. The height of the ridge was large enough to be detectable in a SWOT elevation measurement when the discharge was above a freshwater Froude number of two and the shelf slope was 0.005 or greater. The peak of the ridge had a slope change that was larger than the SWOT predicted slope accuracy and could be used to locate the peak and calculate the discharge using the location. Equations were derived relating the ridge peak and location to discharge. The equation predictions for ridge location agreed well with the ROMS output for all conditions. The equation predictions for ridge height agreed with the ROMS output below a freshwater Froude number of four. The ridge height and location were modulated but not eliminated by the tide. The formation of the offshore ridge during high discharge and the good agreement between its location and the location predicted by my equation point to a new method of estimating discharge from a remotely sensed variable.

Chapter 4 addressed the very important issue of bottom roughness. A new method of river botttom roughness parameterization was applied to nine locations on the Snohomish River. The parameterization derives a Nikuradse roughness length from spectral analysis

of bathymetry transects and values for the ten sites ranged from 0.005 to 0.19 m. The Nikuradse roughness lengths at each site were compared to drag coefficients calculated using near bottom *in situ* ADCP data and a previously published equation. New equations were derived to calculated the drag coefficient from remotely sensed measurements of the turbulent kinetic energy and the horizontal Reynolds stress. The drag coefficients calculated with the remotely sensed turbulent kinetic energy measurements compared well with the drag coefficients calculated with the *in situ* ADCP data. The success of the remote sensing method to measure bottom roughness confirmed turbulence theory that describes the vertical profile of turbulent kinetic energy from the bottom where it is generated by flow over roughness to the surface where it can be detected in imagery.

5.2 Suggestions for future work

The extensive field data sets used in this thesis offer many possibilities for future research. The DARLA data in Chapter 2 showed possible signals of the ridge that could not be verified without bottom salinity data. Prof. Akan's numerical model provides bottom salinity information that could be used to determine if the possible ridge signals were at the location of liftoff. The COHSTREX data in Chapter 4 was analyzed for a study of Reynolds stress and turbulent kinetic energy but it could also be used to study turbulent kinetic energy dissipation in the water column. Thermal imagery collected from a camera suspended by a helikite exists that could be analyzed to extract turbulence statistics at the various sites to strengthen the case that bottom roughness can be detected from an airborne platform.

The high resolution ROMS grid used in this thesis could be used to explore many more aspects of hydrodynamics at the river mouth. Tides could be added to low discharge runs to examine their effect on the water surface slope and the length of the salt wedge. To my knowledge, no theoretical expression exists that links tidal amplitudes and cycles to water surface slope changes at the mouth and just upstream. Tides may affect the water slope far upstream and also affect the length of the salt wedge. The length of the salt wedge is important from a remote sensing perspective because the water surface slope is negligible when a salt wedge is present and commonly used discharge algorithms do not apply. Winds

and alongshore currents could be added to study their effects on the height and location of the ridge.

A lower resolution grid of the Columbia River has been used for several years of ROMS runs (*MacCready et al.*, 2009). A brief examination of the model output showed possible signs of a ridge developing and propagating on ebb tide. Although the resolution is much lower than Prof. Akan's model described in Chapter 2, the long timeseries and wide range of tidal and discharge conditions would make it possible to study the effects of tides and discharge on the ridge.

I would recommend the following analysis steps to continue with this research:

- Compare possible Lidar ridge signals to Prof. Akan's modeled bottom salinities to determine if the ridge is at the liftoff location.

- Examine Prof. MacCready's model output of the Columbia River for the ridge at the liftoff location and relate it to the tidal cycle and river discharge.

- Add winds and alongshore currents to the high resolution ROMS implementation used in this thesis.

- Conduct PIV analysis of the helikite data at all of the sites to calculate the drag coefficient from an airborne platform.

5.3 Open questions

The three main contributions of this thesis are airborne measurements of water surface elevation at the river mouth showing tidal modulation of the slope and a relationship between wave amplification and discharge, the derivation of equations for the liftoff location and height of an offshore ridge that develops during high discharge, and the derivation of equations for the river bottom drag coefficient using remote measurements of turbulence statistics. These contributions led to several questions that I hope will be answered by future research. The questions are:

- How can the relationship between water surface slope at the river mouth and discharge be related mathematically in the presence of tides?
- Does a ridge actually form offshore during high discharge or are there other factors not considered in this thesis that might eliminate it?
- How can tidal modulation be added to my equations for liftoff location and ridge height?
- How do wind and currents affect the ridge?

BIBLIOGRAPHY

Akan, Ç., S. Moghimi, H. Özkan-Haller, J. Osborne, and A. Kurapov (2017), On the dynamics of the mouth of columbia river: Results from a three-dimensional fully coupled wave-current interaction model, *Journal of Geophysical Research: Oceans*.

Alsdorf, D. E., E. Rodríguez, and D. P. Lettenmaier (2007), Measuring surface water from space, *Reviews of Geophysics*, *45*(2).

Altenau, E. H., T. M. Pavelsky, D. Moller, L. H. Pitcher, P. D. Bates, M. T. Durand, and L. C. Smith (2019), Temporal variations in river water surface elevation and slope captured by airswot, *Remote Sensing of Environment*, *224*, 304–316.

Arcement, G. J., and V. R. Schneider (1989), Guide for selecting manning's roughness coefficients for natural channels and flood plains.

Armi, L., and D. Farmer (1986), Maximal two-layer exchange through a contraction with barotropic net flow, *Journal of Fluid Mechanics*, *164*, 27–51.

Auel, C., I. Albayrak, and R. M. Boes (2013), Turbulence characteristics in supercritical open channel flows: effects of froude number and aspect ratio, *Journal of Hydraulic Engineering*, *140*(4), 04014,004.

Balachandar, R., and F. Bhuiyan (2007), Higher-order moments of velocity fluctuations in an open-channel flow with large bottom roughness, *Journal of Hydraulic Engineering*, *133*(1), 77–87.

Baldassarre, G. D., and A. Montanari (2009), Uncertainty in river discharge observations: a quantitative analysis, *Hydrology and Earth System Sciences*, *13*(6), 913–921.

Barkan, R., J. C. McWilliams, A. F. Shchepetkin, M. J. Molemaker, L. Renault, A. Bracco, and J. Choi (2017), Submesoscale dynamics in the northern gulf of mexico. part i: Re-

gional and seasonal characterization and the role of river outflow, *Journal of Physical Oceanography*, *47*(9), 2325–2346.

Barnes, H. H. (1967), *Roughness characteristics of natural channels*, 1849, US Government Printing Office.

Bates, P. D., J. C. Neal, D. Alsdorf, and G. J.-P. Schumann (2013), Observing global surface water flood dynamics, in *The Earth's Hydrological Cycle*, pp. 839–852, Springer.

Best, J. (2005), The fluid dynamics of river dunes: A review and some future research directions, *Journal of Geophysical Research: Earth Surface*, *110*(F4).

Beuzen, T., C. C. Chickadel, and A. R. Horner-Devine (2016), Influence of subsurface stratification on turbulence and aeration in a tidal river, *IEEE Geoscience and Remote Sensing Letters*, *13*(12), 1975–1978.

Biancamaria, S., D. P. Lettenmaier, and T. M. Pavelsky (2016), The swot mission and its capabilities for land hydrology, *Surveys in Geophysics*, *37*(2), 307.

Bjerklie, D. M., S. L. Dingman, C. J. Vorosmarty, C. H. Bolster, and R. G. Congalton (2003), Evaluating the potential for measuring river discharge from space, *Journal of Hydrology*, *278*(1), 17–38.

Bonnema, M. G., S. Sikder, F. Hossain, M. Durand, C. J. Gleason, and D. M. Bjerklie (2016), Benchmarking wide swath altimetry-based river discharge estimation algorithms for the ganges river system, *Water Resources Research*, *52*(4), 2439–2461.

Campana, J., E. J. Terrill, and T. de Paolo (2016), The development of an inversion technique to extract vertical current profiles from x-band radar observations, *Journal of Atmospheric and Oceanic Technology*, *33*(9), 2015–2028, doi:10.1175/JTECH-D-15-0145.1.

Chatanantavet, P., M. P. Lamb, and J. A. Nittrouer (2012), Backwater controls of avulsion location on deltas, *Geophysical Research Letters*, *39*(1).

Chickadel, C. C., A. R. Horner-Devine, S. A. Talke, and A. T. Jessup (2009), Vertical boil propagation from a submerged estuarine sill, *Geophysical Research Letters*, *36*(10).

Chickadel, C. C., S. A. Talke, A. R. Horner-Devine, and A. T. Jessup (2011), Infrared-based measurements of velocity, turbulent kinetic energy, and dissipation at the water surface in a tidal river, *IEEE Geoscience and Remote Sensing Letters*, *8*(5), 849–853.

Cisneros, J., J. Best, T. Van Dijk, R. P. De Almeida, M. Amsler, J. Boldt, B. Freitas, C. Galeazzi, R. Huizinga, M. Iannirubertо, et al. (2020), Dunes in the world's big rivers are characterized by low-angle lee-side slopes and a complex shape, *Nature Geoscience*, pp. 1–7.

Cochrane, J., and F. Kelly (1986), Low-frequency circulation on the texas-louisiana continental shelf, *Journal of Geophysical Research: Oceans*, *91*(C9), 10,645–10,659.

Cole, K. L., and R. D. Hetland (2016), The effects of rotation and river discharge on net mixing in small-mouth kelvin number plumes, *Journal of Physical Oceanography*, *46*(5), 1421–1436.

Cowan, W. L. (1956), Estimating hydraulic roughness coefficients, *Agricultural Engineering*, *37*(7), 473–475.

Dean, R. G., and R. A. Dalrymple (1991), *Water wave mechanics for engineers and scientists*, vol. 2, world scientific publishing Co Inc.

DeVries, P. (2015), Reach Scale Geomorphic Analysis of Hydraulic, Hydrologic, and Sediment Conditions in the Snohomish River Between SR 522 and Ebey Slough, *Tech. rep.*, R2 Resource Consultants.

Durand, M., L.-L. Fu, D. P. Lettenmaier, D. E. Alsdorf, E. Rodriguez, and D. Esteban-Fernandez (2010), The surface water and ocean topography mission: Observing terrestrial surface water and oceanic submesoscale eddies, *Proceedings of the IEEE*, *98*(5), 766–779.

Durand, M., J. Neal, E. Rodríguez, K. M. Andreadis, L. C. Smith, and Y. Yoon (2014), Estimating reach-averaged discharge for the river severn from measurements of river water surface elevation and slope, *Journal of Hydrology*, *511*, 92–104.

Durand, M., C. Gleason, P.-A. Garambois, D. Bjerklie, L. Smith, H. Roux, E. Rodriguez, P. D. Bates, T. M. Pavelsky, J. Monnier, et al. (2016), An intercomparison of remote sensing river discharge estimation algorithms from measurements of river height, width, and slope, *Water Resources Research*, *52*(6), 4527–4549.

Elias, E. P., G. Gelfenbaum, and A. J. Van der Westhuysen (2012), Validation of a coupled wave-flow model in a high-energy setting: The mouth of the columbia river, *Journal of Geophysical Research: Oceans*, *117*(C9).

Fekete, B. M., C. J. Vörösmarty, and W. Grabs (1999), Global, composite runoff fields based on observed river discharge and simulated water balances.

Fong, D. A., and W. R. Geyer (2001), Response of a river plume during an upwelling favorable wind event, *Journal of Geophysical Research: Oceans*, *106*(C1), 1067–1084.

Fong, D. A., S. G. Monismith, M. T. Stacey, and J. R. Burau (2009), Turbulent stresses and secondary currents in a tidal-forced channel with significant curvature and asymmetric bed forms, *Journal of Hydraulic Engineering*, *135*(3), 198–208.

Garvine, R. W. (1982), A steady state model for buoyant surface plume hydrodynamics in coastal waters, *Tellus*, *34*(3), 293–306.

Garvine, R. W. (1984), Radial spreading of buoyant, surface plumes in coastal waters, *Journal of Geophysical Research: Oceans*, *89*(C2), 1989–1996.

Garvine, R. W. (1987), Estuary plumes and fronts in shelf waters: A layer model, *Journal of Physical Oceanography*, *17*(11), 1877–1896.

Geyer, W., and D. Ralston (2011), 2.03—the dynamics of strongly stratified estuaries, *Treatise on Estuarine and Coastal Science. Amsterdam: Elsevier*, pp. 37–52.

Geyer, W., P. Hill, and G. Kineke (2004), The transport, transformation and dispersal of sediment by buoyant coastal flows, *Continental Shelf Research*, *24*(7-8), 927–949.

Godin, G. (1999), The propagation of tides up rivers with special considerations on the upper saint lawrence river, *Estuarine, Coastal and Shelf Science*, *48*(3), 307–324.

González, F. (1984), A case study of wave–current–bathymetry interactions at the columbia river entrance, *Journal of physical oceanography*, *14*(6), 1065–1078.

Hameed, L. K., and S. T. Ali (2013), Estimating of manning's roughness coefficient for hilla river through calibration using hec-ras model, *Jordan Journal of Civil Engineering*, *159*(701), 1–10.

Hannah, D. M., S. Demuth, H. A. van Lanen, U. Looser, C. Prudhomme, G. Rees, K. Stahl, and L. M. Tallaksen (2011), Large-scale river flow archives: importance, current status and future needs, *Hydrological Processes*, *25*(7), 1191–1200.

Helaire, L. T., S. A. Talke, D. A. Jay, and D. Mahedy (2019), Historical changes in lower columbia river and estuary floods: a numerical study, *Journal of Geophysical Research: Oceans*.

Herbers, T. H. C., P. F. Jessen, T. T. Janssen, D. B. Colbert, and J. H. MacMahan (2012), Observing ocean surface waves with GPS tracked buoys, *J. Atmos. Ocean. Tech.*, *29*.

Hetland, R. D. (2005), Relating river plume structure to vertical mixing, *Journal of Physical Oceanography*, *35*(9), 1667–1688.

Hetland, R. D. (2010), The effects of mixing and spreading on density in near-field river plumes, *Dynamics of Atmospheres and Oceans*, *49*(1), 37–53.

Hetland, R. D., and D. G. MacDonald (2008), Spreading in the near-field merrimack river plume, *Ocean Modelling*, *21*(1-2), 12–21.

Hickey, B. M., and N. S. Banas (2003), Oceanography of the us pacific northwest coastal ocean and estuaries with application to coastal ecology, *Estuaries and Coasts*, *26*(4), 1010–1031.

Hickey, B. M., R. M. Kudela, J. Nash, K. W. Bruland, W. T. Peterson, P. MacCready, E. J. Lessard, D. A. Jay, N. S. Banas, A. M. Baptista, et al. (2010), River influences on shelf ecosystems: introduction and synthesis, *Journal of Geophysical Research: Oceans*, *115*(C2).

Horner-Devine, A. R., R. D. Hetland, and D. G. MacDonald (2015), Mixing and transport in coastal river plumes, *Annual Review of Fluid Mechanics*, *47*, 569–594.

Huber, P. J. (2004), *Robust statistics*, vol. 523, John Wiley & Sons.

Hudson, A. S., S. A. Talke, R. Branch, C. Chickadel, G. Farquharson, and A. Jessup (2017), Remote measurements of tides and river slope using an airborne lidar instrument, *Journal of Atmospheric and Oceanic Technology*, *34*(4), 897–904.

Jay, D. A., K. Leffler, and S. Degens (2010), Long-term evolution of columbia river tides, *Journal of waterway, port, coastal, and ocean engineering*, *137*(4), 182–191.

Jellesma, M. (2013), Form drag of subaqueous dune configurations, Master's thesis, University of Twente.

Jessup, A., C. Zappa, M. Loewen, and V. Hesany (1997), Infrared remote sensing of breaking waves, *Nature*, *385*(6611), 52.

Johnson, E. D., and E. A. Cowen (2017), Estimating bed shear stress from remotely measured surface turbulent dissipation fields in open channel flows, *Water Resources Research*, *53*(3), 1982–1996.

Johnson, N., C. Revenga, and J. Echeverria (2001), Managing water for people and nature, *Science*, *292*(5519), 1071–1072.

Jones, G. R., J. D. Nash, R. L. Doneker, and G. H. Jirka (2007), Buoyant surface discharges into water bodies. i: Flow classification and prediction methodology, *Journal of Hydraulic Engineering*, *133*(9), 1010–1020.

Jurisa, J. T., and R. J. Chant (2013), Impact of offshore winds on a buoyant river plume system, *Journal of Physical Oceanography*, *43*(12), 2571–2587.

Kärnä, T., and A. M. Baptista (2016), Evaluation of a long-term hindcast simulation for the columbia river estuary, *Ocean Modelling*, *99*, 1–14.

Kilcher, L. F., and J. D. Nash (2010), Structure and dynamics of the columbia river tidal plume front, *Journal of Geophysical Research: Oceans*, *115*(C5).

Kilcher, L. F., J. D. Nash, and J. N. Moum (2012), The role of turbulence stress divergence in decelerating a river plume, *Journal of Geophysical Research: Oceans*, *117*(C5).

Kukulka, T., and D. A. Jay (2003), Impacts of columbia river discharge on salmonid habitat: 1. a nonstationary fluvial tide model, *Journal of Geophysical Research: Oceans*, *108*(C9).

Kundu, P. K., D. R. Dowling, G. Tryggvason, and I. M. Cohen (2015), Fluid mechanics.

Lamb, M. P., J. A. Nittrouer, D. Mohrig, and J. Shaw (2012), Backwater and river plume controls on scour upstream of river mouths: Implications for fluvio-deltaic morphodynamics, *Journal of Geophysical Research: Earth Surface*, *117*(F1).

Lane, E. W. (1957), A study of the shape of channels formed by natural streams flowing in erodible material, *MRD sediment series; no. 9*.

LeFavour, G., and D. Alsdorf (2005), Water slope and discharge in the amazon river estimated using the shuttle radar topography mission digital elevation model, *Geophysical Research Letters*, *32*(17).

Lettenmaier, D. P., D. Alsdorf, J. Dozier, G. J. Huffman, M. Pan, and E. F. Wood (2015), Inroads of remote sensing into hydrologic science during the wrr era, *Water Resources Research*, *51*(9), 7309–7342.

Li, C., A. Valle-Levinson, L. P. Atkinson, K. C. Wong, and K. M. Lwiza (2004), Estimation of drag coefficient in james river estuary using tidal velocity data from a vessel-towed adcp, *Journal of Geophysical Research: Oceans*, *109*(C3).

Liu, Y., P. MacCready, B. M. Hickey, E. P. Dever, P. M. Kosro, and N. S. Banas (2009), Evaluation of a coastal ocean circulation model for the columbia river plume in summer 2004, *Journal of Geophysical Research: Oceans*, *114*(C2).

MacCready, P., N. S. Banas, B. M. Hickey, E. P. Dever, and Y. Liu (2009), A model study of tide-and wind-induced mixing in the columbia river estuary and plume, *Continental Shelf Research*, *29*(1), 278–291.

MacDonald, D. G., and W. R. Geyer (2004), Turbulent energy production and entrainment at a highly stratified estuarine front, *Journal of Geophysical Research: Oceans*, *109*(C5).

MacDonald, D. G., and W. R. Geyer (2005), Hydraulic control of a highly stratified estuarine front, *Journal of physical oceanography*, *35*(3), 374–387.

Manning, R., J. P. Griffith, T. Pigot, and L. F. Vernon-Harcourt (1890), *On the flow of water in open channels and pipes*.

McCabe, R. M., P. MacCready, and B. M. Hickey (2009), Ebb-tide dynamics and spreading of a large river plume, *Journal of Physical Oceanography*, *39*(11), 2839–2856.

Moftakhari, H., D. Jay, and S. Talke (2016), Estimating river discharge using multiple-tide gauges distributed along a channel, *Journal of Geophysical Research: Oceans*, *121*(4), 2078–2097.

Moog, D. B., and G. H. Jirka (1999a), Stream reaeration in nonuniform flow: Macroroughness enhancement, *Journal of Hydraulic Engineering*, *125*(1), 11–16.

Moog, D. B., and G. H. Jirka (1999b), Air-water gas transfer in uniform channel flow, *Journal of hydraulic engineering*, *125*(1), 3–10.

Naik, P. K., and D. A. Jay (2011), Distinguishing human and climate influences on the columbia river: changes in mean flow and sediment transport, *Journal of hydrology*, *404*(3), 259–277.

Nezu, I. (1977), Turbulent structure in open-channel flows, Ph.D. thesis, Kyoto University.

Nezu, I., and H. Nakagawa (1993a), *Turbulence in open channel flows*, CRC Press.

Nezu, I., and H. Nakagawa (1993b), Turbulence in open-channel flows, iahr monograph series, *AA Balkema, Rotterdam*, pp. 1–281.

Nickles, C., E. Beighley, Y. Zhao, M. Durand, C. David, and H. Lee (2019), How does the unique space-time sampling of the swot mission influence river discharge series characteristics?, *Geophysical Research Letters*, *46*(14), 8154–8161.

Nikora, V. I., D. G. Goring, and B. J. Biggs (1998), On gravel-bed roughness characterization, *Water Resources Research*, *34*(3), 517–527.

NOAA (2015), Estimation of vertical uncertainties in vdatum.

O'Donnell, J. (1990), The formation and fate of a river plume: A numerical model, *Journal of Physical Oceanography*, *20*(4), 551–569.

O'Loughlin, F. E., J. Neal, D. Yamazaki, and P. D. Bates (2016), Icesat-derived inland water surface spot heights, *Water Resources Research*, *52*(4), 3276–3284.

Orem, H. M. (1968), *Discharge in the lower Columbia River basin, 1928-65*, vol. 550, US Geological Survey.

Parhi, P. K., R. Sankhua, and G. Roy (2012), Calibration of channel roughness for mahanadi river,(india) using hec-ras model, *Journal of Water Resource and Protection*, *4*(10), 847.

Pavelsky, T. M., M. T. Durand, K. M. Andreadis, R. E. Beighley, R. C. Paiva, G. H. Allen, and Z. F. Miller (2014), Assessing the potential global extent of swot river discharge observations, *Journal of Hydrology*, *519*, 1516–1525.

Pawlowicz, R., B. Beardsley, and S. Lentz (2002), Classical tidal harmonic analysis including error estimates in matlab using t_tide, *Computers & Geosciences*, *28*(8), 929–937.

Poggioli, A. R., and A. R. Horner-Devine (2015), The sensitivity of salt wedge estuaries to channel geometry, *Journal of Physical Oceanography*, *45*(12), 3169–3183.

Poggioli, A. R., and A. R. Horner-Devine (2018), Two-layer hydraulics at the river–ocean interface, *Journal of Fluid Mechanics*, *856*, 633–672.

Pritchard, M., and D. A. Huntley (2006), A simplified energy and mixing budget for a small river plume discharge, *Journal of Geophysical Research: Oceans*, *111*(C3).

Qu, L., and R. D. Hetland (2019), Temporal resolution of wind forcing required for river plume simulations, *Journal of Geophysical Research: Oceans*, *124*(3).

Ralston, D. K., W. R. Geyer, and J. A. Lerczak (2010), Structure, variability, and salt flux in a strongly forced salt wedge estuary, *Journal of Geophysical Research: Oceans*, *115*(C6).

Ralston, D. K., G. W. Cowles, W. R. Geyer, and R. C. Holleman (2017), Turbulent and numerical mixing in a salt wedge estuary: Dependence on grid resolution, bottom roughness, and turbulence closure, *Journal of Geophysical Research: Oceans*, *122*(1), 692–712.

Ralston, D. K., S. Talke, W. R. Geyer, H. A. Al-Zubaidi, and C. K. Sommerfield (2019), Bigger tides, less flooding: Effects of dredging on barotropic dynamics in a highly modified estuary, *Journal of Geophysical Research: Oceans*, *124*(1), 196–211.

Reineman, B. D., L. Lenain, D. Castel, and W. K. Melville (2009), A portable airborne scanning lidar system for ocean and coastal applications, *Journal of Atmospheric and oceanic technology*, *26*(12), 2626–2641.

Rodriguez, E. (2016), Surface water and ocean topography mission (swot): Science requirements document, *SWOT NASA/JPL Project, Pasadena, Calif.[Available at https://swot. jpl. nasa. gov/files/swot/SRD_021215. pdf.]*.

Safaie, B. (1979), Mixing of buoyant surface jet over sloping bottom, *Journal of the Waterway, Port, Coastal and Ocean Division*, *105*(4), 357–373.

Sanford, T. B., and R.-C. Lien (1999), Turbulent properties in a homogeneous tidal bottom boundary layer, *Journal of Geophysical Research: Oceans*, *104*(C1), 1245–1257.

Saunders, P. M. (1967), The temperature at the ocean-air interface, *Journal of the Atmospheric Sciences*, *24*(3), 269–273.

Shchepetkin, A. F., and J. C. McWilliams (2005), The regional oceanic modeling system (roms): a split-explicit, free-surface, topography-following-coordinate oceanic model, *Ocean modelling*, *9*(4), 347–404.

Shchepetkin, A. F., and J. C. McWilliams (2009), Correction and commentary for "ocean forecasting in terrain-following coordinates: Formulation and skill assessment of the re-

gional ocean modeling system" by haidvogel et al., j. comp. phys. 227, pp. 3595–3624, *Journal of Computational Physics*, *228*(24), 8985–9000.

Shen, L., X. Zhang, D. K. Yue, and G. S. Triantafyllou (1999), The surface layer for free-surface turbulent flows, *Journal of Fluid Mechanics*, *386*, 167–212.

Stacey, M. T., S. G. Monismith, and J. R. Burau (1999), Measurements of reynolds stress profiles in unstratified tidal flow, *Journal of Geophysical Research: Oceans*, *104*(C5), 10,933–10,949.

Sturm, T. W. (2010), *Open channel hydraulics*, McGraw-Hill New York.

Suanda, S. H., F. Feddersen, and N. Kumar (2017), The effect of barotropic and baroclinic tides on coastal stratification and mixing, *Journal of Geophysical Research: Oceans*, *122*(12), 10–156.

Syvitski, J. P., and Y. Saito (2007), Morphodynamics of deltas under the influence of humans, *Global and Planetary Change*, *57*(3-4), 261–282.

Syvitski, J. P., S. D. Peckham, R. Hilberman, and T. Mulder (2003), Predicting the terrestrial flux of sediment to the global ocean: a planetary perspective, *Sedimentary Geology*, *162*(1), 5–24.

Talke, S. A., A. R. Horner-Devine, C. C. Chickadel, and A. T. Jessup (2013), Turbulent kinetic energy and coherent structures in a tidal river, *Journal of Geophysical Research: Oceans*, *118*(12), 6965–6981.

Thomson, J. (2012), Wave breaking dissipation observed with "swift" drifters, *Journal of Atmospheric and Oceanic Technology*, *29*(12), 1866–1882.

Thomson, J., A. R. Horner-Devine, S. Zippel, C. Rusch, and W. Geyer (2014), Wave breaking turbulence at the offshore front of the columbia river plume, *Geophysical Research Letters*, *41*(24), 8987–8993.

Timbadiya, P. V., P. L. Patel, and P. D. Porey (2011), Calibration of hec-ras model on prediction of flood for lower tapi river, india, *Journal of Water Resource and Protection*, *3*(11), 805.

Tuozzolo, S., G. Lind, B. Overstreet, J. Mangano, M. Fonstad, M. Hagemann, R. Frasson, K. Larnier, P.-A. Garambois, J. Monnier, et al. (2019), Estimating river discharge with swath altimetry: A proof of concept using airswot observations, *Geophysical Research Letters*.

Turki, I., B. Laignel, L. Chevalier, S. Costa, and N. Massei (2015), On the investigation of the sea-level variability in coastal zones using swot satellite mission: Example of the eastern english channel (western france), *IEEE Journal of Selected Topics in Applied Earth Observations and Remote Sensing*, *8*(4), 1564–1569.

Wang, B., S. Giddings, O. Fringer, E. Gross, D. Fong, and S. Monismith (2011), Modeling and understanding turbulent mixing in a macrotidal salt wedge estuary, *Journal of Geophysical Research: Oceans*, *116*(C2).

Warner, J. C., B. Armstrong, R. He, and J. B. Zambon (2010), Development of a coupled ocean-atmosphere-wave-sediment transport (coawst) modeling system, *Ocean Modelling*, *35*(3), 230–244.

Xu, P., X. Mao, and W. Jiang (2017), Estimation of the bottom stress and bottom drag coefficient in a highly asymmetric tidal bay using three independent methods, *Continental Shelf Research*, *140*, 37–46.

Yang, K., R. Nie, X. Liu, and S. Cao (2013), Modeling depth-averaged velocity and boundary shear stress in rectangular compound channels with secondary flows, *Journal of Hydraulic Engineering*, *139*(1), 76–83.

Yankovsky, A. E., and D. C. Chapman (1997), A simple theory for the fate of buoyant coastal discharges, *Journal of Physical oceanography*, *27*(7), 1386–1401.

Yuan, Y., and A. R. Horner-Devine (2013), Laboratory investigation of the impact of lateral

spreading on buoyancy flux in a river plume, *Journal of Physical Oceanography*, *43*(12), 2588–2610.

Zhang, X., R. D. Hetland, M. Marta-Almeida, and S. F. DiMarco (2012), A numerical investigation of the mississippi and atchafalaya freshwater transport, filling and flushing times on the texas-louisiana shelf, *Journal of Geophysical Research: Oceans*, *117*(C11).

Zhang, Z., and R. Hetland (2012), A numerical study on convergence of alongshore flows over the texas-louisiana shelf, *Journal of Geophysical Research: Oceans*, *117*(C11).

Zippel, S., and J. Thomson (2017), Surface wave breaking over sheared currents: Observations from the mouth of the columbia river, *Journal of Geophysical Research: Oceans*, pp. n/a–n/a.

Appendix A

DERIVATIONS

A.0.1 Ridge height derivation

$$u\frac{\partial u}{\partial h_*} = -g\frac{\partial \eta}{\partial h_*} - \frac{C_D u^2}{h\delta} \tag{A.1}$$

The dimensionless plume thickness is defined as $h_* = 1 + \alpha x/h_s$, C_D is the drag coefficient, and $\delta = \alpha/h_s$. Substitute in Q/A for u

$$\frac{Q}{A}\frac{\partial}{\partial h_*}\frac{Q}{A} = -g\frac{\partial \eta}{\partial h_*} - \frac{C_D}{h\delta}\frac{Q^2}{A^2} \tag{A.2}$$

Differentiate Q/A with respect to h_*

$$\frac{-Q^2}{A^3}\frac{\partial A}{\partial h_*} = -g\frac{\partial \eta}{\partial h_*} - \frac{C_D}{h\delta}\frac{Q^2}{A^2} \tag{A.3}$$

Solve for $\frac{\partial \eta}{\partial h_*}$

$$\frac{\partial \eta}{\partial h_*} = \frac{Q^2}{A^3 g}\frac{\partial A}{\partial h_*} - \frac{C_D}{h\delta g}\frac{Q^2}{A^2} \tag{A.4}$$

An equation for A can be written using (3.11), (3.12), and the fact that $h = h_s h_*$

$$A = h_s h_* b_0 exp(\frac{\Gamma}{Fr_f}(h_*^{5/2} - 1) \tag{A.5}$$

Differentiate with (A.5) respect to h_* to obtain

$$\frac{\partial A}{\partial h_*} = b_0 h_s exp[\frac{\Gamma}{Fr_f}(h_*^{5/2} - 1)][\frac{5\Gamma}{2Fr_f}h_*^{5/2} + 1] \tag{A.6}$$

Substitute (A.5) and (A.6) into (A.4)

$$\frac{\partial \eta}{\partial h_*} = \frac{Q^2 b_0 h_s exp[\frac{\Gamma}{Fr_f}(h_*^{5/2} - 1)][\frac{5\Gamma}{2Fr_f}h_*^{5/2} + 1]}{g b_0^3 h_s^3 h_*^3 exp[\frac{\Gamma}{Fr_f}(h_*^{5/2} - 1)]^3} - \frac{C_D Q^2}{h_*^3 \delta g b_0^2 h_s^3}[\frac{1}{[exp[\frac{\Gamma}{Fr_f}(h_*^{5/2} - 1)]^2}] \tag{A.7}$$

Simplify to

$$\frac{\partial \eta}{\partial h_*} = \frac{Q^2}{g b_0^2 h_s^2}\left[\frac{\frac{5}{2}\frac{\Gamma}{Fr_f}h_*^{-0.5} + h_*^{-3}}{(exp[\frac{\Gamma}{Fr_f}(h_*^{5/2} - 1)]^2}\right] - \frac{Q^2 C_D}{h_*^3 \delta g b_0^2 h_s^3}\left[\frac{1}{[exp[\frac{\Gamma}{Fr_f}(h_*^{5/2} - 1)]]^2}\right] \tag{A.8}$$

Integrate to obtain h_{ridge}

$$h_{ridge} = \frac{Q^2}{gb_0^2h_s^2}\int_1^{1+\frac{\alpha L_{lo}}{h_s}} \frac{\frac{\Gamma}{Fr_f}2.5h_*^{-0.5}+h_*^{-3}}{[exp[\frac{\Gamma}{Fr_f}(h_*^{5/2}-1)]]^2}\partial h_* - \frac{Q^2C_D}{\delta gb_0^2h_s^3}\int_1^{1+\frac{\alpha L_{lo}}{h_s}} \frac{1}{h_*^3[exp[\frac{\Gamma}{Fr_f}(h_*^{5/2}-1)]]^2}\partial h_* \tag{A.9}$$

Rewrite in terms of Fr_f instead of Q and combine terms.

$$h_{ridge} = \frac{g'Fr_f^2h_s}{g}\left\{\int_1^{1+\frac{\alpha L_{lo}}{h_s}} \frac{\frac{\Gamma}{Fr_f}2.5h_*^{-0.5}+h_*^{-3}}{exp[\frac{2\Gamma}{Fr_f}(h_*^{5/2}-1)]}\partial h_* - \frac{C_D}{\alpha}\int_1^{1+\frac{\alpha L_{lo}}{h_s}} \frac{1}{h_*^3exp[\frac{2\Gamma}{Fr_f}(h_*^{5/2}-1)]}\partial h_*\right\} \tag{A.10}$$

$$h_{ridge} = \frac{g'Fr_f^2h_s}{g}\left\{\int_1^{1+\frac{\alpha L_{lo}}{h_s}} \frac{\frac{\Gamma}{Fr_f}2.5h_*^{5/2}+1-\frac{C_D}{\alpha}}{h_*^3exp[\frac{2\Gamma}{Fr_f}(h_*^{5/2}-1)]}\partial h_*\right\} \tag{A.11}$$

A.0.2 Ridge height derivation with negligible spreading

When spreading is negligible κ can be set to 0 and equation (3.18) becomes

$$h_{ridge} = \frac{g'Fr_f^2h_s}{g}\left\{\int_1^{1+\frac{\alpha L_{lo}}{h_s}} \frac{1-\frac{C_D}{\alpha}}{h_*^3}\partial h_*\right\} \tag{A.12}$$

The depth at liftoff, h_{lo}, can be substituted in for the upper integration limit.

$$h_{lo} = 1 + \frac{\alpha L_{l0}}{h_s} \tag{A.13}$$

$$h_{ridge} = \frac{g'Fr_f^2h_s}{g}\left\{\int_1^{h_{lo}} \frac{1}{h_*^3}\partial h_* - \frac{C_D}{\alpha}\int_1^{h_{lo}} \frac{1}{h_*^3}\partial h_*\right\} \tag{A.14}$$

$$h_{ridge} = \frac{-g'h_s}{2g}Fr_f^2\left[(h_{lo}^{-2}-1) - (\frac{C_D}{\alpha}(h_{lo}^{-2}-1)\right] \tag{A.15}$$

Equation (3.14) can be used to write h_{lo} in terms of Fr_f

$$h_{ridge} = \frac{-g'h_s}{2g}Fr_f^2\left[(Fr_f^{-4/3}-1) - (\frac{C_D}{\alpha}(Fr_f^{-4/3}-1)\right] \tag{A.16}$$

which simplifies to

$$h_{ridge} = \frac{1}{2}\frac{g'}{g}h_s\left[\left(1-\frac{C_D}{\alpha}\right)\left(Fr_f^2 - Fr_f^{2/3}\right)\right]. \tag{A.17}$$